



**MODAL PARAMETERS AND FAULT
TRANSIENTS IN DOUBLE-CIRCUIT
TRANSMISSION LINES: ON THE EFFECTS
OF CONDUCTOR TRANSPOSITION, SHIELD
WIRES, AND LOSSY SOIL MODELING**

CAIO MISSIAGGIA MORAES

**DISSERTAÇÃO DE MESTRADO
EM ENGENHARIA ELÉTRICA**

DEPARTAMENTO DE ENGENHARIA ELÉTRICA

**FACULDADE DE TECNOLOGIA
UNIVERSIDADE DE BRASÍLIA**

FICHA CATALOGRÁFICA

MORAES, CAIO MISSIAGGIA

Modal Parameters and Fault Transients in Double-Circuit Transmission Lines: On the Effects Of Conductor Transposition, Shield Wires, and Lossy Soil Modeling. [Brasília/DF] 2022.

xxx, 112p., 210 x 297 mm (ENE/FT/UnB, Mestre, Dissertação de Mestrado, 2022).

Universidade de Brasília, Faculdade de Tecnologia, Departamento de Engenharia Elétrica.

Departamento de Engenharia Elétrica

- | | |
|-------------------------------|-------------------------------|
| 1. ATP/EMTP | 2. Transmission line modeling |
| 3. Electromagnetic transients | 4. Modal parameters |
| 5. Sequence parameters | 6. Frequency-dependent soil |
| 7. Conductor transposition | 8. Shield wires modeling |
| I. ENE/FT/UnB | II. Título (série) |

REFERÊNCIA BIBLIOGRÁFICA

MORAES, CAIO MISSIAGGIA (2022). Modal Parameters and Fault Transients in Double-Circuit Transmission Lines: On the Effects Of Conductor Transposition, Shield Wires, and Lossy Soil Modeling. Dissertação de Mestrado, Publicação PPGEE.XXXXX/2022, Departamento de Engenharia Elétrica, Universidade de Brasília, Brasília, DF, 112p.

CESSÃO DE DIREITOS

AUTOR: Caio Missiaggia Moraes

TÍTULO: Modal Parameters and Fault Transients in Double-Circuit Transmission Lines: On the Effects Of Conductor Transposition, Shield Wires, and Lossy Soil Modeling.

GRAU: Mestre ANO: 2022

É concedida à Universidade de Brasília permissão para reproduzir cópias desta Dissertação de Mestrado e para emprestar ou vender tais cópias somente para propósitos acadêmicos e científicos. O autor reserva outros direitos de publicação e nenhuma parte desta dissertação de mestrado pode ser reproduzida sem autorização por escrito do autor.

Caio Missiaggia Moraes

Universidade de Brasília (UnB)

Campus Darcy Ribeiro

Faculdade de Tecnologia - FT

Departamento de Engenharia Elétrica(ENE)

Brasília - DF CEP 70919-970

*A bend in the road is not the end of the road...
Unless you fail to make the turn.*

— Helen Keller

ACKNOWLEDGEMENTS

I wish to express my gratitude...

...first to God for having illuminated my path during my master's degree and for giving me spiritual strength along this journey.

...to my family, especially my mother Alessandra and my sister Bia, for providing me with all the opportunities I have had so far, always with the support and the emotional strength necessary in the most delicate moments.

...to professor Amauri, engineer and person for whom I have great admiration, respect, and above all, friendship. I appreciate your patience, knowledge, and disposition for support in the most challenging moments.

...to the members of the research team, Professor Felipe, Professor Kleber, Professor Raphael, and Eduardo, with whom I had the opportunity to deeply learn practical aspects about transmission system and protection of transmission lines. Your knowledge and experience in the field of transmission systems and line protection have been invaluable in shaping my understanding and skills.

...to all my friends who have been with me throughout my journey in the master's program, serving as a source of distraction and bringing joy during this challenging path. Your presence has been a constant source of encouragement and positivity.

...to the entire IATI, Evoltz, and Cepel teams who provided technical and financial support for the development of this research.

Thank you very much to everyone involved! I will always be very grateful to everyone.

ABSTRACT

This work analyzes the impact of conductor transposition, shield wires, and soil modeling on modal parameters of a double-circuit transmission line. Computational modeling routines are developed to represent transmission line parameters span by span, capturing parameter variation along the right-of-way. The circuit model is constructed using EMTP-type software, considering impedances and admittances calculated to account for conductive and displacement current effects on lossy earth. Transient studies are performed on a real 500 kV double-circuit transmission line, considering various scenarios of soil resistivity, transposition and shield wire modeling. Faults are applied at every 1% of the power line, which represents 100 faults per scenario. Results show that a uniform soil model calculated from the average of deep-layer soil model resistivities along the right-of-way accurately represents heterogeneous resistivity distribution along the line, with less than 1% discrepancy. Transposition schemes rotating phases in opposite directions result in lower short-circuit currents, improving safety. The use of Kron reduction, as traditionally performed in line parameters calculations, yields conservative results compared to the realistic model, overestimating fault branch currents and short-circuit contribution currents by 1.1 p.u. (600 A).

Keywords: ATP/EMTP, conductor transposition, transmission line modeling, electromagnetic transients, frequency-dependent soil, modal parameters, sequence parameters, shield wire modeling.

RESUMO

TÍTULO TRADUZIDO: Efeitos da Transposição de Condutores, Cabos Para-Raio e Modelagem do Solo nos Parâmetros Modais e nos Transitórios Eletromagnéticos de uma Linha de Transmissão de Circuito Duplo.

Este trabalho analisa o impacto da transposição de condutores, cabos para-raio e modelagem do solo nos parâmetros modais de uma linha de transmissão em circuito duplo. Foram desenvolvidas rotinas de modelagem computacional para representar os parâmetros modais da linha de transmissão, considerando a variação dos parâmetros ao longo da faixa de servidão. O modelo circuital é construído usando *software* do tipo EMTP, sendo consideradas as impedâncias e admitâncias calculadas para levar em conta os efeitos de corrente condutiva e de dispersão em solos variantes na frequência. Foram realizados estudos transitórios em uma linha de transmissão real de 500 kV em circuito duplo, considerando diversos cenários de resistividade do solo, transposição e modelagem do cabos para-raio. As faltas foram aplicadas a cada 1% da linha de transmissão, o que representa 100 faltas por cenário. Os resultados mostram que um único valor de resistividade sendo a média das resistividades da camada profunda representa com precisão a distribuição heterogênea de resistividade ao longo da linha, com uma discrepância inferior a 1%. Os esquemas de transposição que giram as fases dos circuitos em direções opostas resultam em correntes de curto-circuito mais baixas, melhorando a segurança do sistema de transmissão. O uso da redução de Kron, como é tradicionalmente realizada nos cálculos dos parâmetros da linha, produz resultados conservadores em comparação com o modelo modal-descomposto realista, com a superestimação das correntes do ramo de falta e das correntes de contribuição de curto-circuito em 1,1 p.u. (600 A).

Palavras-chave: ATP/EMTP, transposição de condutores, modelagem de linhas de transmissão, transitórios eletromagnéticos, solos variantes na frequência, parâmetros modais, componentes simétricos, modelagem de cabos para-raio.

TABLE OF CONTENTS

Table of contents	i
List of figures	iv
List of tables	xi
List of symbols	xiii
Glossary	xvi
Chapter 1 – Introduction	1
1.1 Preface	1
1.2 Review of the Specialized Literature	2
1.3 Objectives and Scope of Work	4
1.4 Contributions	6
1.5 Thesis Structure	7
Chapter 2 – Theoretical Foundations	8
2.1 Transmission Line Parameters	8
2.2 Transmission Line Impedance Matrix	10
2.2.1 Carson’s Impedance Formulation for a Uniform Soil	10
2.2.2 Wise’s Impedance Formulation for a Uniform Soil	13
2.3 Transmission Line Admittance Matrix	14
2.3.1 Potential Coefficients Over a Perfect Soil	15
2.3.2 Wise’s Potential Coefficients Formulation For a Uniform Soil	16
2.3.3 Shunt Admittance Matrix Calculation	16
2.4 Line Parameters for Equivalent Phase Conductors	17
2.4.1 Bundle Reduction	17
2.4.2 Kron Reduction	20
2.5 Symmetrical Components for Ideally Transposed Three-phase Transmission Lines	20

2.6	Symmetrical Components for Ideally Transposed Double-circuit Transmission Lines	23
2.6.1	Nine-section Transposition Scheme for Double-circuit Transmission Lines	23
2.6.2	Three-section Transposition Scheme for Double-circuit Transmission Lines	27
2.6.2.1	Barrels Rolled in Opposite Direction	27
2.6.2.2	Barrels Rolled in Same Direction	29
2.7	Modal Parameters for Untransposed Lines	31
2.8	Soil Modeling	33
2.8.1	Wenner Method	33
2.8.2	Multilayered Soil Models	34
2.8.3	Frequency-dependent Soil Properties	37
2.8.4	Soil Frequency Regions and Critical Frequency	38
2.9	Chapter Summary	39
Chapter 3 – Power System Description and Circuit Model Approach		41
3.1	Power System Description	41
3.2	Silves-Oriximiná Transmission Line	43
3.3	Silves-Oriximiná Transmission Line Soil Analysis	44
3.4	EMTP/ATP Circuit Model for Each Transmission Line Span	47
3.5	Validation of Silves-Oriximiná Transmission Line Modeling in EMTP/ATP . . .	49
3.5.1	Silves Substation	50
3.5.2	Oriximiná Substation	52
3.6	Chapter Summary	54
Chapter 4 – Propagation Parameters Study		56
4.1	Soil Influences on Symmetrical Components	56
4.2	Transposition Scheme Influences on Symmetrical Components	59
4.3	Symmetrical Components <i>versus</i> Modal Parameters	61
4.3.1	Equivalent Kron-reduced System	61
4.3.2	Complete System (Shield Wires Modeled Explicitly)	65
4.4	Chapter Summary	69
Chapter 5 – Transient Fault Study		72
5.1	General Study Description	72
5.2	EMTP/ATP Circuit Model for the Transient Study	73
5.3	Influence of Soil Properties on Fault Study	74
5.3.1	Fault Branch Currents	75

5.3.2	Substation Contribution Currents	78
5.4	Influence of Conductor Transposition on Fault Study	82
5.4.1	Faulted Branch Currents	83
5.4.2	Substations Contribution Currents	86
5.5	Influence of Shield Wires Modeling on Fault Study	88
5.5.1	Fault Branch Currents	88
5.5.2	Substations contribution currents	91
5.6	Chapter Summary	92
Chapter 6 – Conclusions and Future Works		95
References		99
Appendix A – Soil Resistivity Measurements		105

LIST OF FIGURES

2.1	Two-port circuit transmission line schematic.	8
2.2	Two-wire configuration located in air above homogenous earth.	11
2.3	Transmission line phase composed of k subconductors distributed symmetrically on a circumference with radius R	18
2.4	Three-section transposition scheme for a three-phase single circuit transmission line.	21
2.5	Nine-section transposition scheme for double-circuit transmission line.	24
2.6	Three-section transposition scheme with barrels rolled in opposite direction for a double-circuit transmission line.	28
2.7	Three-section transposition scheme with barrels rolled in same direction for double-circuit transmission line.	30
2.8	Diagram of Wenner method for measurement of soil apparent resistivity. The probes C1, C2, P1, and P2 are inserted at c meters depth and are positioned spaced by a meters. The electrode spacing a is numerically equal to the soil reading depth.	34
2.9	Real soil (a); and horizontally layered model described by parameters $[\rho_1; \rho_2; \rho_3; \rho_4]$ and $[h_1; h_2; h_3; h_4]$ (b).	35
2.10	N -layered horizontal soil model.	36
2.11	Comparison between constant and frequency-dependent soil properties from 1 Hz up to 1 MHz: (a) conductivity (σ_g) and (b) relative permittivity (ϵ_{rg}) for $\sigma_{g,LF} = 0.001$ [S/m].	37
3.1	Single-line diagram of the Brazilian northern power grid.	41

3.2	Power transmission network map. The lines in red represent 500 kV transmission lines, the ones in green represent 230 kV transmission lines, and the black rectangles represent the substations.	42
3.3	Visualization of the vegetation and the transmission line right-of-way through the Amazon rainforest.	43
3.4	500 double-circuit Silves-Oriximiná transmission line cross-view.	44
3.5	Real transposition scheme applied in the 500 kV double-circuit Silves-Oriximiná transmission line.	45
3.6	Silves-Oriximiná transmission line map.	46
3.7	Deep-layer soil resistivity along the 500 kV Silves-Oriximiná double-circuit transmission line.	47
3.8	ATPDraw representation of one section (span) of: (a) a three-phase line with one shield wire using Kron reduction simplification, and (b) a three-phase line with an "explicit" shield wire, without Kron simplification. Resistance R_G represents the tower grounding.	48
3.9	Flowchart of the proposed EMTP/ATP computacional implementation.	49
3.10	EMTP/ATP steady-state model representation for Silves-Oriximiná transmission line.	50
3.11	Silves-Oriximiná transmission line currents and voltages under nominal load conditions for the circuit 1 at Silves substation.	51
3.12	Silves-Oriximiná transmission line currents and voltages under nominal load conditions for the circuit 2 at Silves substation.	51
3.13	Silves-Oriximiná transmission line currents and voltages under nominal load conditions for the circuit 1 at Oriximiná substation.	53
3.14	Silves-Oriximiná transmission line currents and voltages under nominal load conditions for the circuit 2 at Oriximiná substation.	53

-
- 4.1 Zero sequence component propagation characteristics considering different soil properties: (a) phase velocity, and (b) attenuation constant. Solid lines represent the CP soil models and dashed lines represent the FD soil models. 57
- 4.2 Zero sequence coupling component propagation characteristics considering different soil properties: (a) phase velocity, and (b) attenuation constant. Solid lines represent the CP soil models and dashed lines represent the FD soil models. . . 58
- 4.3 Positive sequence component propagation characteristics considering different soil properties: (a) phase velocity, and (b) attenuation constant. Solid lines represent the CP soil models and dashed lines represent the FD soil models. . . 58
- 4.4 Zero sequence component propagation characteristics considering different transposition schemes: (a) phase velocity, and (b) attenuation constant. Solid lines represent the CP soil models and dashed lines represent the FD soil models, both with $\rho = 1000 \Omega\text{m}$ and $\varepsilon_{rg} = 3$ 59
- 4.5 Zero sequence coupling component propagation characteristics considering different transposition schemes: (a) phase velocity, and (b) attenuation constant. Solid lines represent the CP soil models and dashed lines represent the FD soil models, both with $\rho = 1000 \Omega\text{m}$ and $\varepsilon_{rg} = 3$ 60
- 4.6 Positive sequence component propagation characteristics considering different transposition schemes: (a) phase velocity, and (b) attenuation constant. Solid lines represent the CP soil models and dashed lines represent the FD soil models, both with $\rho = 1000 \Omega\text{m}$ and $\varepsilon_{rg} = 3$ 61
- 4.7 Ground modes propagation characteristics considering symmetrical components and modal parameters with Kron reduction: (a) phase velocity, and (b) attenuation constant. Solid lines represent the CP soil models and dashed lines represent the FD soil models, both with $\rho = 1000 \Omega\text{m}$ and $\varepsilon_{rg} = 3$ 62
- 4.8 Aerial modes propagation characteristics considering symmetrical components and modal parameters with Kron reduction: (a) phase velocity, and (b) attenuation constant. Solid lines represent the CP soil models and dashed lines represent the FD soil models, both with $\rho = 1000 \Omega\text{m}$ and $\varepsilon_{rg} = 3$ 62

- 4.9 Ground mode normalized by zero sequence component (p_0) for: (a) phase velocity and (b) attenuation constant. Solid lines represent the CP soil models and dashed lines represent the FD soil models, both with $\rho = 1000 \Omega\text{m}$ and $\varepsilon_{rg} = 3$ 64
- 4.10 Aerial modes normalized by zero sequence coupling component ($p_0^{\text{I-II}}$) for: (a) phase velocity and (b) attenuation constant. Solid lines represent the CP soil models and dashed lines represent the FD soil models, both with $\rho = 1000 \Omega\text{m}$ and $\varepsilon_{rg} = 3$ 64
- 4.11 Aerial modes normalized by positive sequence component (p_1) for: (a) phase velocity and (b) attenuation constant, comparing symmetrical domain and modal domain modes. Solid lines represent the CP soil models and dashed lines represent the FD soil models, both with $\rho = 1000 \Omega\text{m}$ and $\varepsilon_{rg} = 3$ 65
- 4.12 Ground modes propagation characteristics considering symmetrical components and modal parameter in a complete system (with "explicit" shield wires): (a) phase velocity, and (b) attenuation constant. Solid lines represent the CP soil models and dashed lines represent the FD soil models, both with $\rho = 1000 \Omega\text{m}$ and $\varepsilon_{rg} = 3$ 66
- 4.13 Aerial modes propagation characteristics considering symmetrical components and modal parameters in a complete system (with "explicit" shield wires): (a) phase velocity, and (b) attenuation constant. Solid lines represent the CP soil models and dashed lines represent the FD soil models, both with $\rho = 1000 \Omega\text{m}$ and $\varepsilon_{rg} = 3$ 67
- 4.14 Modal parameters propagation characteristics normalized by zero sequence component (p_0) considering a complete system (with "explicit" shield wires): (a) phase velocity and (b) attenuation constant, comparing symmetrical domain and modal domain modes. Solid lines represent the CP soil models and dashed lines represent the FD soil models, both with $\rho = 1000 \Omega\text{m}$ and $\varepsilon_{rg} = 3$ 68

- 4.15 Modal parameters propagation characteristics normalized by zero sequence coupling component (p_0^{I-II}) considering a complete system (with "explicit" shield wires): (a) phase velocity and (b) attenuation constant, comparing symmetrical domain and modal domain modes. Solid lines represent the CP soil models and dashed lines represent the FD soil models, both with $\rho = 1000 \Omega\text{m}$ and $\varepsilon_{rg} = 3$ 68
- 4.16 Modal parameters propagation characteristics normalized by positive sequence component (p_1) considering a complete system (with "explicit" shield wires): (a) phase velocity and (b) attenuation constant, comparing symmetrical domain and modal domain modes. Solid lines represent the CP soil models and dashed lines represent the FD soil models, both with $\rho = 1000 \Omega\text{m}$ and $\varepsilon_{rg} = 3$ 69
- 5.1 EMTP/ATP simplified model representation for single-phase faults for (a) simplified model using Kron reduction, and (b) model with explicit shield wires. $R_G = 15 \Omega$ is the tower grounding resistance, $R_f = 0.001 \Omega$ is the fault resistance and $R_{SE} = 1 \Omega$ is the substation grounding resistance. 73
- 5.2 Maximum fault branch current under single-phase fault conditions along the transmission line, considering: (a) constant parameters (CP) soil models, and (b) frequency-dependent (FD) soil models. 76
- 5.3 Normalized fault branch current under single-phase fault conditions along the transmission line, considering: (a) constant parameters (CP) soil models, and (b) frequency-dependent (FD) soil models. 77
- 5.4 Maximum value of contribution currents from Silves and Oriximiná substations measured on the faulted circuit under phase-to-ground fault conditions along the transmission line. Soils are considered invariant-frequency (CP) models. 79
- 5.5 Maximum value of contribution currents from Silves and Oriximiná substations measured on the faulted circuit under phase-to-ground fault conditions along the transmission line. Soils are considered frequency-dependent (FD) models. 80

5.6	Normalized contribution currents from Silves and Oriximiná substations measured on circuit 1 phase A (faulted circuit) in phase-to-ground fault conditions along the transmission line. The model with longitudinal heterogeneous soil is considered as reference and have frequency-dependent (FD) properties.	81
5.7	Proposed nine-section transposition scheme for double-circuit transmission line, with the barrels rotated in opposite direction.	83
5.8	Maximum absolute value of fault branch current under a single-phase fault (Ag) condition, considering all types of transposition schemes. Soils are considered frequency-dependent (FD) models and longitudinal heterogeneous along the right-of-way, as presented in Figure 3.7.	84
5.9	Normalized fault branch current under a single-phase fault (Ag) condition, considering all types of transposition scheme. The real transposition of the 500 kV double-circuit Silves-Oriximiná transmission line is used as a reference (see Figure 3.5). Soils are considered frequency-dependent (FD) models and longitudinal heterogeneous along the right-of-way, as presented in Figure 3.7.	85
5.10	Maximum value of contribution currents from Silves and Oriximiná substations measured on circuit 1 phase A (faulted circuit) under phase-to-ground fault conditions along the transmission line for each transposition scenario. Soils are considered frequency-dependent (FD) models and longitudinal heterogeneous along the right-of-way, as presented in Figure 3.7.	86
5.11	Normalized contribution currents from Silves and Oriximiná substations measured on circuit 1 phase A (faulted circuit) under phase-to-ground fault conditions along the transmission line. The real transposition of the 500 kV double-circuit Silves-Oriximiná transmission line is used as a reference (see Figure 3.5). Soils are considered frequency-dependent (FD) models and longitudinal heterogeneous along the right-of-way, as presented in Figure 3.7.	87
5.12	Maximum absolute value of fault branch current under a single-phase fault condition, considering the simplified system with Kron reduction and the complete system with explicit shield wires.	89

5.13	Maximum shield wire currents under single-phase fault conditions at both terminals substation.	90
5.14	Normalized fault branch current under a single-phase fault (Ag) condition, considering the complete system with explicit shield wires.	90
5.15	Maximum value of contribution currents from Silves and Oriximiná substations measured on the faulted circuit under phase-to-ground fault conditions along the transmission line for the model considering Kron reduction and for the model considering explicit shield wires. Soils are considered frequency-dependent (FD) models and longitudinal heterogeneous along the right-of-way, as presented in Figure 3.7.	91
5.16	Normalized contribution currents from Silves and Oriximiná substations measured on the faulted circuit under phase-to-ground fault conditions along the transmission line for the model considering explicit shield wires. Soils are considered frequency-dependent (FD) models and longitudinal heterogeneous along the right-of-way, as presented in Figure 3.7.	92

LIST OF TABLES

2.1	CIGRE recommendations concerning whether or not the frequency dependence of the soil properties should be considered for different engineering applications.	38
3.1	Specifications of the transmission line conductors	45
3.2	Minimum, average and maximum soil resistivity along the right-of-way.	46
3.3	Relative permittivity range values.	47
3.4	Comparison between simulated and field measured voltages and currents in the Silves-Oriximiná transmission line at Silves substation.	52
3.5	Comparison between simulated and field measured voltages and currents in the Silves-Oriximiná transmission line at Oriximiná substation.	54
5.1	Outline of average discrepancy on fault branch current between the soil models in relation to heterogeneous soil model.	78
5.2	Outline of average discrepancy on substations contribution currents for the different CP soil models.	79
5.3	Outline of average discrepancy on substations contribution currents for the different FD soil models.	81
5.4	Outline of average discrepancy on fault branch current between the transposition schemes in relation to the real transposition scheme.	84
5.5	Outline of average discrepancy on substations contribution currents between the transposition schemes concerning the real transposition scheme for the faulted circuit.	88

A.1	Real data from apparent soil resistivity measurements along the path of the 500 kV Silves-Oriximiná transmission line.	105
A.1	Real data from apparent soil resistivity measurements along the path of the 500 kV Silves-Oriximiná transmission line.	106
A.1	Real data from apparent soil resistivity measurements along the path of the 500 kV Silves-Oriximiná transmission line.	107
A.1	Real data from apparent soil resistivity measurements along the path of the 500 kV Silves-Oriximiná transmission line.	108
A.2	Average and deep layer resistivity obtained from the apparent resistivity data presented in Table A.1.	109
A.2	Average and deep layer resistivity obtained from the apparent resistivity data presented in Table A.1.	110
A.2	Average and deep layer resistivity obtained from the apparent resistivity data presented in Table A.1.	111
A.2	Average and deep layer resistivity obtained from the apparent resistivity data presented in Table A.1.	112

LIST OF SYMBOLS

ε_r	Relative electric permittivity	[p.u.]
ε_{rg}	Relative soil electric permittivity	[p.u.]
a	Electrode spacing in the Wenner array	[m]
c	Electrode insertion depth in the Wenner array	[m]
I_W	Test current between terminals C1 and C2 in the Wenner array	[A]
V_W	Voltage drop between terminals P1 and P2 in the Wenner array	[V]
N	Relative soil electric permittivity	[p.u.]
\hat{J}_0	Bessel function of first kind and order zero	
\hat{H}_1	Struve function of the first kind	
ρ_g	Soil resistivity	[Ωm]
ε	Electric permittivity	[F/m]
μ	Magnetic permeability	[H/m]
ρ	Electrical resistivity	[Ωm]
I	Electrical current	[A]
ℓ	Transmission line length	[m]
$Z_{i,j}$	Mutual impedance between conductors i and j	[Ω]
ω	System angular frequency	[rad/s]
ε_0	Vacuum electric permittivity ($\approx 8.85 \times 10^{-12}$)	[F/m]
μ_0	Free space magnetic permeability ($= 4\pi \times 10^{-7}$)	[H/m]

$Z_{i,i}$	Self impedance of conductor i	$[\Omega/\text{m}]$
$Z_{s,int}$	Internal part of conductor self impedance	$[\Omega/\text{m}]$
$Z_{s,ext}$	External part of conductor self impedance	$[\Omega/\text{m}]$
R_{AC}	Conductor ohmic AC resistance	$[\Omega/\text{m}]$
r_{ext}	Conductor external radius	$[\text{m}]$
Q_i	Charge per unit length of the i^{th} conductor	$[\text{C}/\text{m}]$
V	Voltage relative to the earth	$[\text{V}]$
$P_{i,j}$	Mutual potential coefficient between conductors i and j	$[\text{m}/\text{F}]$
$P_{i,i}$	Self potential coefficient of conductor i	$[\text{m}/\text{F}]$
Z	Series impedance	$[\Omega]$
Y	Shunt admittance	$[\text{S}]$
Z_c	Characteristic (or surge) impedance	$[\Omega]$
γ	Propagation constant	$[\text{m}^{-1}]$
α	Attenuation constant	$[\text{Np}/\text{m}]$
β	Phase constant	$[\text{rad}/\text{m}]$
v	Phase velocity	$[\text{m}/\text{s}]$
λ	Wavelength	$[\text{m}]$
\mathbf{Z}	Series impedance matrix of the transmission line	$[\Omega/\text{m}]$
\mathbf{P}	Matrix of potentials of the transmission line	$[\text{m}/\text{F}]$
\mathbf{Y}	Shunt admittance matrix of the transmission line	$[\text{S}/\text{m}]$
\mathbf{S}	Fortescue transformation matrix	
\mathbf{Z}_{012}	Sequence domain impedance matrix of the transmission line	$[\Omega/\text{m}]$
\mathbf{Y}_{012}	Sequence domain admittance matrix of the transmission line	$[\text{S}/\text{m}]$
\mathbf{T}_V	Modal matrix associated to the matrix product $\mathbf{Y} \cdot \mathbf{Z}$	

Λ_k	k^{th} eigenvalue of $\mathbf{Y} \cdot \mathbf{Z}$	
$\mathbf{T}_{V,k}$	k^{th} column of modal matrix \mathbf{T}_V	
\mathbf{Z}_M	Modal series impedance matrix of the transmission line	$[\Omega/\text{m}]$
\mathbf{Y}_M	Modal shunt admittance matrix of the transmission line	$[\text{S}/\text{m}]$
τ	Transmission line travel time	$[\text{s}]$
σ	Electrical conductivity	$[\text{S}/\text{m}]$
F_Z	Impedance correction factor	
F_Y	Admittance correction factor	
\mathbf{Z}'_{ABC}	Equivalent series impedance matrix of the transmission system	$[\Omega/\text{m}]$

GLOSSARY

ATP	Alternative Transients Program
CIGRE	Conseil International des Grands Réseaux Électriques
LEC	Lechuga Substation
LCC	Line/Cable Constants
EMI	Electromagnetic interference
EMTP	Electromagnetic Transients
EMT	Electromagnetic Transients Program
SIL	Silves Substation
TL	Transmission line
ORX	Oriximiná Substation

1.1 PREFACE

The field of electrical power transmission and distribution plays a crucial role in ensuring reliable and efficient delivery of electricity from power generation sources to end consumers. Transmission lines are a main component of any transmission system, which directly affects the energy supply of entire regions, thus required to be robust and reliable structures. Moreover, transmission lines demand vast use of external spaces, being often exposed to interferences in its vicinities, as well as adverse operating conditions caused by weather among other factors, which may give cause to faults and, ultimately, power supply interruptions.

The restrictive environmental regulations regarding the use of space increased cases of double-circuit transmission lines due to this type of transmission line being able to accommodate two circuits in the same right-of-way, it allows for transmitting double the electrical power using practically the same space. However, this type of transmission line poses some difficulties, mainly related to the existence of electromagnetic coupling between the two circuits present in it. This inter-circuit coupling primarily impacts the protection and fault location systems, which has motivated various recent researches in this area (LOPES *et al.*, 2021; FEDOROV *et al.*, 2022; GIL *et al.*, 2021; YU JUNJUN WU, 2022).

A technique employed in overhead double-circuit transmission lines to minimize the effects of mutual coupling and electromagnetic interference between the circuits is the conductor transposition. Currents flowing in an energized conductor produce a time-varying magnetic field. This time-varying magnetic field causes electromotive forces which, on their turn, induce voltages and currents on a metallic structure laid parallelly to the energized conductor, such as shield wires. Then, rearranging the position of conductors within a transmission line extension reduces the electromagnetic fields generated by the currents flowing in phases (MONTEIRO,

2004).

The fact that the lines have conductor transposition and the shield wires are solidly grounded at each transmission tower allows assuming that no currents flow through the shield wires, thus simplifications, such as Kron reduction and symmetric-domain, to be performed to assist in the calculation of electromagnetic transient (EMT) studies (LOPES *et al.*, 2021; FEDOROV *et al.*, 2022; GIL *et al.*, 2021; YU JUNJUN WU, 2022).

Another simplification and recognized source of error that may affect the calculation of EMT is the uncertainty of the soil electrical resistivity (DAS *et al.*, 2014). Indeed, actual soils are anisotropic media, *i.e.* their properties vary with direction and depth (HE *et al.*, 2012). Nevertheless, Carson’s equation expresses its influence on the classical coupling model by a uniform parameter ρ (CARSON, 1926). Besides, designers often adopt typical values from soil tables, rather than having resistivity surveys and building accurate soil models (WHELAN J.M; HANRATTY, 2010).

Moreover, the presence of lossy soil below overhead transmission lines introduces additional complexities to the analysis of modal parameters and EMT studies. Soil characteristics, such as resistivity and permittivity, can significantly affect the propagation of electromagnetic waves, leading to changes in the line’s modal parameters, including characteristic impedances, propagation constants, and constant attenuation factors. Considering the impact of lossy soil is crucial for accurately modeling and simulating transmission lines, especially when studying electromagnetic transients and transient stability phenomena (ALÍPIO; VISACRO, 2014; HE *et al.*, 2012; PAPADOPOULOS *et al.*, 2010).

In this work, a comprehensive investigation is conducted on symmetrical, modal parameters and EMT of a double-circuit transmission line. The study aims to provide a deeper understanding of the effects of conductor transposition, shield wires, and lossy soil on the behavior of the line under single-phase faults situations. All studies evaluated are based on a transmission line in the state of Amazonas, Brazil, which is part of a complex interconnected transmission system. Field data from this power line are used and modeled according to the project and construction reports of the company holding the installation concession, such as: soil resistivity along the right-of-way, cross-section, transposition type, and power flow.

1.2 REVIEW OF THE SPECIALIZED LITERATURE

Electromagnetic transient studies in power systems requires models that accurately consider the overhead transmission line parameters over a wide frequency range. The first approach proposed by Carson (1926), widely implemented in EMTP-based softwares, utilizes earth correction terms to account for the imperfect earth influence on conductor impedance. However, this approach is limited to cases where displacement current and earth conduction effects are negligible.

Numerous efforts have been made to develop accurate models for earth impedance calculation, involving rigorous solutions with infinite integrals that can be evaluated using infinite series or numerical integration methods (HOFMANN, 2003; PAPAGIANNIS *et al.*, 2005). These methods have been validated against finite element method (FEM) results (PAPAGIANNIS *et al.*, 2005; TRIANTAFYLLIDIS *et al.*, 1999; PAPAGIANNIS *et al.*, 2000). However, researchers often seek simplifications through closed-form expressions based on complex depth approximation or other solutions for the infinite integral terms (Deri, A., Tevan, 1981; RACHIDI *et al.*, 1999; NODA, 2006; THEODOULIDIS, 2015).

Alternative models have been proposed to extend the applicability to higher frequencies and consider earth conduction effects on shunt admittances (WISE, 1931; WISE, 1934; WISE, 1948). An attempt to find an exact solution to the problem was also proposed by Kikuchi (1956), which uses an exact solution considering the transition from quasi-TEM to surface wave guide propagation, while Pettersson (1994) approximated Kikuchi's and Wise's formulations with logarithmic expressions for numerical evaluation.

In all the aforementioned works, the electrical properties of soil, such as conductivity and permittivity, are assumed to be constant, despite the well-established fact that they exhibit frequency-dependent behavior almost a century ago (WG-C4.33, 2019; SMITH-ROSE, 1933; SCOTT, 1966). Due to the complex composition of soil and the multitude of variables influencing its behavior under electromagnetic fields, modeling the frequency dependence of soil presents a significant scientific challenge. First, the frequency dependence of soil properties in high-frequency range has been established by Smith-Rose (1933) and Scott (1966) through laboratory measurements, which has been further confirmed by field measurements (WG-C4.33,

2019; VISACRO *et al.*, 2011; VISACRO; ALIPIO, 2012). In 1975, Longmire & Smith (1975) proposed the first semi-theoretical model, building upon Scott's laboratory method. Later, Portela (1999) developed a similar semi-theoretical model, incorporating a statistical approach that mostly applied to lightning protection. Recently, other expressions for the frequency dependence of soil parameters have been proposed by Visacro and Alipio, based on their own field measurements of grounding harmonic impedance (VISACRO; ALIPIO, 2012; ALIPIO; VISACRO, 2013; ALÍPIO; VISACRO, 2014).

Within the electromagnetic studies reported in the literature, it is common for the current flowing in the shield wires to be disregarded due to the use of phase conductor transposition, allowing for the utilization of Kron reduction. In Dommel & Bhattacharya (1992) and Portela & Tavares (2002), it was shown that transmission lines considered ideally transposed do not accurately represent a transposed transmission line throughout the frequency spectrum. In 2006, Elguera & Tavares (2006) demonstrated the influence of representing a real transposition of a transmission line under electromagnetic transient studies.

In Martins-Britto (2020), it is proposed a heterogeneous transmission line implementation using EMTP-type software, focusing on studies of electromagnetic interference involving transmission lines and neighboring metallic pipelines. Additionally, EMTP/ATP software tools employ simplified formulations that do not consider dispersive soils with frequency-dependent parameters.

Despite transmission line modeling being extensively studied, the studies reported in the literature often develop complex models for specific topics of interest, while simplifying other aspects of the analysis. Studies focused on grounding and lightning protection typically concentrate on improved soil models, considering heterogeneous and frequency-dependent soils. However, the modeling of the transmission line itself is simplified, often considering only one tower and its grounding (ALIPIO; VISACRO, 2013; VISACRO; ALIPIO, 2012). In transmission line protection system studies, simplified Kron-reduced models are commonly verified due to the use of transformation matrices, with homogeneous and frequency-independent soils considered (FEDOROV *et al.*, 2022; LOPES *et al.*, 2021; GIL *et al.*, 2021). Finally, in electromagnetic interference studies, a common approach using a transmission line model with explicit shield wires is observed, but with constant soil properties and uniform equivalent models repre-

senting earth structures with N-layers (MARTINS-BRITTO *et al.*, 2020; MARTINS-BRITTO, 2020).

Thus, to the best of the author’s knowledge, there is no report in the specialized literature accounting for transmission lines under a circuit theory EMTP-based approach with longitudinal heterogeneities along the right-of-way, *i.e.* span-wise modeling, using formulations for impedance and admittance calculations that consider lossy soils with frequency-dependent properties, in which all these improvements are built and modeled in a same EMTP/ATP framework.

1.3 OBJECTIVES AND SCOPE OF WORK

To address the aforementioned gaps in the literature e provide a comprehensive study, this work aims to build a realistic circuit model implementation to represent transmission lines operating on real power plant grids, considering real constructive aspects on the same modeling, such as: conductor transposition, soil properties and shield wires. In addition, this work develop an analysis of the impact of transposition scheme, shield wires and the variation of soil resistivity on the modal parameters and symmetrical components of double-circuit transmission line.

Intended to avoid the limitations of Carson’s formula, impedances and admittances are calculated considering the influence of conductive and displacement current in propagation media along the entire frequency spectrum investigated. In addition, the frequency-dependent soil properties are adopted.

The studies are performed based on the interconnection transmission lines of the Oriximiná, Silves, and Lechuga substations located in the North region of Brazil. The transmission lines between these substations are a triangular double-circuit and operate at 500 kV level. This goal can be broken down into the following specific objectives:

1. Implementation of complex transmission lines, on EMTP-based software, considering frequency-dependent and wave propagation in conductors;
2. Implementation of a model that allows the variation of physical and geometric parameters during the right-of-way path, such as electrical resistivity of the soil, grounding resistance

of the towers, and conductor arrangement of the line, for example;

3. Improvement of the impedance and admittance calculations used in EMTP-based software, to use formulas that consider current dispersion in the soil, including lossy soils parameters;

With the products of this thesis, it is possible to carry out a variety of relevant tasks related to EMT studies, with improved accuracy, involving realistic models of complex systems, such as:

- Analysis of fault transients in a real double-circuit transmission line that constitutes the northern system of Brazil;
- Analysis of propagation parameters for the symmetric components and the validity region of these parameters for representing electromagnetic phenomena in double-circuit transmission lines;
- Analysis of correctly modeling shield wires and their impacts on the short-circuit levels of double-circuit transmission lines.

1.4 CONTRIBUTIONS

With respect to peer review and publication of results related to this master's thesis research, the following papers are selected and listed in chronological order and of importance:

1. MORAES, C. M.; MATOS, G. H. S.; MARTINS-BRITTO, A. G.; LOPES, F. V.; SILVA, K. M., "Total AC Interferences Between a Power Line Subject to a Single-Phase Fault and a Nearby Pipeline With Multilayered Soil", in *IEEE Transactions on Electromagnetic Compatibility*, vol. 65, no. 2, pp. 585-594, April 2023.
2. MORAES, C. M.; MARTINS-BRITTO, A. G.; LOPES, F. V.; SILVA, K. M.; RIBEIRO, E. P. A.; RODRIGUES, M. A. M. "On the Effects of EMI and the Soil Structure on Transmission Line Parameters — Part I: Theoretical Model", *2021 Workshop on Communication Networks and Power Systems (WCNPS)*, 2021, pp. 1-6.

3. MORAES, C. M.; MARTINS-BRITTO, A. G.; LOPES, F. V.; SILVA, K. M.; RIBEIRO, E. P. A.; RODRIGUES, M. A. M. "On the Effects of EMI and the Soil Structure on Transmission Line Parameters — Part II: Impacts on Fault Locators", *2021 Workshop on Communication Networks and Power Systems (WCNPS)*, 2021, pp. 1-6.
4. MORAES, C. M.; MARTINS-BRITTO, A. G.; LOPES, F. V.; SILVA, K. M.; RIBEIRO, E. P. A.; RODRIGUES, M. A. M. "Influences of Electromagnetic Interferences on Two-Terminal Impedance-Based Fault Location Methods", 2022, *IX Simpósio Brasileiro de Sistemas Elétricos (SBSE 2022)*, pp. 1-6.
5. MORAES, C. M.; MARTINS-BRITTO, A. G.; BRITO RIBEIRO, M. A. "On the effective length of transmission line grounding conductors and the validity of the point-source model in GPR responses", *2022 Workshop on Communication Networks and Power Systems (WCNPS)*, 2022, pp. 1-6.

The articles titled "*On the Effects of EMI and the Soil Structure on Transmission Line Parameters — Part II: Impacts on Fault Locators*" and "*On the effective length of transmission line grounding conductors and the validity of the point-source model in GPR responses*" are the winner of the Best Paper Award Prize at the 2021 Workshop on Communication Networks and Power Systems (WCNPS) and 2022 Workshop on Communication Networks and Power Systems (WCNPS) conferences, respectively.

1.5 THESIS STRUCTURE

The current chapter highlights the context under which the research is inserted and its relevance and describes the objectives, scope of work, and main contributions of this thesis.

Chapter 2 provides the theoretical basis related to transmission line parameters and fundamental equations of modal parameters, lossy soil formulations, apparent resistivity measurement analysis, and transposition scheme.

Chapter 3 presents the power system description and circuit model approach, focusing on the 500 kV double-circuit transmission line between Silves and Oriximiná in Northern Brazil. Detailed constructive aspects, including conductor arrangement and shield wires, are provi-

ded. The chapter explores challenges posed by dense vegetation and analyzes soil resistivity variations along the transmission right-of-way.

Chapter 4 examines the propagation parameters in a double-circuit transmission line. The study focuses on variations in soil properties, transposition methods, and a comparison between two distinct approaches for representation of the shield wires, namely: (1) using simplified Kron-reduced equivalent Z and Y matrices; and (2) using explicit representations of the shield wires via modal components.

Chapter 5 focuses on analyzing various scenarios of short circuits in the 500 kV Silves-Oriximiná transmission line considering models that were chosen based on the theoretical studies from the previous chapter. The study evaluates the impact of soil properties, transposition schemes, and shield wires on short-circuit levels. A total of 1500 short-circuit cases are analyzed, considering single-phase faults along circuit 1 while keeping circuit 2 under nominal conditions.

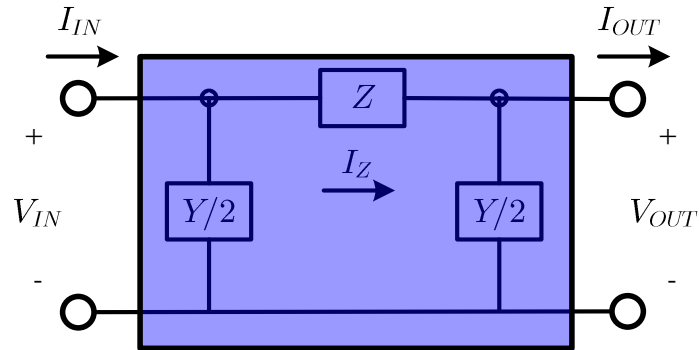
Chapter 6 exposes the final considerations and points directions for the future continuity of this work.

THEORETICAL FOUNDATIONS

2.1 TRANSMISSION LINE PARAMETERS

Considering the solutions of the equations that relate the voltages and currents at the transmission line terminals, represented by the two-port circuit in Figure 2.1, it is possible to obtain the wave propagation parameters for the transmission lines, as follows (DOMMEL; BHATTACHARYA, 1992; MONTEIRO, 2004):

Figure 2.1. Two-port circuit transmission line schematic.



Source: Own authorship.

$$\begin{bmatrix} V_{IN} \\ I_{IN} \end{bmatrix} = \begin{bmatrix} \cosh(\gamma L) & Z_c \cdot \sinh(\gamma L) \\ \frac{\sinh(\gamma L)}{Z_c} & \cosh(\gamma L) \end{bmatrix} \cdot \begin{bmatrix} V_{OUT} \\ I_{OUT} \end{bmatrix}, \quad (2.1)$$

with

$$Z_c = \sqrt{\frac{Z}{Y}}, \quad (2.2)$$

$$\gamma = \sqrt{ZY} = \alpha + j\beta, \quad (2.3)$$

$$v = \frac{\omega}{\beta}, \quad (2.4)$$

$$\lambda = \frac{2\pi}{|\gamma|}, \quad (2.5)$$

in which: L is the total transmission line length, given in [m]; Z_c is the characteristic impedance, in [Ω]; λ is the propagation constant, in [m^{-1}]; α is the attenuation constant, given in [Np/m]; β is the phase constant, in [rad/m]; v is the phase velocity, in [m/s]; λ is the wavelength, expressed in [m]; and $\omega = 2\pi f$ is the angular frequency, in [rad/s].

The equation (2.1) can be rewritten in terms of the series impedance and shunt admittance matrix of the transmission line, resulting in the well-known classical nominal- π of the transmission line, as depicted in Figure 2.1:

$$\begin{bmatrix} V_{IN} \\ I_{IN} \end{bmatrix} = \begin{bmatrix} 1 + \frac{YZ}{2} & Z \\ Y \cdot (1 + \frac{YZ}{4}) & 1 + \frac{YZ}{2} \end{bmatrix} \cdot \begin{bmatrix} V_{OUT} \\ I_{OUT} \end{bmatrix}. \quad (2.6)$$

This solution leads to the well-known classical nominal- π representation of the transmission line, in which \mathbf{Z} and \mathbf{Y} are the series impedance and shunt admittance matrices, respectively (DOMMEL; BHATTACHARYA, 1992; MONTEIRO, 2004).

Although the classical nominal- π model is not valid to represent long transmission lines, the solutions presented in this section remain valid, without loss of generality for the equivalent- π model, by using the appropriate correction factors (F_Z and F_Y) in terms of the propagation constant and line length, in the following forms (DOMMEL; BHATTACHARYA, 1992; MONTEIRO, 2004):

$$Z_{equivalent-\pi} = Z_{nominal-\pi} F_Z, \quad (2.7)$$

$$\frac{Y_{equivalent-\pi}}{2} = \frac{Y_{nominal-\pi}}{2} F_Y, \quad (2.8)$$

in which F_Z is the correction factor for series impedance and F_Y is the shunt admittance correction factor, both determined by:

$$F_Z = \frac{\sinh(\gamma\ell)}{\gamma\ell}, \quad (2.9)$$

$$F_Y = \frac{\tanh(\frac{\gamma\ell}{2})}{\frac{\gamma\ell}{2}}. \quad (2.10)$$

2.2 TRANSMISSION LINE IMPEDANCE MATRIX

The voltage drop along a transmission line, presented in Figure 2.1, can be expressed as phasor equations for AC steady-state conditions at a specific frequency. Considering a transmission line with N conductors, the voltage drop is given by (DOMMEL; BHATTACHARYA, 1992):

$$-\begin{bmatrix} \frac{\partial V_1}{\partial x} \\ \frac{\partial V_2}{\partial x} \\ \frac{\partial V_3}{\partial x} \\ \vdots \\ \frac{\partial V_N}{\partial x} \end{bmatrix} = \begin{bmatrix} Z_{1,1} & Z_{1,2} & Z_{1,3} & Z_{1,k} & \dots & Z_{1,N} \\ Z_{2,1} & Z_{2,2} & Z_{2,3} & Z_{2,k} & \dots & Z_{2,N} \\ Z_{3,1} & Z_{3,2} & Z_{3,3} & Z_{3,k} & \dots & Z_{3,N} \\ \vdots & \vdots & \vdots & \vdots & \ddots & \vdots \\ Z_{N,1} & Z_{N,2} & Z_{N,3} & Z_{N,k} & \dots & Z_{N,N} \end{bmatrix} \cdot \begin{bmatrix} I_1 \\ I_2 \\ I_3 \\ \vdots \\ I_N \end{bmatrix} = \quad (2.11)$$

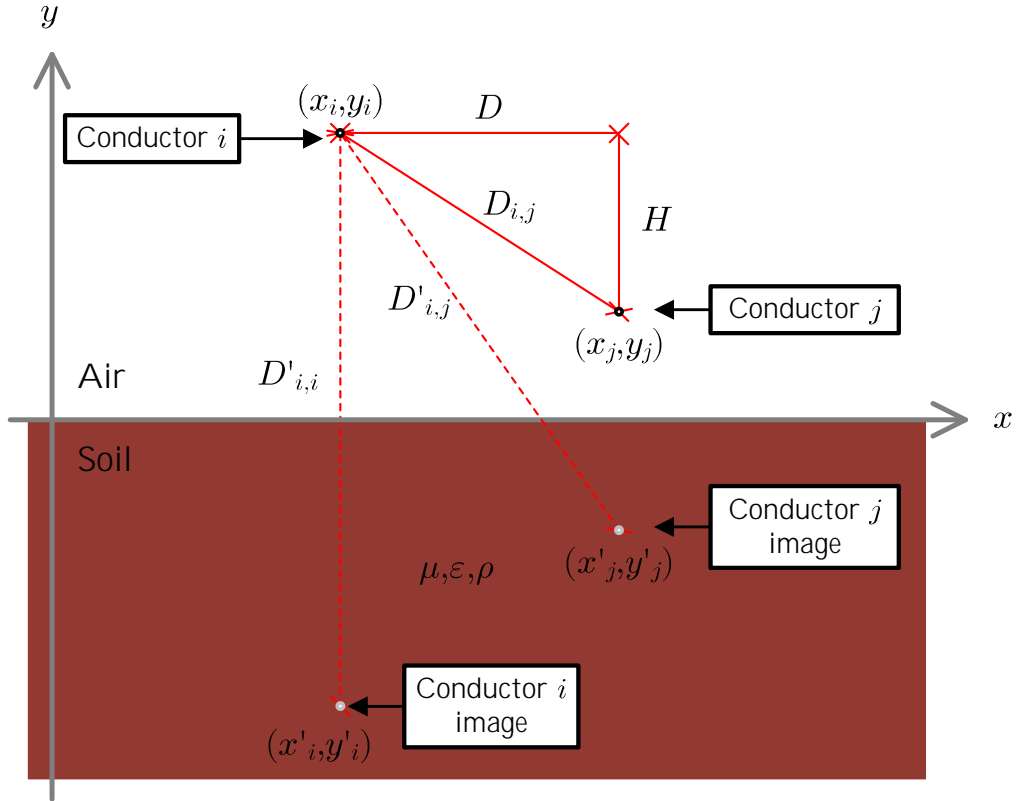
$$-\frac{\partial \mathbf{V}}{\partial x} = \mathbf{Z} \cdot \mathbf{I}, \quad (2.12)$$

in which $\mathbf{V} = [V_1, V_2, \dots, V_N]$ is the vector of phasor voltages, measured from conductors 1, 2, \dots , N to the reference, in [V], and $\mathbf{I} = [I_1, I_2, \dots, I_N]$ is the vector of phasor currents flowing in the conductors 1, 2, \dots , N , in [A]. The matrix \mathbf{Z} is called the series impedance matrix, and it is symmetric and complex.

2.2.1 Carson's Impedance Formulation for a Uniform Soil

Considering the system presented in Figure 2.2, composed of two parallel conductors i and j over uniform soil described by resistivity ρ , permittivity ε and permeability μ , the off-diagonal elements $Z_{i,j}$ of the series impedance matrix \mathbf{Z} correspond to the mutual impedances between conductors i and j with ground return path, computed in [Ω/m] using Carson's equation (2.13) (CARSON, 1926):

$$Z_{i,j} = \frac{j\omega\mu_0}{2\pi} \ln \left(\frac{D'_{i,j}}{D_{i,j}} + J_m \right), \quad (2.13)$$

Figure 2.2. Two-wire configuration located in air above homogenous earth.

Source: Adapted from (MARTINS-BRITTO, 2020).

$$J_m = \int_0^{\infty} \frac{2e^{-H\lambda}}{\lambda + \sqrt{\lambda^2 + j\frac{\omega\mu_0}{\rho} - \omega^2\mu_0\epsilon_0\epsilon_r}} \cos(\lambda D) d\lambda, \quad (2.14)$$

in which $\mu_0 = 4\pi \times 10^{-7}$ [H/m] is the magnetic permeability constant in free space, $\epsilon_0 \approx 8.85 \times 10^{-12}$ [F/m] is the vacuum electrical permittivity, ρ is the local soil electrical resistivity, in [Ωm], ϵ_r is the local soil relative electrical permittivity, H , D , $D_{i,j}$ and $D'_{i,j}$ are the relative distances represented in Figure 2.2, in [m], with:

$$H = y_i + y_j, \quad (2.15)$$

$$D = x_j - x_i, \quad (2.16)$$

$$D_{i,j} = \sqrt{(x_j - x_i)^2 + (y_i - y_j)^2}, \quad (2.17)$$

$$D'_{i,j} = \sqrt{(x_j - x_i)^2 + (y_i + y_j)^2} \quad (2.18)$$

being $[x_N, y_N]$, $N = 1, 2, \dots, i, \dots, j, \dots, N$ are the coordinates of N -th conductor. As most soil types are nonmagnetic, permeability μ is assumed to be equal to the free space value μ_0 (TSIAMITROS *et al.*, 2008a; TSIAMITROS *et al.*, 2008b).

Elements $Z_{i,i}$ in the main diagonal are the self-impedances of the aboveground conductors. The self-impedance is composed of internal and external parts, both given in $[\Omega/\text{m}]$, as follows:

$$Z_{i,i} = Z_{i,i}^{int} + Z_{i,i}^{ext}. \quad (2.19)$$

The internal component $Z_{i,i}^{int}$ depends on the characteristics and geometry of the conductors. For stranded or solid tubular conductors, the internal self impedance is the AC ohmic resistance R_{AC} corrected to the conductor operating temperature, skin, and proximity effect, normally supplied by the manufacturer or calculated directly from the DC ohmic resistance (WHELAN J.M; HANRATTY, 2010).

The external self impedance $Z_{i,i}^{ext}$ is related to the ground return path impedance and is determined by setting $j = i$, $D_{i,i} = r_i$, $D'_{i,i} = 2|y_i|$ and $D = 0$, while J_m is denoted as J_s , in (2.13)-(2.14), resulting in:

$$Z_{i,i}^{ext} = \frac{j\omega\mu_0}{2\pi} \ln \left(\frac{2|y_i|}{r_i} + J_s \right), \quad (2.20)$$

$$J_s = \int_0^\infty \frac{2e^{-2|y_i|\lambda}}{\lambda + \sqrt{\lambda^2 + j\frac{\omega\mu_0}{\rho} - \omega^2\mu_0\varepsilon_0\varepsilon_r}} \cos(\lambda D) d\lambda, \quad (2.21)$$

in which $|y_i|$ is the height of the i -th conductor, given in [m], and r_i is the external radius of conductor i , given in [m].

The first terms present in Carson's equations, denoted in 2.13 and 2.20, correspond to the ground return impedance for a perfectly conductive soil. The improper integrals in (2.14) and in (2.21), denoted as J_m and J_s respectively, represent the effects of the soil with finite resistivity, including losses caused by current return.

However, the solution found by Carson imposes challenges in pursuing its solution. The integrals J_m and J_s show both regular and irregular oscillations due to the cosine and the exponential terms. To overcome these oscillations, alternate solutions have been assessed by

several researchers using numerical techniques based on quadratures, power series expansion, or deduction of simplified expressions, being worth mentioning the formulas derived by Carson-Clem, Deri, Lucca, and Ametani (WG-36.02, 1995; Deri, A., Tevan, 1981; LUCCA, 1994; AMETANI *et al.*, 2009). The use of simplified formulas is convenient but may introduce significant errors if the particularities of the interference problem under study are not well understood. In general, these expressions produce satisfactory results for low frequencies and relatively small spacings between conductors, which imposes a limitation on the calculation model.

According to Theodoulidis (2015), Carson's integral can be evaluated analytically, with floating-point precision and without convergence problems, employing a closed-form solution, *i.e.* expressed in terms of one or more functions whose behavior is well known. Indeed, the integrals in (2.13) and (2.20) can be written as (2.22) with the variable change expressed as shown in (2.23) and (2.24):

$$\int_0^{\infty} \frac{2e^{-H\lambda}}{\lambda + \sqrt{\lambda^2 + j\frac{\omega\mu_0}{\rho} - \omega^2\mu_0\varepsilon_0\varepsilon_r}} \cos(\lambda D) d\lambda = \frac{\pi}{2u_1} [\widehat{H}_1(u_1) - \widehat{Y}_1(u_1)] - \frac{1}{u_1^2} + \frac{\pi}{2u_2} [\widehat{H}_1(u_2) - \widehat{Y}_1(u_2)] - \frac{1}{u_2^2}, \quad (2.22)$$

$$u_1 = (H - jD) \sqrt{j\frac{\omega\mu_0}{\rho} - \omega^2\mu_0\varepsilon_0\varepsilon_r}, \quad (2.23)$$

$$u_2 = (H + jD) \sqrt{j\frac{\omega\mu_0}{\rho} - \omega^2\mu_0\varepsilon_0\varepsilon_r}, \quad (2.24)$$

in which \widehat{H}_1 is the Struve function and \widehat{Y}_1 is the Bessel function of the second type, both of first order (THEODOULIDIS, 2015).

Although Carson's formulation is widely used in the literature and is assumed in various electromagnetic transients programs, including well-established software such as Line/Cable Constants (LCC) from the Alternate Transient Program (ATP), the calculation is based on three specific assumptions that serve as restrictions: (1) The soil permeability is equal to the free space; (2) the wave propagates at the speed of light without any attenuation, and (3) the wave is propagated at a low frequency that displacement currents can be neglected (WISE, 1931; WISE, 1934; WISE, 1948).

2.2.2 Wise's Impedance Formulation for a Uniform Soil

To overcome Carson's limitations formula, Wise proposed a generalized formulation for impedance and admittance formulas, by taking into account the influence of the conductive and displacement current in all propagation media (WISE, 1931; WISE, 1934; WISE, 1948). This generalized formula for mutual impedance is:

$$Z_{i,j} = \frac{j\omega\mu_0}{2\pi} \ln \left(\frac{D'_{i,j}}{D_{i,j}} + J_m \right), \quad (2.25)$$

$$J_m^{Wise} = \int_0^\infty \frac{2\mu e^{-H\lambda}}{\mu_0 \left(\sqrt{\lambda^2 + j\frac{\omega\mu_0}{\rho} - \omega^2\mu_0\varepsilon_0\varepsilon_r + \omega^2\mu_0\varepsilon_0} \right) + \mu\lambda} \cos(\lambda D) d\lambda, \quad (2.26)$$

in which μ is the soil magnetic permeability, in [H/m].

Self-impedance ($Z_{i,i}$) is composed of an internal part ($Z_{i,i}^{int}$), which depends on the characteristics and geometry of the conductors, and an external part ($Z_{i,i}^{ext}$) that depends on the ground return path impedance, and are calculated as presented in (2.28)-(2.29):

$$Z_{i,i} = Z_{i,i}^{int} + Z_{i,i}^{ext}. \quad (2.27)$$

$$Z_{i,i}^{ext} = \frac{j\omega\mu_0}{2\pi} \ln \left(\frac{2|y_i|}{r_i} + J_s \right), \quad (2.28)$$

$$J_s^{Wise} = \int_0^\infty \frac{2\mu e^{-2|y_i|\lambda}}{\mu_0 \left(\sqrt{\lambda^2 + j\frac{\omega\mu_0}{\rho} - \omega^2\mu_0\varepsilon_0\varepsilon_r + \omega^2\mu_0\varepsilon_0} \right) + \mu\lambda} \cos(\lambda D) d\lambda. \quad (2.29)$$

These solutions, being considered more generalized formulations than Carson's integrals, serve as the reference solutions for the calculation of self and mutual impedances in this work.

2.3 TRANSMISSION LINE ADMITTANCE MATRIX

Considering a transmission line with N conductors, the capacitive coupling between the conductors is directly dependent on the amount of line charges:

$$\begin{bmatrix} V_1 \\ V_2 \\ V_3 \\ \vdots \\ V_N \end{bmatrix} = \begin{bmatrix} P_{1,1} & P_{1,2} & P_{1,3} & P_{1,k} & \dots & P_{1,N} \\ P_{2,1} & P_{2,2} & P_{2,3} & P_{2,k} & \dots & P_{2,N} \\ P_{3,1} & P_{3,2} & P_{3,3} & P_{3,k} & \dots & P_{3,N} \\ \vdots & \vdots & \vdots & \vdots & \ddots & \vdots \\ P_{N,1} & P_{N,2} & P_{N,3} & P_{N,k} & \dots & P_{N,N} \end{bmatrix} \cdot \begin{bmatrix} q_1 \\ q_2 \\ q_3 \\ \vdots \\ q_N \end{bmatrix} = \quad (2.30)$$

$$\mathbf{V} = \mathbf{P} \cdot \mathbf{q}, \quad (2.31)$$

in which q_N is the charge per unit length of the conductor N , expressed in [C/m], and \mathbf{P} is the Maxwell potential coefficients matrix, given in [m/F].

2.3.1 Potential Coefficients Over a Perfect Soil

The Maxwell potential coefficients can be calculated simply when the following assumptions are made: (1) the distance between conductors and/or conductors to soil are too long in comparison to the conductor radius, (2) the air as a perfectly insulating medium and (3) the soil is uniform at zero potential (DOMMEL; BHATTACHARYA, 1992). Then, considering these assumptions that are reasonable to the transmission line, the matrix \mathbf{P} elements can be computed using the method of images (DOMMEL; BHATTACHARYA, 1992).

Considering the system with two parallel conductors above a homogeneous soil, presented in Figure 2.2, the elements of Maxwell potential coefficients are determined according to the following expressions (DOMMEL; BHATTACHARYA, 1992):

$$P_{i,j} = \frac{1}{2\pi\epsilon_0\epsilon_r} \ln \left(\frac{D'_{i,j}}{D_{i,j}} \right), \quad (2.32)$$

in which, $P_{i,j}$ is the mutual potential coefficient between conductor i and j , expressed in [m/F]; ϵ_0 is the vacuum electric permittivity, given in [F/m]; ϵ_r is the soil relative electric permittivity; $D'_{i,j}$ is the distance between conductor i and the image of conductor j and $D_{i,j}$ is the distance between conductor i and j , both expressed in [m] (DOMMEL; BHATTACHARYA, 1992).

The self potentials coefficients $P_{i,i}$ are given by:

$$P_{i,i} = \frac{1}{2\pi\epsilon_0\epsilon_r} \ln \left(\frac{2|y_i|}{r_i} \right), \quad (2.33)$$

in which $|y_i|$ is the height of conductor i , in meters; and r_i is the conductor external radius, in meters. Then, the shunt admittance matrix \mathbf{Y} is determined as presented in (2.36).

While these solutions offer a reasonable approximation for transmission lines and effectively capture ground effects up to 1 MHz, it is worth noting that more refined models have been developed to account for soil characteristics better accurately (WG-36.02, 1995). These improved models take into consideration phenomena such as dispersion currents and the conductive properties of the ground on admittances computations (WISE, 1931; WISE, 1934; WISE, 1948).

2.3.2 Wise's Potential Coefficients Formulation For a Uniform Soil

Similar to impedance calculations, presented in Section 2.2.2, Wise introduced a solution for computing admittances that incorporates the effects of losses in imperfect soils (WISE, 1931; WISE, 1934; WISE, 1948). Thus, considering the two wires system shown in Figure 2.2, the potential coefficients can be determined using the following approach:

$$P_{i,j} = \frac{1}{2\pi\epsilon_0} \ln \left(\frac{D'_{i,j}}{D_{i,j}} + Q_m \right), \quad (2.34)$$

$$Q_m^{Wise} = \int_0^\infty \frac{-2\omega^2\mu\mu_0\epsilon_0(\mu_0\lambda + \alpha_g\mu)e^{-H\lambda}}{[\alpha_g\mu_0 + \lambda\mu] \left[\alpha_g\mu(\omega^2\mu_0\epsilon_0) + \lambda\mu_0 \left(\frac{j\omega\mu_0}{\rho} - \omega^2\mu_0\epsilon_r \right) \right]} \cos(\lambda D) d\lambda, \quad (2.35)$$

in which $\alpha_g = \sqrt{\lambda^2 + \left(\frac{j\omega\mu_0}{\rho} - \omega^2\mu_0\epsilon_r \right) + \omega^2\mu_0\epsilon_0}$; μ_0 is the magnetic permeability constant in free space, ϵ_0 is the vacuum electrical permittivity; ρ is the local soil electrical resistivity, in $[\Omega\text{m}]$; ϵ_r is the local soil relative electrical permittivity; μ is the soil magnetic permeability, in $[\text{H/m}]$; and H , D , $D_{i,j}$ and $D'_{i,j}$ are the relative distances represented in Figure 2.2, expressed in $[\text{m}]$.

The main elements of potential matrix $P_{i,i}$ can be obtained by setting $j = i$, $D_{i,i} = r_i$, $D'_{i,i} = 2|y_i|$ and $D = 0$, while Q_m is denoted as Q_s , in (2.34)-(2.35).

The formulation proposed by Wise for computing shunt admittances serves as the fundamental basis for the development of this work.

2.3.3 Shunt Admittance Matrix Calculation

With the computed matrix of potential coefficients \mathbf{P} , the shunt admittances \mathbf{Y} can be obtained using equation 2.36:

$$\mathbf{Y} = j\omega\mathbf{P}^{-1} \quad (2.36)$$

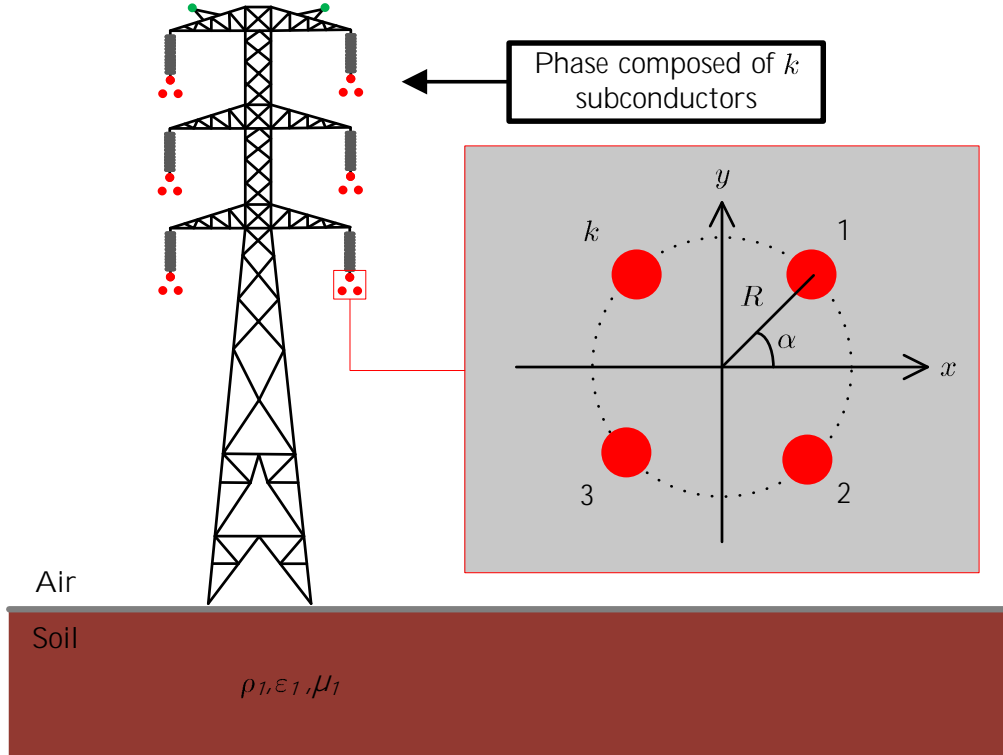
with $j = \sqrt{-1} = 1\angle 90^\circ$.

2.4 LINE PARAMETERS FOR EQUIVALENT PHASE CONDUCTORS

As a result of the skin effect, current tends to concentrate on the outer surface of a conductor. In theory, for extremely high voltages, it would be possible to use hollow conductors instead of solid tubular conductors. However, this approach is not economically viable, and therefore bundled conductors are employed (CHAVES; CHAGAS, 2016; WHEELER, 1942). By arranging multiple conductors in a specific geometric configuration to represent a single phase, as presented in Figure 2.3, various benefits are achieved, including the reduction of line reactance, corona losses, voltage gradients, radio interference, and the surge impedance of a power line (CHAVES; CHAGAS, 2016; WHEELER, 1942).

Then, the complete impedance matrix considering the individual parameters of each conductor, as presented in (2.2), can be large and contains redundant information. To overcome this, the common matrix used is the impedance matrix representing the equivalent impedances of each phase, condensing the amount of information and making the impedance matrix simpler.

Figure 2.3. Transmission line phase composed of k subconductors distributed symmetrically on a circumference with radius R .



Source: Own authorship.

2.4.1 Bundle Reduction

Considering a transmission line with k individual subconductors to be bundled to form a phase R , as presented in Figure 2.3, the follow condition is applied (DOMMEL; BHATTACHARYA, 1992):

$$I_1^R + I_2^R + \dots + I_k^R = I_R, \quad (2.37)$$

$$\frac{\partial V_1^R}{\partial x} = \frac{\partial V_2^R}{\partial x} = \dots = \frac{\partial V_k^R}{\partial x} = \frac{\partial V_R}{\partial x}, \quad (2.38)$$

Then, the relation in (2.2) can be rewritten as:

$$- \begin{bmatrix} \frac{\partial V_1^1}{\partial x} \\ \frac{\partial V_2^1}{\partial x} \\ \vdots \\ \frac{\partial V_k^1}{\partial x} \\ \vdots \\ \frac{\partial V_1^2}{\partial x} \\ \vdots \\ \frac{\partial V_k^R}{\partial x} \end{bmatrix} = \begin{bmatrix} Z_{1,1} & Z_{1,2} & Z_{1,3} & Z_{1,4} & \dots & Z_{1,k} \\ Z_{2,1} & Z_{2,2} & Z_{2,3} & Z_{2,4} & \dots & Z_{2,k} \\ \vdots & \vdots & \vdots & \vdots & \ddots & \vdots \\ Z_{3,1} & Z_{3,2} & Z_{3,3} & Z_{3,4} & \dots & Z_{3,k} \\ \vdots & \vdots & \vdots & \vdots & \ddots & \vdots \\ Z_{k,1} & Z_{k,2} & Z_{k,3} & Z_{k,4} & \dots & Z_{k,k} \end{bmatrix} \cdot \begin{bmatrix} I_1^1 \\ I_2^1 \\ \vdots \\ I_1^2 \\ \vdots \\ I_k^R \end{bmatrix}. \quad (2.39)$$

The first step is to introduce the phase current (I_R) in (2.39), by replacing the current of the first subconductor I_1^R by the total current I_R :

$$- \begin{bmatrix} \frac{\partial V_1^1}{\partial x} \\ \frac{\partial V_2^1}{\partial x} \\ \vdots \\ \frac{\partial V_k^R}{\partial x} \end{bmatrix} = \begin{bmatrix} Z_{1,1} & Z_{1,2} & \dots & Z_{1,k} \\ Z_{2,1} & Z_{2,2} & \dots & Z_{2,k} \\ \vdots & \vdots & \ddots & \vdots \\ Z_{k,1} & Z_{k,2} & \dots & Z_{k,k} \end{bmatrix} \cdot \begin{bmatrix} I_1^R \\ I_2^R \\ \vdots \\ I_k^R \end{bmatrix} \rightarrow - \begin{bmatrix} \frac{\partial V_1^1}{\partial x} \\ \frac{\partial V_2^1}{\partial x} \\ \vdots \\ \frac{\partial V_k^R}{\partial x} \end{bmatrix} = \begin{bmatrix} Z_{1,1} & Z_{1,2} & \dots & Z_{1,k} \\ Z_{2,1} & Z_{2,2} & \dots & Z_{2,k} \\ \vdots & \vdots & \ddots & \vdots \\ Z_{k,1} & Z_{k,2} & \dots & Z_{k,k} \end{bmatrix} \cdot \begin{bmatrix} I_R \\ I_2^R \\ \vdots \\ I_k^R \end{bmatrix}. \quad (2.40)$$

However, this procedure introduce errors proportional to $I_2^R + I_3^R + \dots + I_k^R$. To balance these errors it is necessary to perform a matrix operation which is to subtract the elements of the column of the first subconductor from the elements of all remaining ($k - 1$) columns (DOMMEL; BHATTACHARYA, 1992):

$$\mathbf{Z}_{k,k} = \mathbf{Z}_{k,k} - \mathbf{Z}_{k,1}. \quad (2.41)$$

Furthermore, a second matrix operation is required to eliminate the voltage terms in the remaining ($k - 1$) conductors. The process consists of subtracting the row of the first subconductor from the rows of the ($k - 1$) subconductors (DOMMEL; BHATTACHARYA, 1992):

$$-\begin{bmatrix} \frac{\partial V_1^1}{\partial x} \\ \frac{\partial V_2^1}{\partial x} - \frac{\partial V_1^R}{\partial x} \\ \vdots \\ \frac{\partial V_k^R}{\partial x} - \frac{\partial V_1^R}{\partial x} \end{bmatrix} = \begin{bmatrix} Z_{1,1} & Z_{1,2} & \cdots & Z_{1,k} \\ Z_{2,1} & Z_{2,2} & \cdots & Z_{2,k} \\ \vdots & \vdots & \ddots & \vdots \\ Z_{k,1} & Z_{k,2} & \cdots & Z_{k,k} \end{bmatrix} \cdot \begin{bmatrix} I_R \\ I_2^R \\ \vdots \\ I_k^R \end{bmatrix} \rightarrow -\begin{bmatrix} \frac{\partial V_1^1}{\partial x} \\ 0 \\ \vdots \\ 0 \end{bmatrix} = \begin{bmatrix} Z_{1,1} & Z_{1,2} & \cdots & Z_{1,k} \\ Z_{2,1} & Z_{2,2} & \cdots & Z_{2,k} \\ \vdots & \vdots & \ddots & \vdots \\ Z_{k,1} & Z_{k,2} & \cdots & Z_{k,k} \end{bmatrix} \cdot \begin{bmatrix} I_R \\ I_2^R \\ \vdots \\ I_k^R \end{bmatrix}, \quad (2.42)$$

$$\mathbf{Z}_{k,k} = \mathbf{Z}_{k,k} - \mathbf{Z}_{1,k}. \quad (2.43)$$

With the terms on the left side of (2.42) set to zero, the $(k - 1)$ subconductors can be eliminated by Kron reduction, explained in the next section, resulting in only one equivalent conductor for the bundled phase R .

A precaution to be taken when applying the Kron reduction in a multi-phase system composed of bundled conductors is that the $(k - 1)$ subconductors to be eliminated must be placed in the last columns and rows of the matrix before applying the Kron reduction.

2.4.2 Kron Reduction

Usually, the towers of transmission lines are grounded. This grounding involves the tower's metal structure and the shield wires of the transmission line. Therefore, considering a frequency of up to 250 kHz, it is reasonable that the potential of the grounded shield wires is considered equal to zero. This condition can be applied to any segmented grounded conductor and also to metallic structures that are grounded along the path (DOMMEL; BHATTACHARYA, 1992).

This condition allows us to apply a reduction in the equivalent phase impedance and admittance matrix, known as Kron reduction. The reduced matrix \mathbf{Z}_R is called the equivalent phase conductor matrix. Partitioning equation (2.2) with subscript " P " the phase conductors and with subscript " G " the grounded conductors, it follows that (DOMMEL; BHATTACHARYA, 1992):

$$-\begin{bmatrix} \frac{\partial \mathbf{V}_P}{\partial x} \\ \frac{\partial \mathbf{V}_G}{\partial x} \end{bmatrix} = \begin{bmatrix} \mathbf{Z}_{PP} & \mathbf{Z}_{PG} \\ \mathbf{Z}_{GP} & \mathbf{Z}_{GG} \end{bmatrix} \cdot \begin{bmatrix} \mathbf{I}_P \\ \mathbf{I}_G \end{bmatrix}. \quad (2.44)$$

Since $\mathbf{V}_{\mathbf{G}} = 0$ and $\frac{\partial \mathbf{V}_{\mathbf{G}}}{\partial x} = 0$, the impedance matrix can be reduced by eliminating $\mathbf{I}_{\mathbf{G}}$,

$$-\frac{\partial \mathbf{V}_{\mathbf{P}}}{\partial x} = \mathbf{Z}_{\mathbf{R}} \cdot \mathbf{I}_{\mathbf{P}} \quad (2.45)$$

in which

$$\mathbf{Z}_{\mathbf{R}} = \mathbf{Z}_{\mathbf{PP}} - \mathbf{Z}_{\mathbf{PG}} \cdot \mathbf{Z}_{\mathbf{GG}}^{-1} \cdot \mathbf{Z}_{\mathbf{GP}}. \quad (2.46)$$

In this manner, if the system is composed of M phases, the reduced matrix $\mathbf{Z}_{\mathbf{R}}$ will have dimensions $M \times M$, simplifying the analysis of the transmission system.

2.5 SYMMETRICAL COMPONENTS FOR IDEALLY TRANSPOSED THREE-PHASE TRANSMISSION LINES

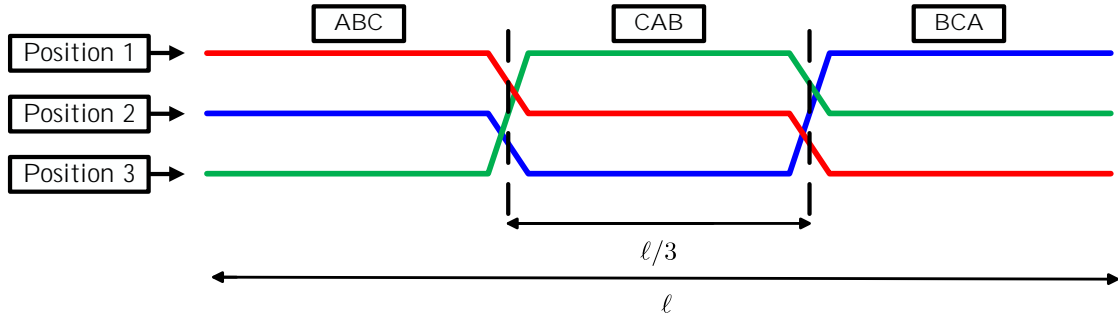
Analyzing electrical systems composed of transmission lines through their phase parameters is not the most common or simplest task to be done. Generally, transmission lines are analyzed using their sequence parameters. If the system is balanced, the coupled equations in the phase domain that describe the transmission system are transformed into decoupled equations in symmetrical components (DOMMEL; BHATTACHARYA, 1992; MONTEIRO, 2004).

A transmission line is considered balanced when, in the phase domain, the self-impedances (Z_s) and self-admittances (Y_s) are equal, and the mutual impedances (Z_m) and admittances (Y_m) between two conductors are equal,

$$\mathbf{Z}'_{\mathbf{ABC}} = \begin{bmatrix} Z_s & Z_m & \dots & Z_m \\ Z_m & Z_s & \dots & Z_m \\ \vdots & \vdots & \ddots & \vdots \\ Z_m & Z_m & \dots & Z_s \end{bmatrix}, \quad (2.47)$$

$$\mathbf{Y}'_{\mathbf{ABC}} = \begin{bmatrix} Y_s & Y_m & \dots & Y_m \\ Y_m & Y_s & \dots & Y_m \\ \vdots & \vdots & \ddots & \vdots \\ Y_m & Y_m & \dots & Y_s \end{bmatrix}. \quad (2.48)$$

A way to achieve a more balanced transmission line in real cases is by transposing the phase conductors, as illustrated in Figure 2.4.

Figure 2.4. Three-section transposition scheme for a three-phase single circuit transmission line.

Source: Own authorship.

Considering the total length of the transmission line (ℓ) and that each transposition section, commonly referred to as "barrels", are equally divided and has a length of one-third of the total length of the transmission line ($\ell/3$), the total impedance of the transposed transmission line can be calculated, with \mathbf{Z}'_{ABC} the equivalent phase matrix of the system after Kron reduction, as explained in detail in Section 2.4 (DOMMEL; BHATTACHARYA, 1992; MONTEIRO, 2004):

$$\mathbf{Z}'_{\text{ABC}} = \frac{1}{3} \cdot [\mathbf{Z}_{\text{ABC},1} + \mathbf{Z}_{\text{ABC},2} + \mathbf{Z}_{\text{ABC},3}] \quad (2.49)$$

$$\mathbf{Z}'_{\text{ABC}} = \frac{1}{3} \cdot \left\{ \begin{bmatrix} Z_{1,1} & Z_{1,2} & Z_{1,3} \\ Z_{2,1} & Z_{2,2} & Z_{2,3} \\ Z_{3,1} & Z_{3,2} & Z_{3,3} \end{bmatrix} + \begin{bmatrix} Z_{3,3} & Z_{3,1} & Z_{3,2} \\ Z_{3,1} & Z_{1,1} & Z_{2,3} \\ Z_{3,2} & Z_{1,2} & Z_{2,2} \end{bmatrix} + \begin{bmatrix} Z_{2,2} & Z_{2,3} & Z_{2,1} \\ Z_{3,2} & Z_{3,3} & Z_{3,1} \\ Z_{1,2} & Z_{1,3} & Z_{1,1} \end{bmatrix} \right\} = \quad (2.50)$$

$$\mathbf{Z}'_{\text{ABC}} = \begin{bmatrix} Z_s & Z_m & Z_m \\ Z_m & Z_s & Z_m \\ Z_m & Z_m & Z_s \end{bmatrix}, \quad (2.51)$$

in which,

$$Z_s = \frac{1}{3}(Z_{1,1} + Z_{2,2} + Z_{3,3}), \quad (2.52)$$

$$Z_m = \frac{1}{3}(Z_{1,2} + Z_{2,3} + Z_{3,1}). \quad (2.53)$$

Lastly, considering an ABC phase sequence, the Fortescue matrix \mathbf{S} is utilized to apply the symmetrical component transform, leading to the \mathbf{Z}_{012} sequence matrix:

$$\mathbf{S} = \begin{bmatrix} 1 & 1 & 1 \\ 1 & a^2 & a \\ 1 & a & a^2 \end{bmatrix}, \text{ with } a = e^{j120^\circ} \quad (2.54)$$

$$\mathbf{Z}_{012} = \mathbf{S}^{-1} \cdot \mathbf{Z}'_{\text{ABC}} \cdot \mathbf{S} = \begin{bmatrix} Z_0 & 0 & 0 \\ 0 & Z_1 & 0 \\ 0 & 0 & Z_2 \end{bmatrix}, \quad (2.55)$$

in which Z_0 and Z_1, Z_2 are, respectively, the zero, positive, and negative sequence impedances of the transmission line, in ohms per unit length. It is possible to deduce that Z_1 is equal to Z_2 , given the ideal transposition and perfect symmetry of the three-phase system considered (DOMMEL; BHATTACHARYA, 1992; MONTEIRO, 2004).

Due to transmission lines spanning long distances and encountering various terrains, soil types, vegetation, and numerous construction interferences, it is often not possible to achieve perfect one-third phase conductor transposition as proposed by ideal transpositions. Therefore, it is rare to find ideal transpositions in real transmission lines, which are presented in this section and the subsequent sections for understanding the methodology and its use in the specific literature.

The methodology to obtain the symmetrical components admittance matrix \mathbf{Y}_{012} precisely follows the steps outlined in (2.49)-(2.55), with subsequent calculation steps being omitted for brevity.

2.6 SYMMETRICAL COMPONENTS FOR IDEALLY TRANSPOSED DOUBLE-CIRCUIT TRANSMISSION LINES

Specific transposition schemes for double-circuit transmission lines transform the impedance and admittance phase matrices into decoupled diagonal matrix based on symmetrical components. The procedure for averaging the sections of the barrel remains consistent with the methodology described for a single three-phase circuit, outlined in (2.49)-(2.55). However, the phase domain matrix (\mathbf{Z}_{ABC}) in this case expands to dimensions of 6×6 due to the presence of two three-phase circuits at the same tower. Then, the symmetrical components of double-circuit lines are obtained from (DOMMEL; BHATTACHARYA, 1992; MONTEIRO, 2004):

$$\mathbf{Z}_{012} = \begin{bmatrix} \mathbf{S}^{-1} & 0 \\ 0 & \mathbf{S}^{-1} \end{bmatrix} \cdot \mathbf{Z}'_{\text{ABC}} \cdot \begin{bmatrix} \mathbf{S} & 0 \\ 0 & \mathbf{S} \end{bmatrix}, \quad (2.56)$$

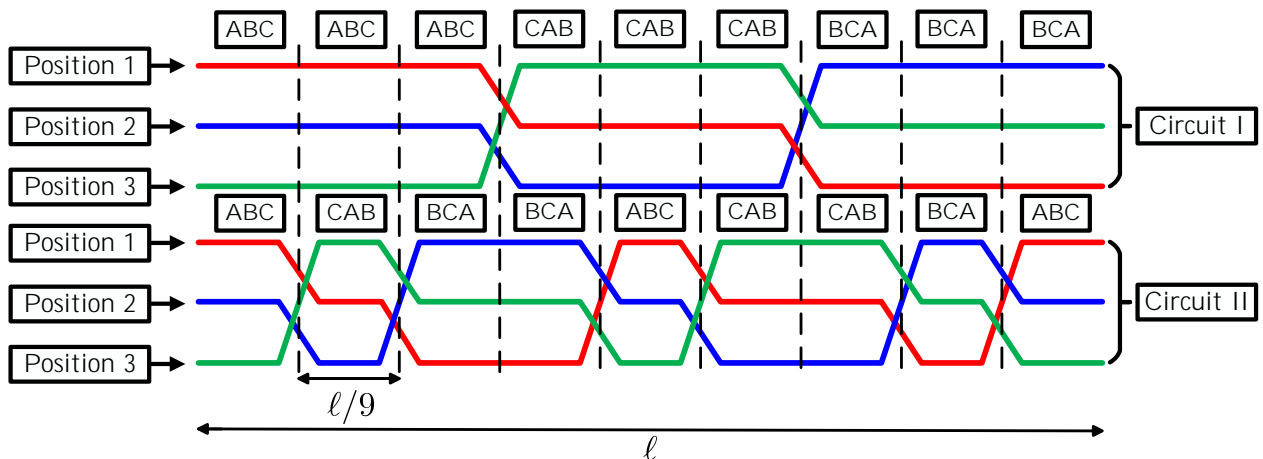
in which \mathbf{S} is the Fortescue matrix, defined in (2.54).

Since the two three-phase circuits belong to the same tower and are geometrically close to each other along the transmission line extension, electromagnetic and electrostatic couplings between the circuits will occur under steady-state and transient conditions (DOMMEL; BHATTACHARYA, 1992; MONTEIRO, 2004).

2.6.1 Nine-section Transposition Scheme for Double-circuit Transmission Lines

The nine-section transposition scheme for parallel circuit lines is a method used to minimize electromagnetic couplings between circuits in a double-circuit transmission line. In this scheme, each circuit is divided into nine sections, and the phases are transposed between these sections alternately (DOMMEL; BHATTACHARYA, 1992; MONTEIRO, 2004). The phase transposition for each circuit is performed in each barrel according to a specific pattern, as shown in Figure 2.5.

Figure 2.5. Nine-section transposition scheme for double-circuit transmission line.



Source: Own authorship.

It is important to note that although the transposition system is divided into nine sections, the first circuit exchanges the positions of the phases three times, while the second circuit does

it six times. Furthermore, both circuits rotate their phases in the same direction. In other words, when the phase positions are swapped, the conductor in position 1 moves to position 2, the conductor in position 2 moves to position 3, and the conductor in position 3 moves to position 1 in both circuits (DOMMEL; BHATTACHARYA, 1992; MONTEIRO, 2004).

Considering the transposition scheme presented in Figure 2.5, the average of the impedance matrix is:

$$\mathbf{Z}'_{\text{ABC}} = \frac{1}{9} \cdot [\mathbf{Z}_{\text{ABC},1} + \mathbf{Z}_{\text{ABC},2} + \mathbf{Z}_{\text{ABC},3} + \cdots + \mathbf{Z}_{\text{ABC},9}], \quad (2.57)$$

$$\mathbf{Z}'_{\text{ABC}} = \frac{1}{9} \cdot \begin{bmatrix} 3Z_s^{\text{I}} & 3Z_m^{\text{I}} & 3Z_m^{\text{I}} & Z_m^{\text{II-I}} & Z_m^{\text{II-I}} & Z_m^{\text{II-I}} \\ 3Z_m^{\text{I}} & 3Z_s^{\text{I}} & 3Z_m^{\text{I}} & Z_m^{\text{II-I}} & Z_m^{\text{II-I}} & Z_m^{\text{II-I}} \\ 3Z_m^{\text{I}} & 3Z_m^{\text{I}} & 3Z_s^{\text{I}} & Z_m^{\text{II-I}} & Z_m^{\text{II-I}} & Z_m^{\text{II-I}} \\ \hline Z_m^{\text{I-II}} & Z_m^{\text{I-II}} & Z_m^{\text{I-II}} & 3Z_s^{\text{II}} & 3Z_m^{\text{II}} & 3Z_m^{\text{II}} \\ Z_m^{\text{I-II}} & Z_m^{\text{I-II}} & Z_m^{\text{I-II}} & 3Z_m^{\text{II}} & 3Z_s^{\text{II}} & 3Z_m^{\text{II}} \\ Z_m^{\text{I-II}} & Z_m^{\text{I-II}} & Z_m^{\text{I-II}} & 3Z_m^{\text{II}} & 3Z_m^{\text{II}} & 3Z_s^{\text{II}} \end{bmatrix}, \quad (2.58)$$

in which, Z_s^{I} is the self-impedance from the first circuit, Z_s^{II} is the self-impedance from the second circuit, Z_m^{I} is the mutual impedance from the first circuit, Z_m^{II} is the mutual impedance from the second circuit, $Z_m^{\text{I-II}}$ is the mutual coupling impedance of circuit 1 onto circuit 2 and $Z_m^{\text{II-I}}$ is the mutual coupling impedance of circuit 2 onto circuit 1, in ohms per length unit and they are calculated as (MONTEIRO, 2004):

$$Z_s^{\text{I}} = Z_{1,1} + Z_{2,2} + Z_{3,3}, \quad (2.59)$$

$$Z_s^{\text{II}} = Z_{4,4} + Z_{5,5} + Z_{6,6}, \quad (2.60)$$

$$Z_m^{\text{I}} = Z_{1,2} + Z_{2,3} + Z_{3,1}, \quad (2.61)$$

$$Z_m^{\text{II}} = Z_{4,5} + Z_{5,6} + Z_{6,4}, \quad (2.62)$$

considering that the average separation between the circuits remains the same along the entire path extension of the transmission line, the mutual impedance coupling between both circuits is the same and is calculated as (MONTEIRO, 2004):

$$Z_m^{I-II} = Z_m^{II-I} = Z_{1,4} + Z_{1,5} + Z_{1,6} + Z_{2,4} + Z_{2,5} + Z_{2,6} + Z_{3,4} + Z_{3,5} + Z_{3,6}. \quad (2.63)$$

By transforming \mathbf{Z}'_{ABC} into symmetrical components using transformation in (2.56), the sequence matrix \mathbf{Z}_{012} for a nine-section transposed double-circuit transmission line is obtained:

$$\mathbf{Z}_{012} = \left[\begin{array}{ccc|ccc} Z_0^I & 0 & 0 & Z_0^{II-I} & 0 & 0 \\ 0 & Z_1^I & 0 & 0 & 0 & 0 \\ 0 & 0 & Z_2^I & 0 & 0 & 0 \\ \hline Z_0^{I-II} & 0 & 0 & Z_0^{II} & 0 & 0 \\ 0 & 0 & 0 & 0 & Z_1^{II} & 0 \\ 0 & 0 & 0 & 0 & 0 & Z_2^{II} \end{array} \right]. \quad (2.64)$$

Considering two perfectly transposed and parallel three-phase circuits with identical circuit constructive aspects, meaning both circuits have the same geometric spacing between phases, are symmetrical to the tower axis, and consist of the same phase conductors and shield wires constructive parameters, then using a special case of the transformation matrix for any number of phases on balanced transmission lines ($\mathbf{T}_{M\text{-phases}}$), it is possible to obtain a decoupled diagonal matrix based on symmetrical components of the transmission line, as follows (DOMMEL; BHATTACHARYA, 1992; FEDOROV *et al.*, 2022):

$$\mathbf{Z}'_{012} = \mathbf{T}_{6\text{-phases}}^{-1} \cdot \mathbf{Z}'_{ABC} \cdot \mathbf{T}_{6\text{-phases}}, \quad (2.65)$$

in which $\mathbf{T}_{6\text{-phases}}$ is a six-phases transformation matrix derived from a generalized transformation matrix for M-phases ($\mathbf{T}_{M\text{-phases}}$) balanced transmission lines, given by (DOMMEL; BHATTACHARYA, 1992):

$$\mathbf{T}_{6\text{-phases}} = \left[\begin{array}{cccccc} 1 & 1 & \sqrt{3} & 1 & 0 & 0 \\ 1 & 1 & -\sqrt{3} & 1 & 0 & 0 \\ 1 & 1 & 0 & -2 & 0 & 0 \\ 1 & -1 & 0 & 0 & \sqrt{3} & 1 \\ 1 & -1 & 0 & 0 & -\sqrt{3} & 1 \\ 1 & -1 & 0 & 0 & 0 & -2 \end{array} \right]. \quad (2.66)$$

Then, equation (2.65) yields a diagonal matrix, given by: \mathbf{Z}'_{012}

$$\mathbf{Z}'_{012} = \begin{bmatrix} Z_0 & 0 & 0 & 0 & 0 & 0 \\ 0 & Z_0^{I-II} & 0 & 0 & 0 & 0 \\ 0 & 0 & Z_1^I & 0 & 0 & 0 \\ 0 & 0 & 0 & Z_2^I & 0 & 0 \\ 0 & 0 & 0 & 0 & Z_1^{II} & 0 \\ 0 & 0 & 0 & 0 & 0 & Z_2^{II} \end{bmatrix}, \quad (2.67)$$

in which Z_0 is the zero sequence impedance, Z_0^{I-II} is the zero sequence coupling impedance between the circuits, Z_1^I is the positive sequence impedance for the first circuit, Z_2^I is the negative sequence impedance for the first circuit, Z_1^{II} is the positive sequence impedance for the second circuit, Z_2^{II} is the negative sequence impedance for the second circuit, all given in $[\Omega/\text{m}]$.

Since the two circuits are identical and symmetric: $Z_1^I = Z_2^I = Z_1^{II} = Z_2^{II}$, then the matrix (2.67) can be rewritten as:

$$\mathbf{Z}'_{012} = \begin{bmatrix} Z_0 & 0 & 0 & 0 & 0 & 0 \\ 0 & Z_0^{I-II} & 0 & 0 & 0 & 0 \\ 0 & 0 & Z_1 & 0 & 0 & 0 \\ 0 & 0 & 0 & Z_1 & 0 & 0 \\ 0 & 0 & 0 & 0 & Z_1 & 0 \\ 0 & 0 & 0 & 0 & 0 & Z_1 \end{bmatrix}. \quad (2.68)$$

Despite the matrix (2.67) being diagonal, the modal transformation using the matrix $\mathbf{T}_{6\text{-phases}}$ does not imply a modal system with six decoupled modes. Consequently, the system still depend on the zero sequence coupling between the circuits. Hence, this coupling between the circuits still exists, even though it may appear to be implicated.

Balancing three-phase double-circuit lines just through transposition never result in a completely diagonal symmetrical matrix, which means there will always be some form of zero, positive, or negative sequence coupling between the two circuits (DOMMEL; BHATTACHARYA, 1992). The method that produces the minimal coupling between the circuits is the nine-section transposition, which results in only a zero sequence coupling factor between both circuits on the same tower.

Similarly to the single three-phase system, all the developments presented for impedance involving the transposition of double-circuit transmission lines are applicable to admittances as well. For the sake of brevity, they are omitted in this section.

2.6.2 Three-section Transposition Scheme for Double-circuit Transmission Lines

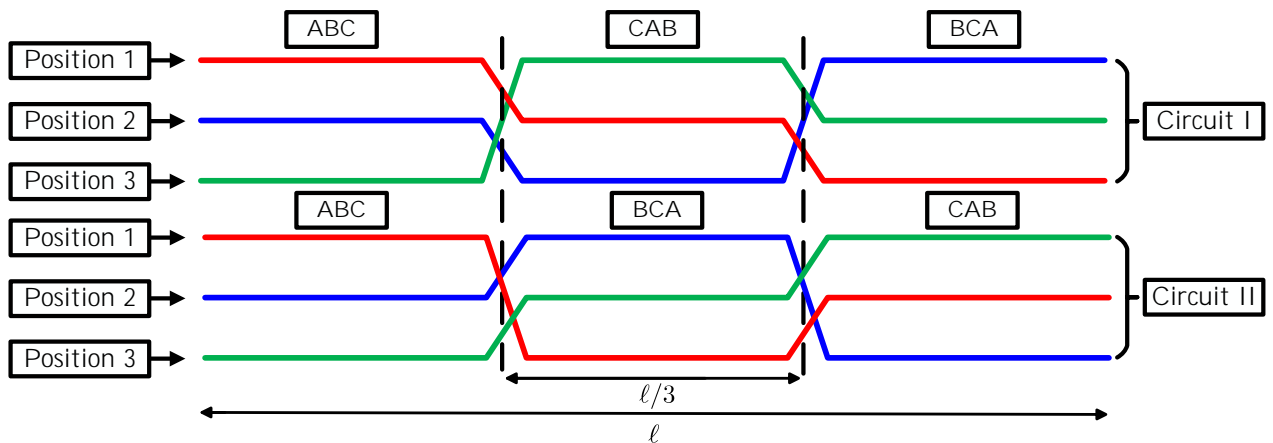
The three transposition barrels schemes include positive, negative, and zero sequences coupling between the circuits. However, this transposition scheme offers the advantage of lower cost and execution complexity in comparison to the nine-section barrels system. Since only four towers are required for the transpositions, as opposed to the eight towers needed in the latter (MONTEIRO, 2004; DOMMEL; BHATTACHARYA, 1992).

The three-section transposition scheme is widely used for double-circuit transmission lines due to its advantages. Two main types of this transposition scheme are observed: with barrels rolled in the opposite direction and with barrels rolled in the same direction.

2.6.2.1 Barrels Rolled in Opposite Direction

In this transposition scheme, both circuits are divided into three equal segments, and during each transposition, the rotation of phases in the second circuit is performed in the opposite direction to the first circuit. This arrangement is illustrated in Figure 2.6.

Figure 2.6. Three-section transposition scheme with barrels rolled in opposite direction for a double-circuit transmission line.



Source: Own authorship.

The total impedance for this system is determined by the following calculation (MONTEIRO, 2004):

$$\mathbf{Z}'_{\text{ABC}} = \frac{1}{3} \cdot \left[\begin{array}{ccc|ccc} Z_s^{\text{I}} & Z_m^{\text{I}} & Z_m^{\text{I}} & Z_s^{\text{II-I}} & Z_m^{\text{II-I}} & Z_l^{\text{II-I}} \\ Z_m^{\text{I}} & Z_s^{\text{I}} & Z_m^{\text{I}} & Z_l^{\text{II-I}} & Z_s^{\text{II-I}} & Z_m^{\text{II-I}} \\ Z_m^{\text{I}} & Z_m^{\text{I}} & Z_s^{\text{I}} & Z_m^{\text{II-I}} & Z_l^{\text{II-I}} & Z_s^{\text{II-I}} \\ \hline Z_s^{\text{I-II}} & Z_m^{\text{I-II}} & Z_l^{\text{I-II}} & Z_s^{\text{II}} & Z_m^{\text{II}} & Z_m^{\text{II}} \\ Z_l^{\text{I-II}} & Z_s^{\text{I-II}} & Z_m^{\text{I-II}} & Z_m^{\text{II}} & Z_s^{\text{II}} & Z_m^{\text{II}} \\ Z_m^{\text{I-II}} & Z_l^{\text{I-II}} & Z_s^{\text{I-II}} & Z_m^{\text{II}} & Z_m^{\text{II}} & Z_s^{\text{II}} \end{array} \right], \quad (2.69)$$

in which \mathbf{Z}'_{ABC} elements, expressed in $[\Omega/\text{m}]$, and calculated as:

$$Z_s^{\text{I}} = Z_{1,1} + Z_{2,2} + Z_{3,3}, \quad (2.70)$$

$$Z_s^{\text{II}} = Z_{4,4} + Z_{5,5} + Z_{6,6}, \quad (2.71)$$

$$Z_m^{\text{I}} = Z_{1,2} + Z_{2,3} + Z_{3,1}, \quad (2.72)$$

$$Z_m^{\text{II}} = Z_{4,5} + Z_{5,6} + Z_{6,4}, \quad (2.73)$$

and

$$Z_s^{\text{I-II}} = Z_s^{\text{II-I}} = Z_{1,4} + Z_{2,5} + Z_{3,6}, \quad (2.74)$$

$$Z_m^{\text{I-II}} = Z_m^{\text{II-I}} = Z_{1,5} + Z_{2,6} + Z_{3,4}, \quad (2.75)$$

$$Z_l^{\text{I-II}} = Z_l^{\text{II-I}} = Z_{1,6} + Z_{2,4} + Z_{3,5}. \quad (2.76)$$

Finally, applying the transformation (2.56):

$$\mathbf{Z}_{012} = \left[\begin{array}{ccc|ccc} Z_0^{\text{I}} & 0 & 0 & Z_0^{\text{II-I}} & 0 & 0 \\ 0 & Z_1^{\text{I}} & 0 & 0 & Z_1^{\text{II-I}} & 0 \\ 0 & 0 & Z_2^{\text{I}} & 0 & 0 & Z_2^{\text{II-I}} \\ \hline Z_0^{\text{I-II}} & 0 & 0 & Z_0^{\text{II}} & 0 & 0 \\ 0 & Z_1^{\text{I-II}} & 0 & 0 & Z_1^{\text{II}} & 0 \\ 0 & 0 & Z_2^{\text{I-II}} & 0 & 0 & Z_2^{\text{II}} \end{array} \right]. \quad (2.77)$$

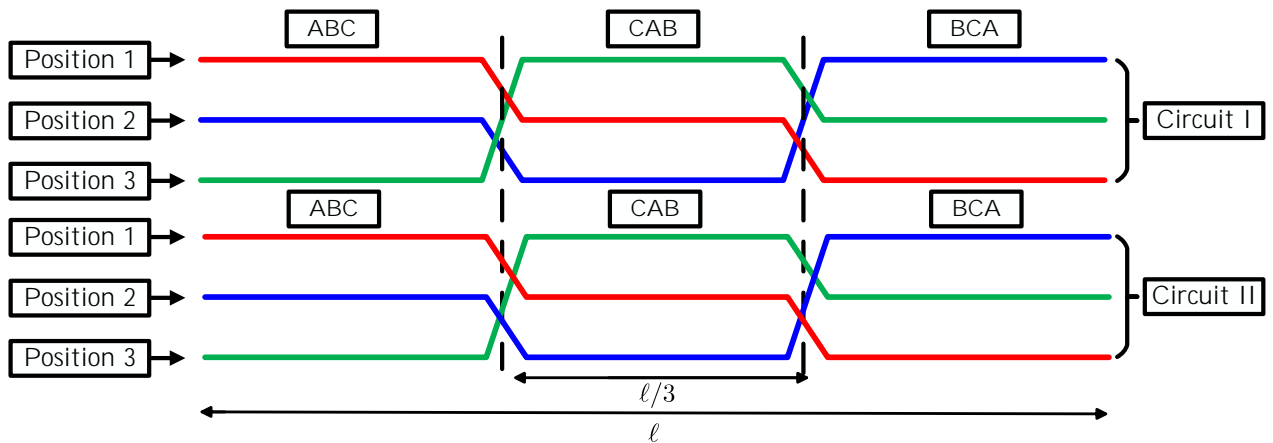
Employing the three-section transposition scheme with barrels rolled in opposite directions introduces electromagnetic coupling on positive and negative sequences between the circuits. In other words, the positive sequence of the first circuit is electromagnetically coupled with the

positive sequence of the second circuit. Consequently, a positive sequence current in Circuit 1 causes a voltage drop in the positive sequence of Circuit 2, while the negative and zero sequences are not impacted. A similar coupling phenomenon between the circuits at the same tower occurs in the negative sequence (MONTEIRO, 2004).

2.6.2.2 Barrels Rolled in Same Direction

A different coupling phenomenon occurs with the positions of the phase rotating in the same directions between circuits. In this transposition scheme, presented in Figure 2.7, a positive sequence current in a circuit induces a voltage drop in the negative sequence of the other circuit. Likewise, a negative sequence current in a circuit causes a voltage drop on the positive sequence of the second circuit, due to the electromagnetic coupling between the circuits using the three-section transposition with the barrels rolled in the same direction (MONTEIRO, 2004).

Figure 2.7. Three-section transposition scheme with barrels rolled in same direction for double-circuit transmission line.



Source: Own authorship.

Similar to the other transposition schemes, the total impedance of the transmission line is determined by averaging the sections. Subsequently, the transformation (2.56) is applied, resulting in the symmetrical components matrix \mathbf{Z}_{012} , shown in (2.86):

$$\mathbf{Z}'_{\text{ABC}} = \frac{1}{3} \cdot \left[\begin{array}{ccc|ccc} Z_s^{\text{I}} & Z_m^{\text{I}} & Z_m^{\text{I}} & Z_k^{\text{II-I}} & Z_l^{\text{II-I}} & Z_m^{\text{II-I}} \\ Z_m^{\text{I}} & Z_s^{\text{I}} & Z_m^{\text{I}} & Z_l^{\text{II-I}} & Z_m^{\text{II-I}} & Z_k^{\text{II-I}} \\ Z_m^{\text{I}} & Z_m^{\text{I}} & Z_s^{\text{I}} & Z_m^{\text{II-I}} & Z_k^{\text{II-I}} & Z_l^{\text{II-I}} \\ \hline Z_k^{\text{I-II}} & Z_l^{\text{I-II}} & Z_m^{\text{I-II}} & Z_s^{\text{II}} & Z_m^{\text{II}} & Z_m^{\text{II}} \\ Z_l^{\text{I-II}} & Z_m^{\text{I-II}} & Z_k^{\text{I-II}} & Z_m^{\text{II}} & Z_s^{\text{II}} & Z_m^{\text{II}} \\ Z_m^{\text{I-II}} & Z_k^{\text{I-II}} & Z_l^{\text{I-II}} & Z_m^{\text{II}} & Z_m^{\text{II}} & Z_s^{\text{II}} \end{array} \right], \quad (2.78)$$

in which \mathbf{Z}'_{ABC} elements, given in $[\Omega/\text{m}]$, and calculated as:

$$Z_s^{\text{I}} = Z_{1,1} + Z_{2,2} + Z_{3,3}, \quad (2.79)$$

$$Z_s^{\text{II}} = Z_{4,4} + Z_{5,5} + Z_{6,6}, \quad (2.80)$$

$$Z_m^{\text{I}} = Z_{1,2} + Z_{2,3} + Z_{3,1}, \quad (2.81)$$

$$Z_m^{\text{II}} = Z_{4,5} + Z_{5,6} + Z_{6,4}, \quad (2.82)$$

and

$$Z_k^{\text{I-II}} = Z_k^{\text{II-I}} = Z_{1,4} + Z_{3,5} + Z_{2,6}, \quad (2.83)$$

$$Z_l^{\text{I-II}} = Z_l^{\text{II-I}} = Z_{1,5} + Z_{3,6} + Z_{2,4}, \quad (2.84)$$

$$Z_m^{\text{I-II}} = Z_m^{\text{II-I}} = Z_{1,6} + Z_{3,4} + Z_{2,5}, \quad (2.85)$$

$$\mathbf{Z}_{012} = \left[\begin{array}{ccc|ccc} Z_0^{\text{I}} & 0 & 0 & Z_0^{\text{II-I}} & 0 & 0 \\ 0 & Z_1^{\text{I}} & 0 & 0 & 0 & Z_2^{\text{II-I}} \\ 0 & 0 & Z_2^{\text{I}} & 0 & Z_1^{\text{II-I}} & 0 \\ \hline Z_0^{\text{I-II}} & 0 & 0 & Z_0^{\text{II}} & 0 & 0 \\ 0 & 0 & Z_2^{\text{I-II}} & 0 & Z_1^{\text{II}} & 0 \\ 0 & Z_1^{\text{I-II}} & 0 & 0 & 0 & Z_2^{\text{II}} \end{array} \right]. \quad (2.86)$$

2.7 MODAL PARAMETERS FOR UNTRANSPOSED LINES

The symmetrical components approach offers a practical means of dealing with multi-phase systems, however, this method yields average values for characteristics impedances and pro-

propagation constants, which may conceal significant effects arising from conductor asymmetry (WEDEPOHL, 1963; WEDEPOHL *et al.*, 1996). The modal-domain representation overcomes this problem by transforming N coupled line conductors' phase parameters \mathbf{Z} and \mathbf{Y} into their respective N decoupled propagation modes.

Using eigenvalue/eigenvector theory, the coupled matrices \mathbf{Z} and \mathbf{Y} , whose terms are given according to (2.25)-(2.29) and (2.34)-(2.35) respectively, can be cast into decoupled diagonal ones (WEDEPOHL, 1963; WEDEPOHL *et al.*, 1996):

$$\mathbf{\Lambda} = \mathbf{T}_{\mathbf{V}}^{-1} \cdot \mathbf{Y} \cdot \mathbf{Z} \cdot \mathbf{T}_{\mathbf{V}}, \quad (2.87)$$

in which $\mathbf{\Lambda}$ is the diagonal matrix composed of the eigenvalues of the matrix product $\mathbf{Y} \cdot \mathbf{Z}$, and $\mathbf{T}_{\mathbf{V}}$ is the matrix of eigenvectors, or modal transformation matrix, associated with $\mathbf{Y} \cdot \mathbf{Z}$.

Matrices $\mathbf{\Lambda}$ and $\mathbf{T}_{\mathbf{V}}$ are determined by solving the following system of linear equations (WEDEPOHL, 1963; WEDEPOHL *et al.*, 1996):

$$\{\mathbf{Y} \cdot \mathbf{Z} - \Lambda_k \mathbf{I}\} \cdot \mathbf{T}_{\mathbf{V},k} = 0, \quad (2.88)$$

in which \mathbf{I} is the identity matrix, Λ_k is the k -th eigenvalue of matrix product $\mathbf{Y} \cdot \mathbf{Z}$, and $\mathbf{T}_{\mathbf{V},k}$ denotes the k -th column of modal matrix $\mathbf{T}_{\mathbf{V}}$.

It is worth noting that the transformation matrix $\mathbf{T}_{\mathbf{V}}$ in the modal domain is not constant or predetermined, unlike in the symmetrical domain. Additionally, the transformation matrix is frequency-dependent (FD), meaning that it varies according to the operating frequency of the system and transients phenomenon (CHRYSOCHOS *et al.*, 2014).

Equation (2.88) contains information about the propagation parameters of the transmission line, as the eigenvalues resulting from the solution of the linear system correspond to the propagation constants derived from the transmission line wave equation. It is worth noting that for the same set of eigenvalues of the product $\mathbf{Y} \cdot \mathbf{Z}$, which represents the physics of wave propagation along the line, there are infinite possible sets of eigenvectors that satisfy the (2.88) relation. It can be demonstrated that the Fortescue (2.54) and Clarke (2.66) matrices are composed of eigenvectors that characterize particular solutions of (2.88), which are valid for low frequencies. In other words, these transformation matrices, commonly employed in power

system analysis and short-circuit studies, are also forms of modal decompositions.

A crucial aspect for the precise implementation of modal-domain models is the derivation of frequency-dependent transformation matrices that exhibit smooth behavior across the frequency range (CHRYSOCHOS *et al.*, 2014). This entails ensuring that the matrices do not contain any discontinuity or swaps between the elements in the frequency domain. An attempt to compute the eigenvectors using conventional algorithms like the QR method leads to undesirable frequency-domain "switchovers" (FRANCIS, 1961; FRANCIS, 1962; CHRYSOCHOS *et al.*, 2014; FERNANDES; NEVES, 2004).

In this study, the linear system (2.88) is solved using the Levenberg-Marquardt algorithm, which is combined with an eigenvector correlation technique (CHRYSOCHOS *et al.*, 2014; LEVENBERG, 1944; MARQUARDT, 1963).

Modal parameters are the diagonal elements of modal matrices \mathbf{Z}_M and \mathbf{Y}_M calculated as follows:

$$\mathbf{Z}_M = \mathbf{T}_V^T \cdot \mathbf{Z} \cdot \mathbf{T}_V, \quad (2.89)$$

$$\mathbf{Y}_M = \mathbf{T}_V^{-1} \cdot \mathbf{Y} \cdot \mathbf{T}_V^{-T}, \quad (2.90)$$

in which superscript $^{-T}$ denotes the inverse of the transposed matrix.

The k -th propagation parameters on modal-domain are calculated using \mathbf{Z}_M and \mathbf{Y}_M in (2.2) and (2.3).

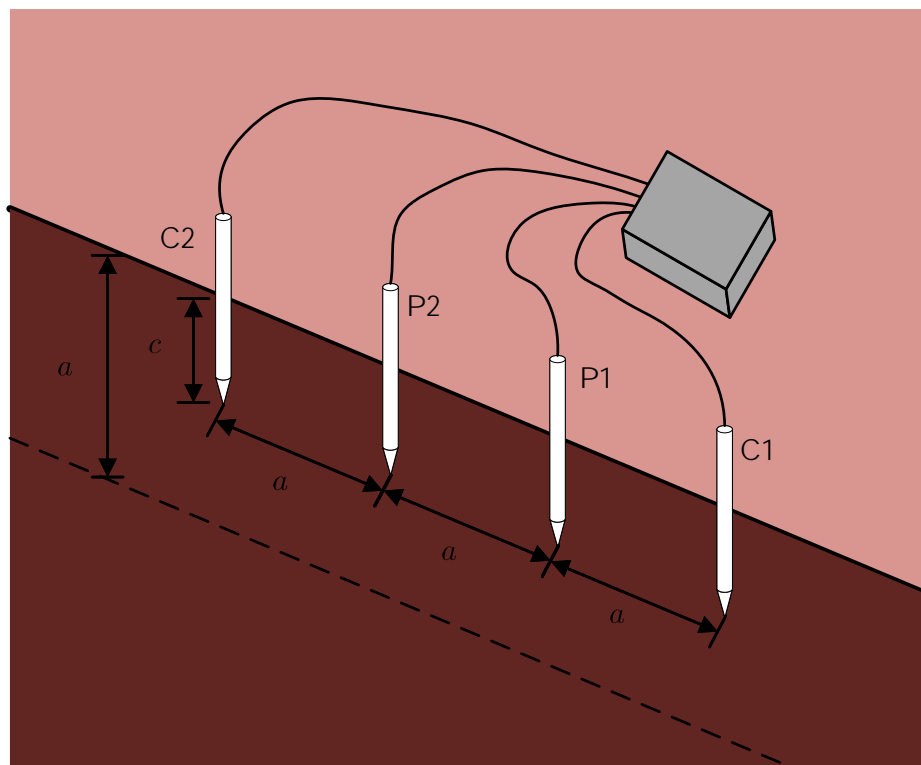
2.8 SOIL MODELING

Electromagnetic transients in power transmission systems require accurate calculations of earth-return parameters. The electromagnetic properties of the soil are of utmost importance in accurately capturing the effects of surges in transmission lines. Thus, a thorough analysis and proper representation of the soil in electrical system modeling are critical (WG-36.02, 1995; PAPADOPOULOS *et al.*, 2021; XUE *et al.*, 2018).

2.8.1 Wenner Method

Figure 2.8 depicts the Wenner method employed for the measurement of soil apparent resistivity. The method involves the arrangement of four electrodes (C1, C2, P1, and P2) in a collinear fashion with equal spacing a between them. These electrodes are inserted into the soil at a depth of c meters. A known test current I_W^a is injected from terminal C1 to terminal C2, resulting in a voltage drop V_W^a measured between the voltage probes P1 and P2. The apparent soil resistance R_{app}^a is then calculated using the following equation (WENNER, 1915; SAZALI *et al.*, 2020):

Figure 2.8. Diagram of Wenner method for measurement of soil apparent resistivity. The probes C1, C2, P1, and P2 are inserted at c meters depth and are positioned spaced by a meters. The electrode spacing a is numerically equal to the soil reading.



Source: Own authorship.

$$R_{app}^a = \frac{V_W^a}{I_W^a}, \quad (2.91)$$

in which R_{app}^a is the apparent resistance that corresponds to the soil equivalent resistance in the

electrical path at depth a , given in ohms. The apparent soil resistivity ρ_{app}^a at depth a meters can be determined from R_{app}^a as following

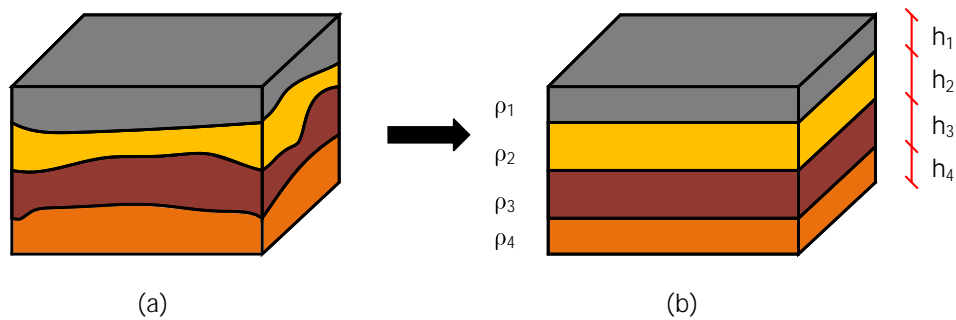
$$\rho_{app}^a = \frac{4\pi a R_{app}^a}{1 + \frac{2a}{\sqrt{a^2+4c^2}} - \frac{a}{\sqrt{a^2+c^2}}}, \quad (2.92)$$

in which ρ_{app}^a is the measured apparent resistivity at depth a , in Ωm ; a is the electrode spacing, in meters; and c is the electrode insertion depth, in meters.

2.8.2 Multilayered Soil Models

Extraction of information from apparent resistivity data is frequently the most challenging stage in soil modeling. The aim is to identify a set of parameters that effectively depict the true soil composition. Typically, it is reasonable to approximate the earth as a horizontally stratified multilayer structure since resistivity variations tend to exhibit greater changes with depth rather than with longitudinal distance (IEEE Std 80, 2000; ZHANG *et al.*, 2005). This procedure is illustrated in Figure 2.9.

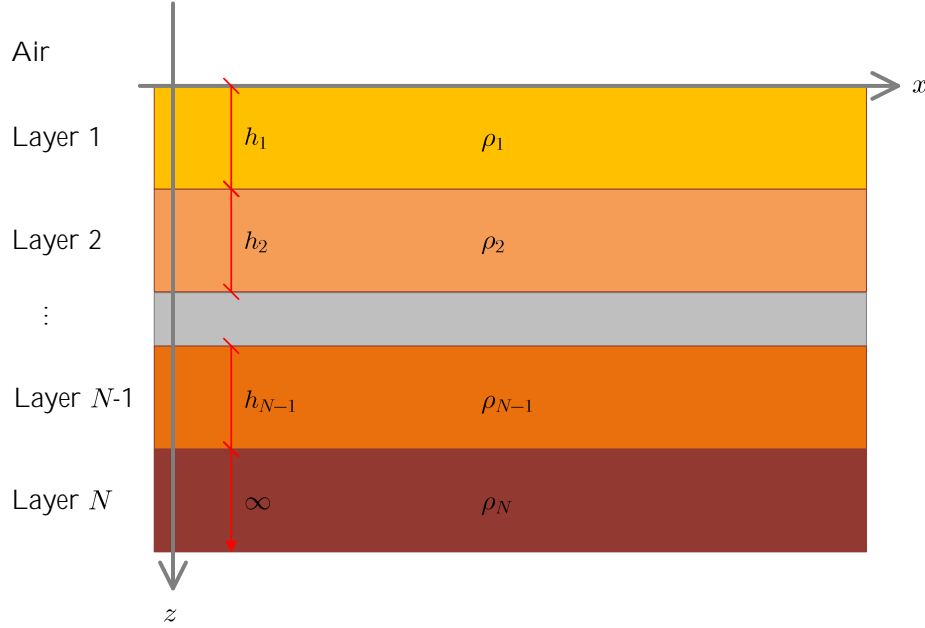
Figure 2.9. Real soil (a); and horizontally layered model described by parameters $[\rho_1; \rho_2; \rho_3; \rho_4]$ and $[h_1; h_2; h_3; h_4]$ (b).



Source: adapted from (ABNT, 2012).

Generally, a multilayered soil consist of $(N-1)$ layers with distincts resistivities $[\rho_1, \rho_2, \dots, \rho_{N-1}]$ and thicknesses $[h_1, h_2, \dots, h_{N-1}]$, atop an N^{th} layer known as the deep layer, as presented in Figure 2.10. The deep layer is represented for a resistivity ρ_N with an infinite thickness $h_N \rightarrow \infty$.

The case $N = 1$ corresponds to a homogeneous or uniform soil model, in which the electrical

Figure 2.10. N -layered horizontal soil model.

Source: Own authorship.

resistivity is determined as the arithmetic mean of the measured apparent resistivities (IEEE Std 80, 2000). The uniform model is a theoretical value and is useful for simplified estimations, but is encountered in few practical cases as real soil structures found in nature are reported to be composed of three to five layers (WHELAN J.M; HANRATTY, 2010).

For an N -layered soil model, the analytical expression for the apparent resistivity is (TAKAHASHI; KAWASE, 1990; ZHANG *et al.*, 2005):

$$\rho_a = \rho_1 [1 + 2F_N(a) - F_N(2a)], \quad (2.93)$$

$$F_N(x) = 2x \int_0^\infty \frac{K_{N,1} e^{-2\lambda h_1}}{1 - K_{N,1} e^{-2\lambda h_1}} \widehat{J}_0(\lambda x) d\lambda, \quad (2.94)$$

in which \widehat{J}_0 is the Bessel function of the first kind and order zero; λ is an auxiliary integration variable that represents the spatial frequency of the Fourier spectrum and can be physically associated to the energy attenuation throughout the layers (TSIAMITROS *et al.*, 2007); and $K_{N,1}$ is the soil structure kernel function, defined recursively as:

$$K_{N,s} = \frac{k_s + K_{N,s+1} e^{-2\lambda h_{s+1}}}{1 + k_s K_{N,s+1} e^{-2\lambda h_{s+1}}}, \quad (2.95)$$

$$K_{N,N-1} = k_{N-1}, \quad (2.96)$$

$$k_S = \frac{\rho_{S+1} - \rho_S}{\rho_{S+1} + \rho_S}, \quad (2.97)$$

$$k_{N-1} = \frac{\rho_N - \rho_{N-1}}{\rho_N + \rho_{N-1}}, \quad (2.98)$$

in which k_S is known as the reflection coefficient between layers S and $S + 1$, ranging between values -1 and $+1$. The improper integral in (2.94) is quickly decayed to zero, allowing the upper limit to be truncated to a convenient choice. Normally, accurate results can be achieved by integrating within the interval $[0, \frac{4}{h_1}]$ (HE *et al.*, 2012).

The process of soil parameter inversion involves the identification of $[\rho_1, \rho_2, \rho_3, \dots, \rho_N]$ and $[h_1, h_2, h_3, \dots, h_{N-1}]$ based on the measured values of $\rho_{app}^a \times a$. Given that the theoretical value of ρ_a can be determined using (2.92)-(2.98), it is possible to establish the following error function:

$$\Psi_e(\rho_1, \rho_2, \dots, \rho_N, h_1, h_2, \dots, h_{N-1}) = \sum_{j=1}^M \left[\frac{\rho_{a,j}^m - \rho_{a,j}}{\rho_{a,j}^m} \right]^2, \quad (2.99)$$

in which Ψ_e is the stratification normalized quadratic error; and M is the number of apparent resistivity measurements. The estimation of soil parameters involves the selection of an initial approximation and the application of a suitable minimization method utilizing (2.99) as the objective function, which has a distinct and differentiable structure. To achieve this, various approaches, including steepest descent, Levenberg-Marquardt, and evolutionary algorithms, have been found to yield satisfactory outcomes (ALAMO, 1993; MARTINS-BRITTO, 2017; DAWALIBI; BLATTNER, 1984).

2.8.3 Frequency-dependent Soil Properties

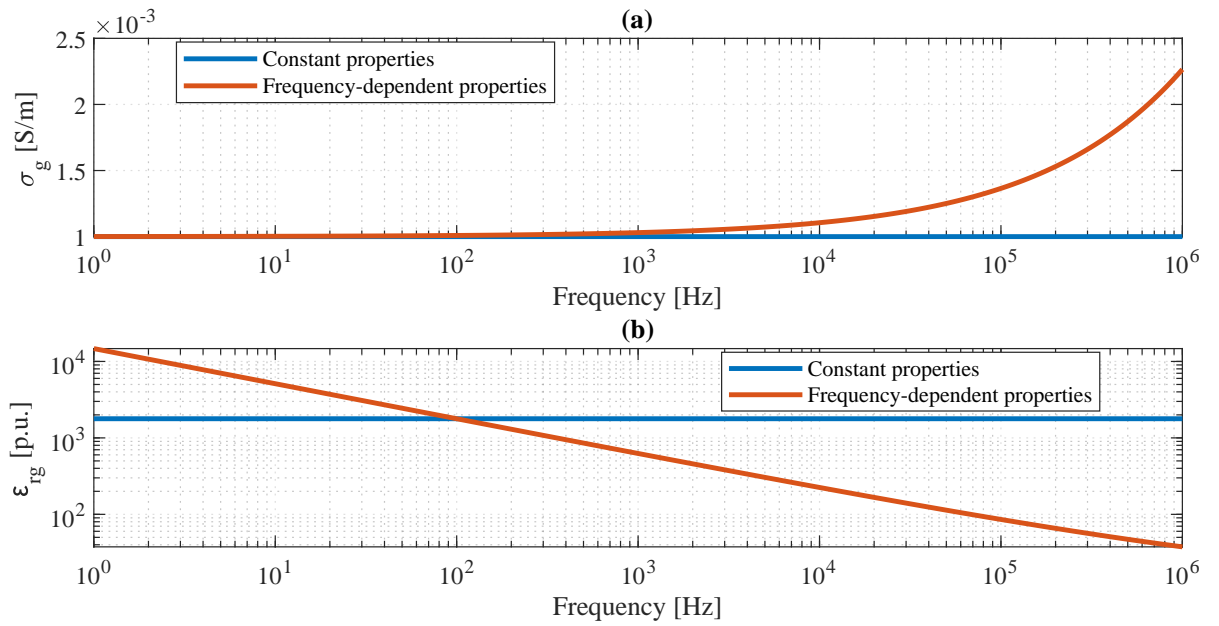
The relative permittivity (ε_{rg}) and conductivity (σ_g) reflect the dispersive and lossy nature of the soil as a dielectric material, taking into account dynamic polarization processes (PAPADOPOULOS; PAPAGIANNIS, 2007; SEMLYEN, 1981; PAPADOPOULOS *et al.*, 2010).

Soil electrical properties (ε_{rg} and σ_g) can be estimated using suitable models that are applicable in engineering contexts. These models provide a means to characterize the frequency-dependent behavior of the soil properties. Considering frequency-dependent models provides valuable insights for analyzing and characterizing soil behavior in electromagnetic applications (PAPADOPOULOS; PAPAGIANNIS, 2007; SEMLYEN, 1981; PAPADOPOULOS *et al.*, 2010).

Several frequency-dependent soil models that are suitable for analyzing electromagnetic transients have been proposed in the existing literature (ALÍPIO; VISACRO, 2014; CAVKA *et al.*, 2014; LONGMIRE; SMITH, 1975).

In this work, the CIGRE WG C4.33 model will be used as the baseline model for frequency-dependent soils. This model was developed based on real soil analyses over a frequency range from 100 Hz to 4 MHz (WG-C4.33, 2019).

Figure 2.11. Comparison between constant and frequency-dependent soil properties from 1 Hz up to 1 MHz: (a) conductivity (σ_g) and (b) relative permittivity (ε_{rg}) for $\sigma_{g,LF} = 0.001$ [S/m].



Source: Own authorship.

According to CIGRE WG C4.33 model, ε_{rg} and σ_g are calculated as:

$$\varepsilon_{rg}(f) = 12 + 9.5 \cdot 10^4 \cdot \sigma_{g,LF}^{0.27} f^{-0.46}, \quad (2.100)$$

$$\sigma_g(f) = \sigma_{g,LF} + 4.7 \cdot 10^{-6} \cdot \sigma_{g,LF}^{0.27} f^{0.54}, \quad (2.101)$$

in which $\sigma_{g,LF} = \frac{1}{\rho_{g,LF}}$ is the soil conductivity at 100 Hz, in [S/m]; f is the frequency, in [Hz] and ε_{rg} is the soil relative permittivity. Figure 2.11 shows the difference between soil properties that vary with frequency and those that are constant in frequency, considering $\sigma_{g,LF} = 0.001$ [S/m].

The use of frequency-dependent soil models is recommended for electromagnetic transient studies in which soils with resistivity greater than 700 Ωm are encountered (WG-C4.33, 2019). Table 2.1 summarizes the relevance and recommendations concerning the frequency dependence effect of soil properties in various engineering applications.

Table 2.1. CIGRE recommendations concerning whether or not the frequency dependence of the soil properties should be considered for different engineering applications.

Application	Range of soil resistivity [Ωm]	Relevance	Recommendation
Grounding electrodes studies	$\rho_g < 300$	Not relevant	Ignore
	$300 \geq \rho_g \leq 700$	Relevant	Recommended
	$\rho_g > 700$	Very relevant	Mandatory
Transmission lines studies	$\rho_g < 300$	Not relevant	Ignore
	$300 \geq \rho_g \leq 700$	Relevant	Recommended
	$\rho_g > 700$	Very relevant	Mandatory
Induced voltages	$\rho_g < 2500$	Not relevant	Ignore
	$\rho_g \geq 2500$	Relevant	Recommended

Source: Adapted from (WG-C4.33, 2019).

2.8.4 Soil Frequency Regions and Critical Frequency

A variable known as the critical frequency provides comprehension into the electromagnetic polarization of soil, considering its electromagnetic parameters (ε_{rg} and σ_g). The critical frequency (f_{cr}) is defined as (PAPADOPOULOS; PAPAGIANNIS, 2007; SEMLYEN, 1981; PAPADOPOULOS *et al.*, 2010):

$$f_{cr} = \frac{\sigma_g}{2\pi\varepsilon_{rg}\varepsilon_0}. \quad (2.102)$$

Based on equation (2.102), three distinct regions can be identified, each describing the frequency-dependent behavior of soil (PAPADOPOULOS; PAPAGIANNIS, 2007; SEMLYEN, 1981; PAPADOPOULOS *et al.*, 2010):

- **Low frequency region** ($f < 0.1f_{cr}$): the soil behaves as a perfect conductor and the displacement current is negligible;

- **Transition region** ($0.1f_{cr} < f < 2f_{cr}$): the earth behaves both as a conductor and an insulator then, the displacement and resistive currents are comparable.
- **Very high frequency or surface wave region** ($f > 2f_{cr}$): the soil behaves mainly as an insulator, which corresponds to that the displacement current is predominant.

2.9 CHAPTER SUMMARY

This chapter provided a straightforward exposition of the main concepts necessary to build accurate models of double-circuit transmission lines.

Initially, the voltage and current relationships at the terminals of the transmission line were presented. Subsequently, the propagation parameters of the transmission line were introduced.

The classical formulas for calculating the impedances and admittances of transmission lines were presented, along with the generalized formulations that consider the conductive and ground leakage current, which form the basis of the research work.

Also, three basic types of ideal double-circuit transpositions and each type of inter-circuit coupling generated were explained, accompanied by the computations of parameters for grouped conductors and the simplification technique known as Kron reduction.

Finally, soil analysis methods and formulations considering frequency-dependent soil properties were introduced.

The theoretical foundations presented in this chapter are essential for understanding and subsequently modeling a transmission system in a realistic and accurate manner.

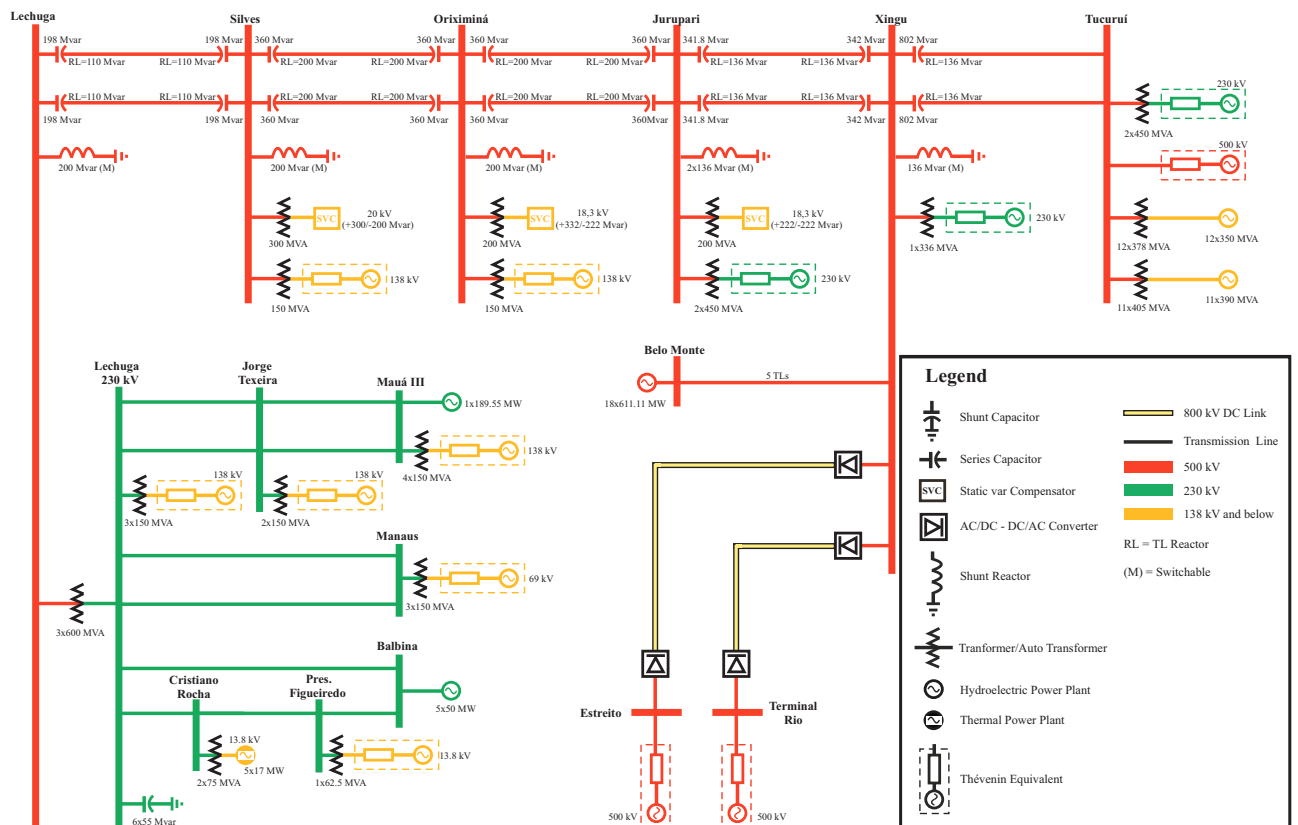
In the next chapter, the base transmission system for this work is presented, detailing the constructive aspects of the transmission line, the characteristics of the soil along the right-of-way, and how these aspects were considered in terms of computational modeling.

POWER SYSTEM DESCRIPTION AND CIRCUIT MODEL APPROACH

3.1 POWER SYSTEM DESCRIPTION

This study focuses on a transmission system located in the northern region of Brazil, whose single-line diagram is presented in Figure 3.1.

Figure 3.1. Single-line diagram of the Brazilian northern power grid.



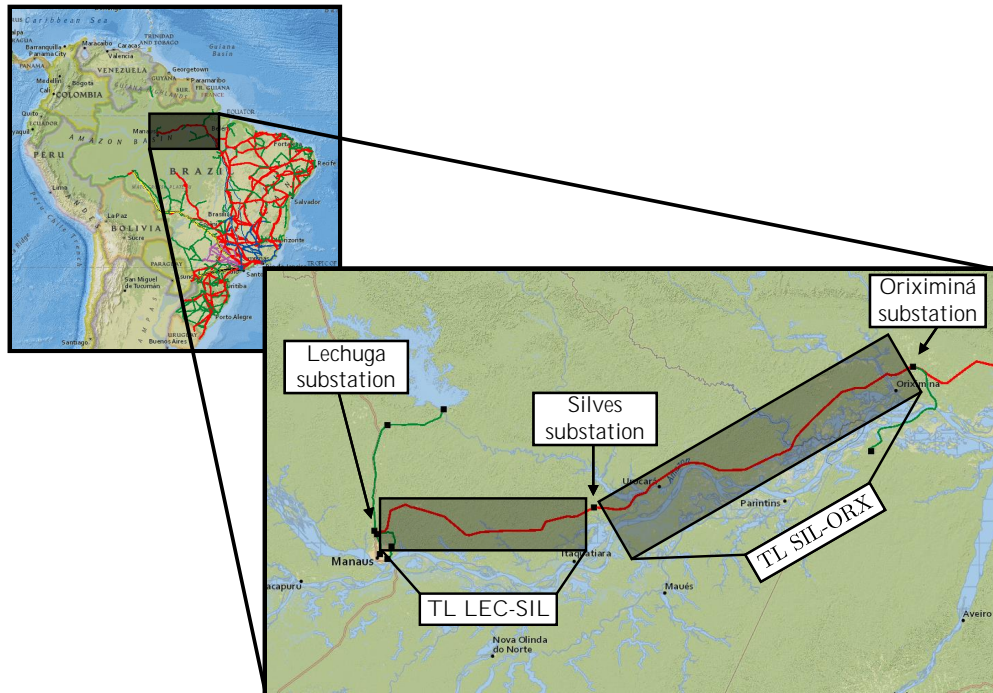
Source: Own authorship.

The power system grid comprises a network of interconnected components, including the 500 kV Lechuga (LEC) substation as the starting point. From Lechuga substation, 500 kV double-

circuit transmission lines extend through Silves (SIL) and continue to Tucuruí substation. The grid also incorporates the Belo Monte power plant and includes DC ± 800 kV lines that connect Xingu to Estreito and Terminal Rio substations.

The transmission system consists of 500 kV/60 Hz double-circuit transmission lines that interconnect three substations: Lechuga (LEC), Silves (SIL), and Oriximiná (ORX). The first transmission line (LEC-SIL TL) connects the Lechuga and Silves substations and is 223.76 km long. The second transmission line (SIL-ORX TL) extends through 333.45 km, connecting the Silves and Oriximiná substations. Figure 3.2 shows this interconnected transmission system.

Figure 3.2. Power transmission network map. The lines in red represent 500 kV transmission lines, the ones in green represent 230 kV transmission lines, and the black rectangles represent the substations.



Source: Adapted from <<https://gisepeprd2.epe.gov.br/webmapepe/>>.

The right-of-ways of these transmission lines extend through the Amazon rainforest, where the vegetation is dense and can reach heights of 40 to 110 meters, as shown in Figure 3.3. As a result, many faults occur in this transmission system, making the modeling and study of these electromagnetic transients necessary to understand the phenomena and contribute to the line's protection system for the optimal operation of the transmission system.

While the system comprises two double-circuit transmission lines, this study will specifically

Figure 3.3. Visualization of the vegetation and the transmission line right-of-way through the Amazon rainforest.



Source: Own autorship.

focus on the modeling details of the Silves-Oriximiná transmission line.

3.2 SILVES-ORIXIMINÁ TRANSMISSION LINE

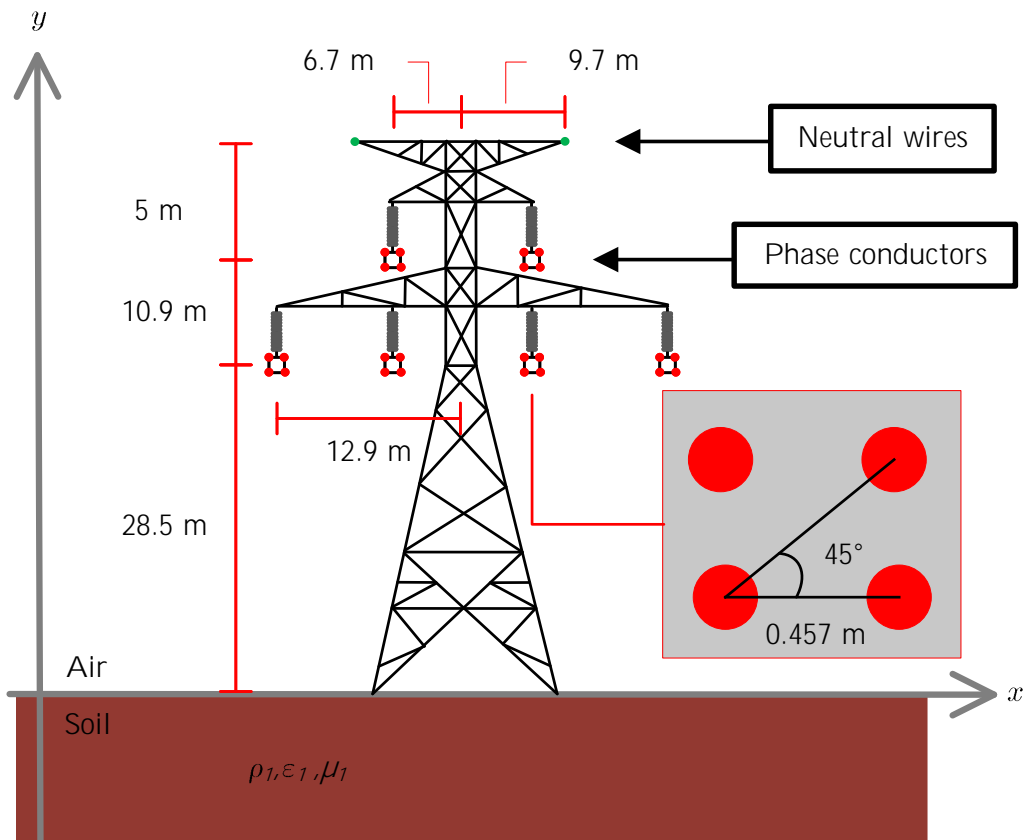
The Silves-Oriximiná transmission line (SIL-ORX TL) transmission line consists of a double-circuit transposed line that operates at 500 kV, a triangular phase conductor arrangement, and two shield wires, as shown in Figure 3.4.

The line circuit 1 is energized with a current of 400 A per phase, with ABC sequence, 60 Hz frequency and it is grounded at both terminal substations through earth resistance of 1Ω . Circuit 2 is energized with a current of 390 A per phase, with CBA sequence, 60 Hz frequency and it is also grounded with the same earth resistance of 1Ω at both terminals substations.

Each phase of the transmission line is composed of four bundled conductors in a square arrangement, as illustrated in Figure 3.4. Table 3.1 describes the transmission line conductors and the corresponding electrical characteristics.

The right-of-way extension is composed of 597 towers, each of which with grounding resistances of 15Ω , with an average span of 558 meters long.

Figure 3.4. 500 double-circuit Silves-Oriximiná transmission line cross-view.



Source: Own authorship.

The transposition scheme of the Silves-Oriximiná transmission line is composed of 4 sections with the "barrels" rolled in opposite directions, as shown in Figure 3.5.

3.3 SILVES-ORIXIMINÁ TRANSMISSION LINE SOIL ANALYSIS

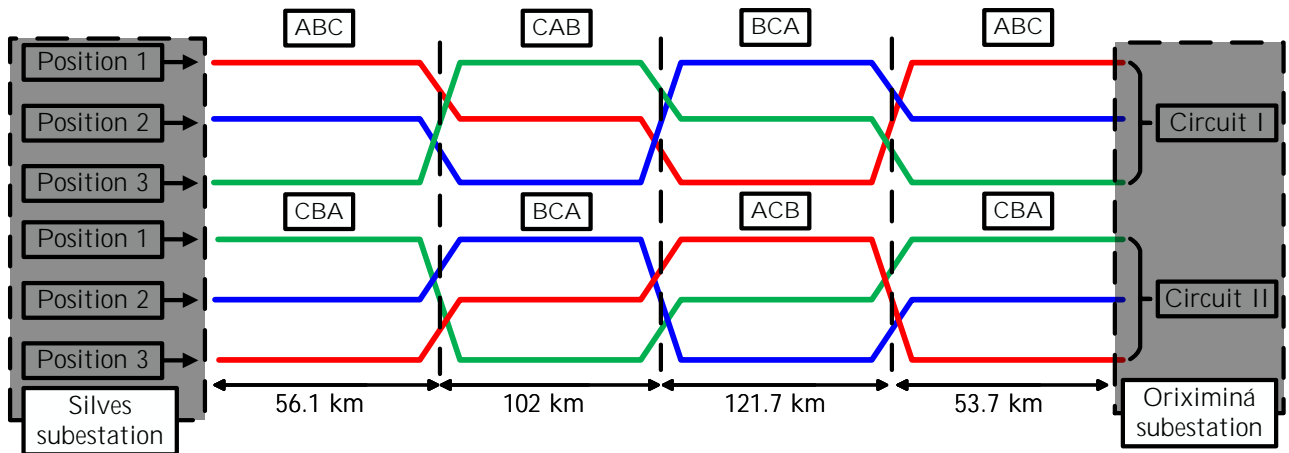
From October 2010 to March 2011, soil apparent resistivities were measured along the right-of-way. A total of 150 measurements were conducted using the Wenner method (see Section 2.8.1), which covers a distance of 333.45 km.

Given the considerable length of the transmission line, the right-of-way traversed a variety of terrains, including dry regions such as valleys and mountains, as well as wet areas like rivers and lakes. The geographical characteristics encountered during the measurements are depicted in Figure 3.6, providing a visual representation of the diverse landscapes crossed by the transmission line right-of-way.

Table 3.1. Specifications of the transmission line conductors

Conductor	Internal radius [m]	External radius [m]	DC Resistance [Ω /km]
AAAC -27	-	0.01462	0.068016
ACSR Dotterel	0.0046228	0.0077089	0.306336

Source: Own authorship.

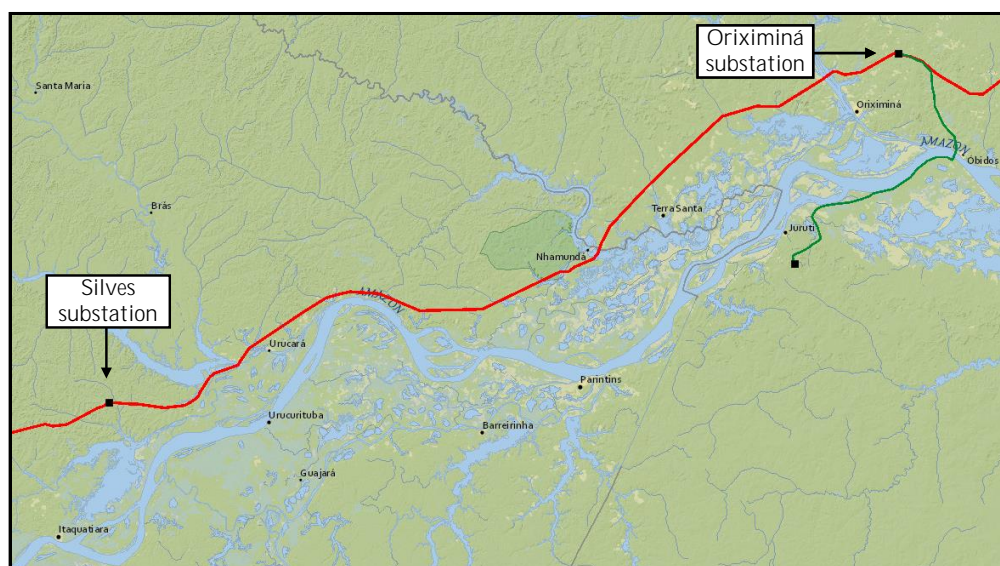
Figure 3.5. Real transposition scheme applied in the 500 kV double-circuit Silves-Oriximiná transmission line.

Source: Own autorship.

Intended to construct the most representative soil models from the 150 measurements points along the right-of-way, all multilayered soil models are built on RESAP, a computational module present in the Current Distribution Electromagnetic Interference Grounding and Soil Structure Analysis (CDEGS) package, which is worldly reputed as the industry standard for the calculation of EMIs, substation, and tower grounding studies (DAWALIBI; BLATTNER, 1984).

In this study, the field measurements are processed using RESAP, which results in 150 multilayered soil models, calculated as presented in Section 2.8.2. Although the impedance and admittance formulations, presented in Sections 2.2.2 and 2.3.2, are applied only to homogeneous soils, the general applicability of the method is maintained. Since the deep layer resistivity values obtained from the RESAP processing can be used as an equivalent uniform soil resistivity with validity (MARTINS-BRITTO *et al.*, 2019; MARTINS-BRITTO *et al.*, 2020).

Using the bottom layer resistivity for electromagnetic transient studies has proven to be compatible and yielded similar results to equivalent uniform models for N-layered soils, within

Figure 3.6. Silves-Oriximiná transmission line map.

Source: Adapted from <<https://gisepeprd2.epe.gov.br/webmapepe/>>.

the frequency range of 60 Hz to 1 MHz (MARTINS-BRITTO *et al.*, 2019; MARTINS-BRITTO *et al.*, 2020).

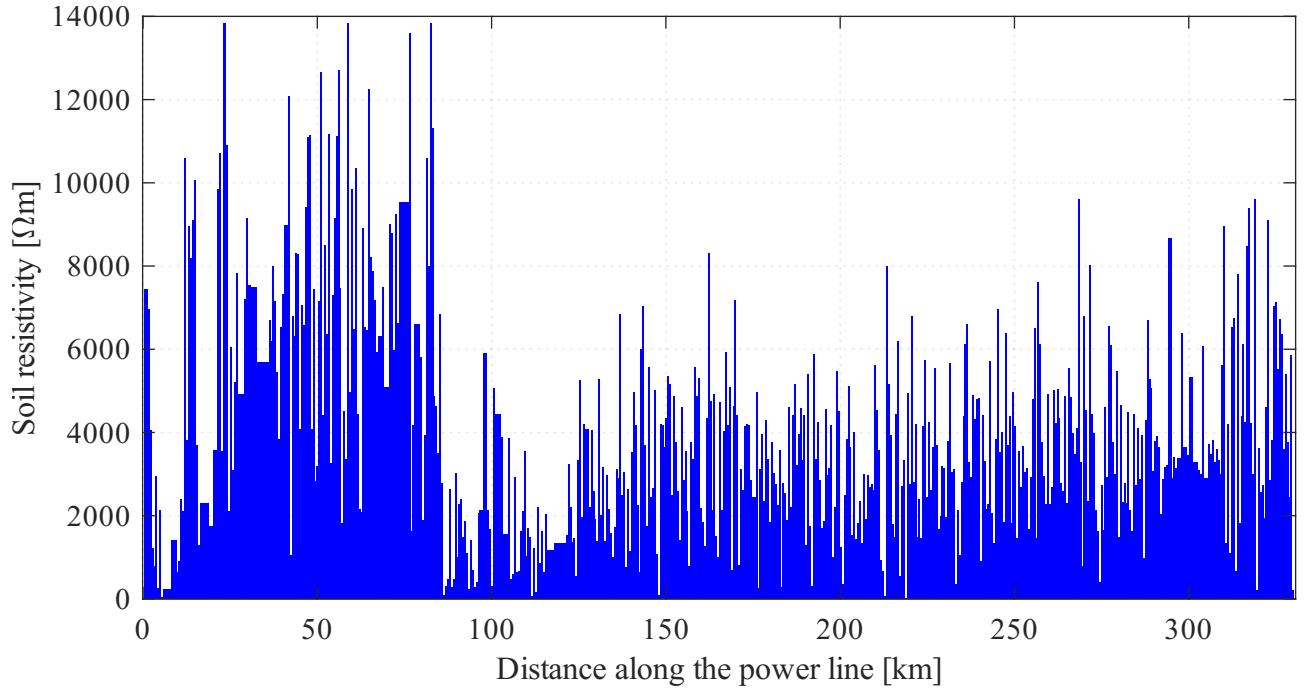
The soil resistivity values along the Silves-Oriximiná transmission line are summarized in Table A.2 and are shown in Figure 3.7, which it is evident that there is a significant variation in resistivity values along the right-of-way. The regions with lower resistivity values (from \approx 75 km to 125 km) are represented by the waterlogged areas, while the higher resistivity values (from \approx 25 km to 70 km) correspond to the dry or rocky regions traversed by the transmission line.

The minimum, maximum and average resistivity values are presented in Table 3.2. It is observed that the resistivity variation from the highest value to the lowest value is approximately 346 times.

Table 3.2. Minimum, average and maximum soil resistivity along the right-of-way.

	Soil resistivity [Ωm]
Minimum	40.0
Average	4324.63
Maximum	13832.39

Source: Own authorship.

Figure 3.7. Deep-layer soil resistivity along the 500 kV Silves-Oriximiná double-circuit transmission line.

Source: Own autorship.

Relative permittivity values (ϵ_{rg}) are classified based on the soil resistivity into different ranges, as summarized in Table 3.3 (MARTINS-BRITTO *et al.*, 2022).

Table 3.3. Relative permittivity range values.

Relative soil permittivity	
$0 < \rho_g \leq 100$	1
$100 < \rho_g \leq 5000$	3
$\rho_g \geq 5000$	5

Source: Own authorship.

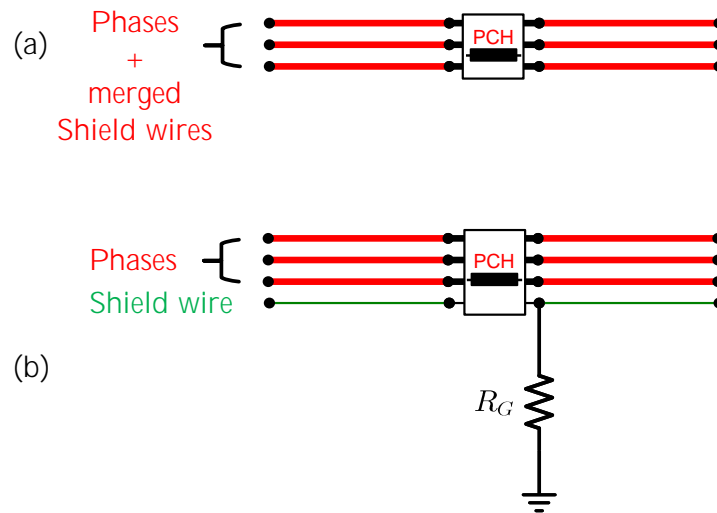
3.4 EMTP/ATP CIRCUIT MODEL FOR EACH TRANSMISSION LINE SPAN

It is well understood that the spans of transmission lines vary in parameters (soil, tower geometry, span length) along the entire path due to physical obstacles and challenges in the terrain through the right-of-way.

Assuming the soil resistivity and the tower geometry to be constants along each span, the

circuit for one span section is built according to Figure 3.8, which exemplifies the particular case (with no loss of generality) of (a) a three-phase line with a shield wire using Kron reduction simplification, and (b) a three-phase line with the "explicit" shield wire, without employing Kron reduction, modeled using the ATPDraw interface.

Figure 3.8. ATPDraw representation of one section (span) of: (a) a three-phase line with one shield wire using Kron reduction simplification, and (b) a three-phase line with an "explicit" shield wire, without Kron simplification. Resistance R_G represents the tower grounding.



Source: Own autorship.

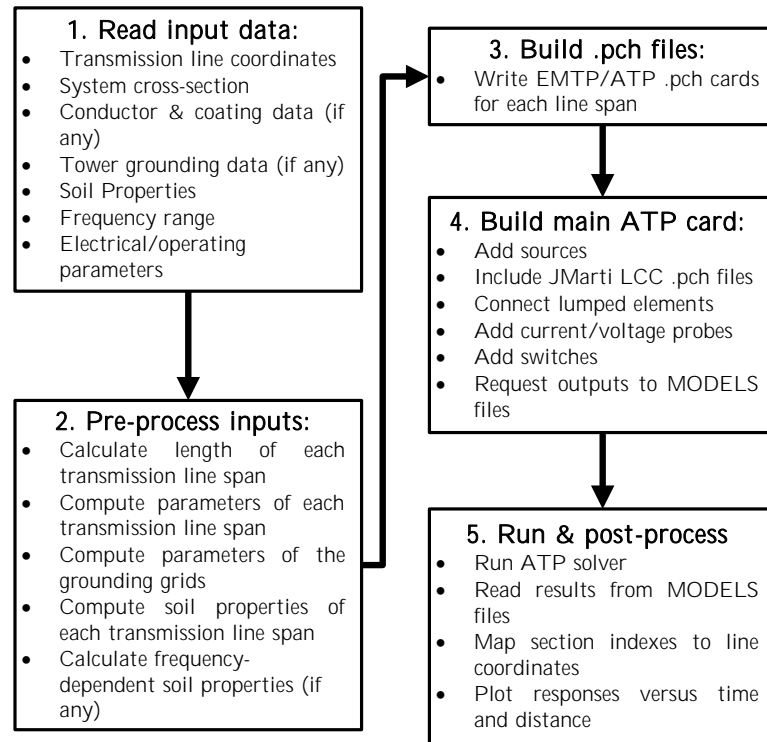
Each transmission line span is represented by a punch (.pch) file loaded as a JMarti Line Constants (LCCs) object, which is constructed with the corresponding cross-section, soil resistivity, and system frequency. Ground resistances R_G at tower locations are determined from grounding electrode geometries and soil resistivities.

The impedances and admittances of each span are calculated using Wise formulations, with a frequency range from 1 Hz to 1 MHz. Once these parameters are computed, the modal parameters of each phase are determined using the Levenberg-Marquardt algorithm enhanced with an eigenvector correlation technique to prevent frequency-domain switchovers, as detailed in Section 2.7.

Lastly, after obtaining the modal parameters for each conductor, the propagation parameters are recorded in a punch (.pch) file using a format compatible with EMTP/ATP. The punch file is modeled as the software generates and reads LCC JMarti cards.

With the necessary parameters at hand, complex systems are built by successively concatenating the individual cells described above. A basic flowchart of the proposed computational implementation to build complex transmission lines in EMTP/ATP is shown in Figure 3.9.

Figure 3.9. Flowchart of the proposed EMTP/ATP computational implementation.



Source: Own autorship.

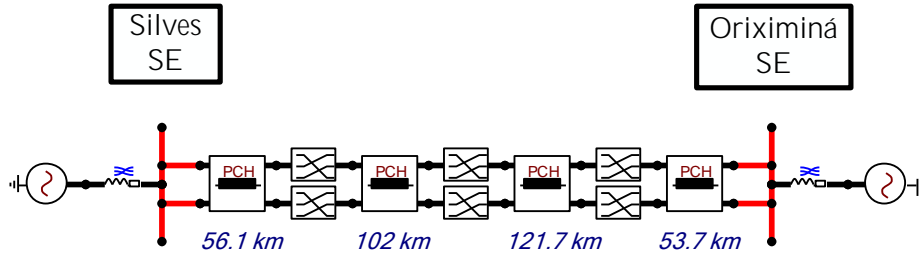
3.5 VALIDATION OF SILVES-ORIXIMINÁ TRANSMISSION LINE MODELING IN EMTP/ATP

Using the implementation of the 500 kV Silves-Oriximiná transmission line is built, as presented in the previous section, it is possible to validate the performance of the computational power system with the real system.

On May 1st and 2nd, 2021, an opening for maintenance was performed on some of the circuits, and oscillography data were collected at the Oriximiná and Silves substations, allowing the observation of voltages and currents in the circuits of these buses (ABB; EVOLTZ, 2021).

The Silves-Oriximiná transmission line steady-state EMTP/ATP equivalent circuit, as presented in Figure 3.10, is adapted to represent the topology of aforementioned power plant grid

Figure 3.10. EMTP/ATP steady-state model representation for Silves-Oriximiná transmission line.



Source: Own authorship.

(see Figure 3.1) through Thévenin equivalent impedances and balancing the power flow, maintaining the level of detail established to represent the transmission system implemented in the field with the computational model proposed in this work.

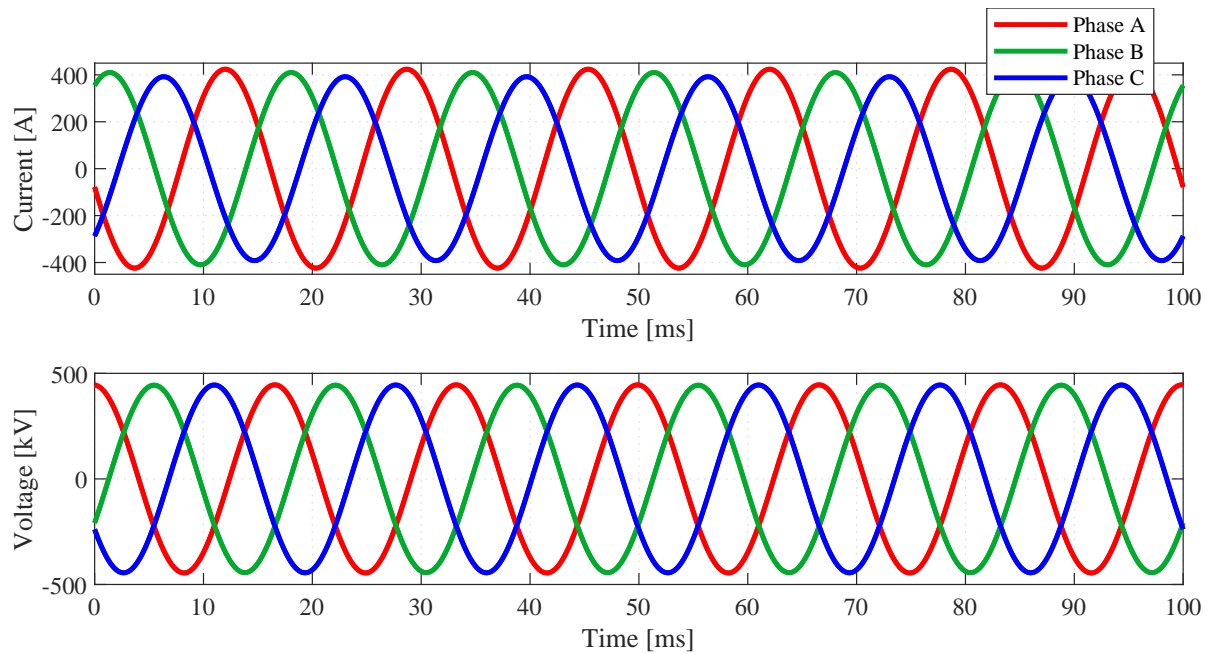
3.5.1 Silves Substation

The computationally simulated voltage and current values of the Silves-Oriximiná transmission line measured at the Silves substation are shown in Figures 3.11 and 3.12. Figure 3.11 presents the steady-state voltage and current values for Circuit 1, while Figure 3.12 presents the same simulated variables for Circuit 2 of the transmission line.

Based on the technical report ABB & Evoltz (2021), produced by Hitachi ABB in conjunction with Evoltz (the company responsible for the concession contract of the transmission line), Table 3.4 compares the voltage and current peak values simulated in EMTP/ATP with the values measured in the field at Silves substation. Table 3.4 also presents the absolute errors of current and voltage for each phase in both circuits of the transmission line.

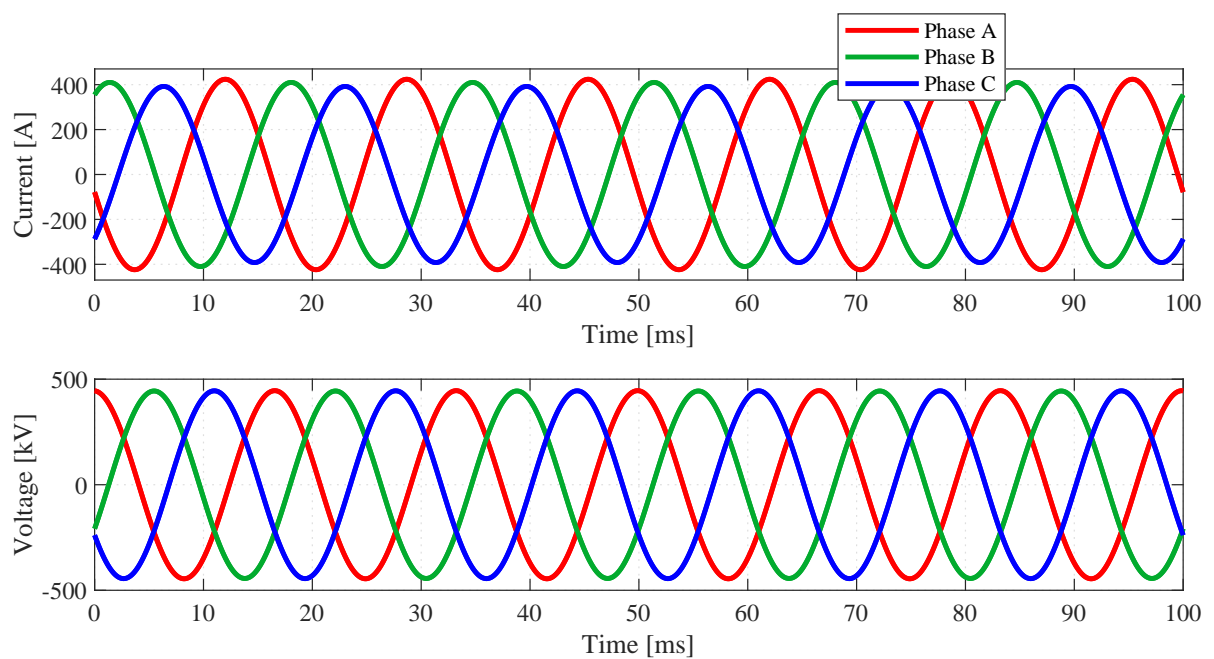
It is observed that the voltage and current values in all phases of both circuits are very close to the voltage and current values measured in the field on May 1, 2021. Considering the currents, the implemented circuit model exhibited a discrepancy of less than 8% compared to the field values. For the voltages, the results are even better, with a discrepancy below 3% absolute error.

Figure 3.11. Silves-Oriximiná transmission line currents and voltages under nominal load conditions for the circuit 1 at Silves substation.



Source: Own autorship.

Figure 3.12. Silves-Oriximiná transmission line currents and voltages under nominal load conditions for the circuit 2 at Silves substation.



Source: Own autorship.

Table 3.4. Comparison between simulated and field measured voltages and currents in the Silves-Oriximiná transmission line at Silves substation.

Phase (Circuit)	Peak current [A]		Peak voltage [kV]		Error [%]	
	Real	EMTP/ATP	Real	EMTP/ATP	Current	Voltage
A (C1)	394.62	423.94	433.56	445.45	7.43	2.74
B (C1)	399.4	409.74	433.72	439.98	2.59	1.44
C (C1)	398.28	392	435.25	447.76	1.58	2.87
A (C2)	399.21	412.07	435.59	445.5	3.22	2.28
B (C2)	397.12	410.7	438.79	443.99	3.42	1.19
C (C2)	397	395.57	436.99	444.77	0.36	1.78

Source: Own authorship with data obtained from (ABB; EVOLTZ, 2021).

3.5.2 Oriximiná Substation

As Silves substation, the simulated steady-state transmission line currents and voltages at the Oriximiná substation are shown in Figures 3.13 and 3.14 for circuits 1 and 2, respectively.

Table 3.5 summarizes the peak values of simulated voltages and currents and compares them with the field values obtained from the ABB & Evoltz (2021) technical report.

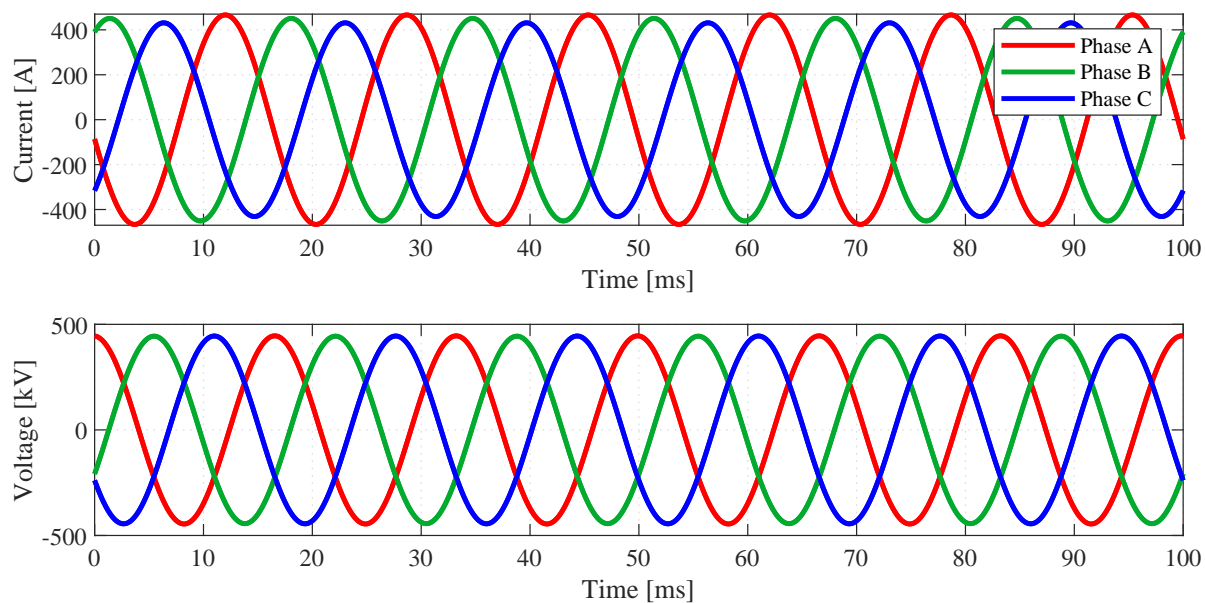
Despite the circuit implementation show more discrepant values at the Oriximiná substation compared to the measured values, the circuit model still manages to adhere to the field values.

The currents exhibited an error of less than 9% for all phases of the Silves-Oriximiná transmission line.

The simulated voltages showed better adherence to the field measurements, with a maximum discrepancy of 3% compared to the values presented in the technical report for the Oriximiná substation.

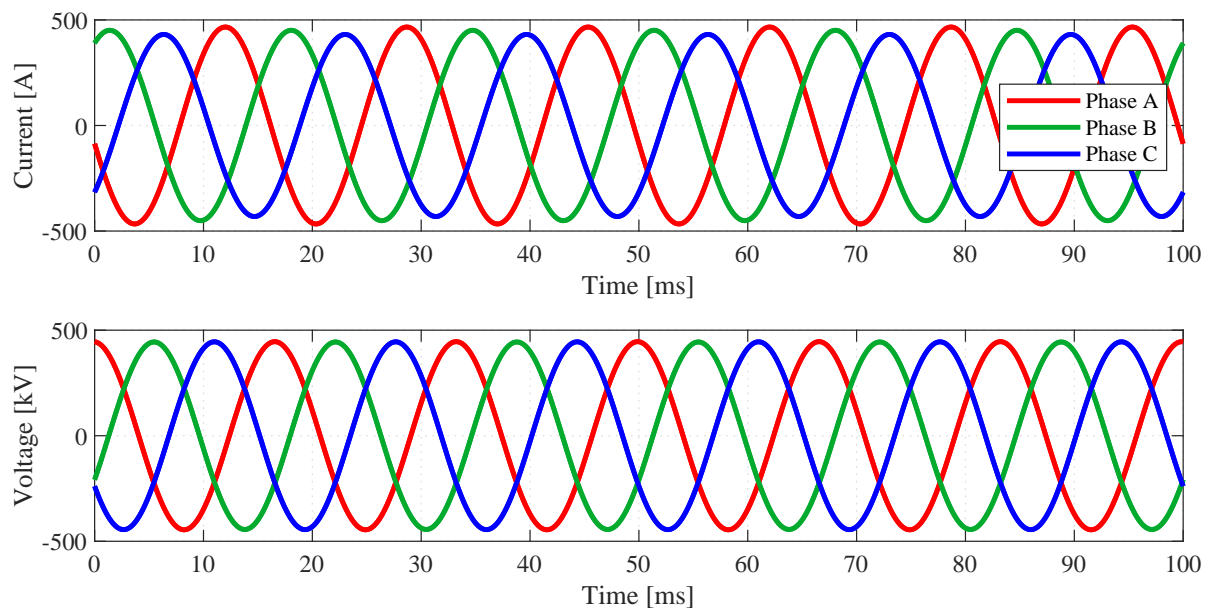
All steady-state currents and voltages in Silves-Oriximiná transmission line responses calculated by the proposed circuital implementation presented an absolute error of less than 10% compared to real field values measured on May 1, 2021. Thus, the proposed methodology can be considered valid and accurate for the study of EMT.

Figure 3.13. Silves-Oriximiná transmission line currents and voltages under nominal load conditions for the circuit 1 at Oriximiná substation.



Source: Own autorship.

Figure 3.14. Silves-Oriximiná transmission line currents and voltages under nominal load conditions for the circuit 2 at Oriximiná substation.



Source: Own autorship.

Table 3.5. Comparison between simulated and field measured voltages and currents in the Silves-Oriximiná transmission line at Oriximiná substation.

Phase (Circuit)	Peak current [A]		Peak voltage [kV]		Error [%]	
	Real	EMTP/ATP	Real	EMTP/ATP	Current	Voltage
A (C1)	395.48	433.5	432.42	445.4	9.61	3.00
B (C1)	399.06	429.74	432.4	443.98	7.69	2.68
C (C1)	397.09	423.28	433.27	444.76	6.60	2.65
A (C2)	397.91	435.94	437.47	440.5	9.56	0.69
B (C2)	400.99	420.4	440.06	442.01	4.84	0.44
C (C2)	398.81	419.13	434.08	441.46	5.10	1.70

Source: Own authorship with data obtained from (ABB; EVOLTZ, 2021).

3.6 CHAPTER SUMMARY

In this chapter, a detailed description of the power system under study is provided, and the circuit model approach for analyzing the transmission line is presented. The transmission line is analyzed using a circuit model approach, and the power system under study is described in detail. A network of interconnected components constitutes the power system, which is located in the northern region of Brazil. The single-line diagram of the Brazilian northern power grid is presented, with emphasis placed on the Lechuga (LEC) substation as the starting point. Substations including Lechuga, Silves, and Oriximiná are connected by 500 kV double-circuit transmission lines in the transmission system. Additionally, the grid incorporates the Belo Monte power plant and DC \pm 800 kV lines that connect Xingu to Estreito and Terminal Rio.

The focus of this study lies on the Silves-Oriximiná transmission line (SIL-ORX TL), which operates at 500 kV and is a double-circuit transposed line. The line features a triangular phase conductor arrangement with two shield wires. The chapter provides the circuit parameters, such as current, sequence, and grounding resistance, for both circuits. The transmission line consists of four bundled conductors in each phase, and their specifications are described in the chapter.

The right-of-way of the transmission line extends through the Amazon rainforest, which is characterized by dense vegetation. The challenges posed by the vegetation height along the right-of-way are highlighted through visualizations included in the chapter. The transposition scheme applied to the Silves-Oriximiná transmission line is presented, demonstrating the

arrangement of barrels in opposite directions.

An analysis of the soil along the Silves-Oriximiná transmission line is conducted to comprehend the variations in resistivity. Soil resistivity measurements were performed along the 333.45 km right-of-way using the Wenner method. The measurements encompass diverse terrains, including wet areas such as rivers and lakes, as well as dry regions like valleys and mountains. A map depicting the geographical characteristics encountered during the measurements is provided. The obtained soil data from the measurements are processed using the RESAP program, resulting in 150 multilayered soil models. The resistivity values of the bottom layer are utilized for electromagnetic transient studies.

Significant variations in soil resistivity are observed along the transmission line, with lower values in waterlogged areas and higher values in dry or rocky regions. The chapter presents the minimum, average, and maximum resistivity values, demonstrating a wide range of resistivity along the right-of-way. The classification of relative permittivity values is based on soil resistivity ranges.

Moreover, the circuit model approach for each transmission line span is introduced. The circuit models are constructed assuming constant soil resistivity and tower geometry within each span section. The representation of the circuit models for both a three-phase line with a shield wire using Kron reduction simplification and a three-phase line with an "explicit" shield wire without Kron simplification is accomplished using the ATPDraw interface. The circuit models incorporate tower grounding resistance.

The chapter ends with a comparison between the proposed circuit implementation and the field measurements taken on May 1, 2021. The results demonstrate that the circuit implementation is valid and represents the Silves-Oriximiná transmission line under nominal operating conditions, exhibiting less than a 10% discrepancy between the simulated and field-measured values.

In the next chapter, the propagation parameters in the double-circuit Silves-Oriximiná transmission line will be analyzed. The investigation will include the analysis of variations in soil properties, the examination of suitable transposition methods, and a comparison of modal parameters using Kron reduction and "explicit" shield wires.

PROPAGATION PARAMETERS STUDY

This chapter addresses the analysis of propagation parameters in a double-circuit transmission line. Three main parameters are studied: variations in soil properties (resistivity and relative permittivity), suitable transposition methods for double-circuit lines, and a modal parameters comparison between a system using Kron reduction and a system that considered the use of "explicit" shield wires.

4.1 SOIL INFLUENCES ON SYMMETRICAL COMPONENTS

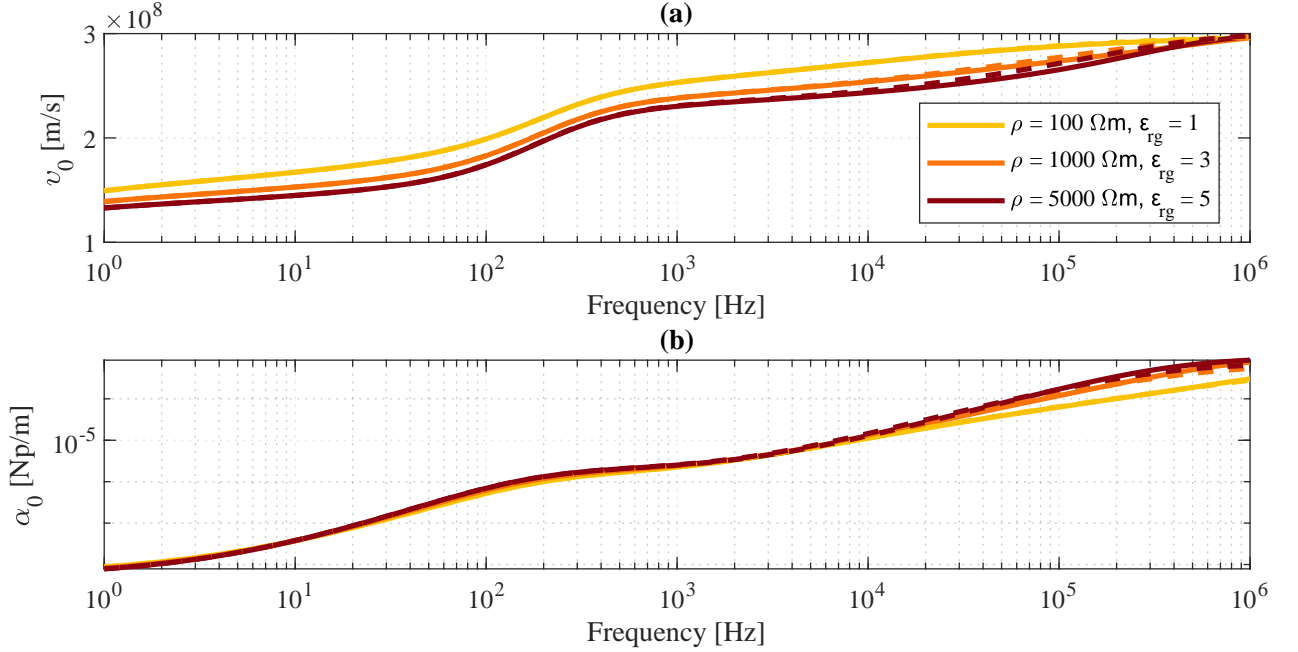
Three types of soil properties are used for this analysis: (a) $\rho = 100 \text{ } \Omega\text{m}$ and $\varepsilon_{rg} = 1$, (b) $\rho = 1000 \text{ } \Omega\text{m}$ and $\varepsilon_{rg} = 3$, and (c) $\rho = 5000 \text{ } \Omega\text{m}$ and $\varepsilon_{rg} = 5$. For these soil types, constant-frequency (CP) soil models are considered (represented by solid lines in the graphs) as well as frequency-dependent (FD) soil models (represented by dashed lines in the graphs). The FD soil model used is the CIGRE WG C4.33 model, calculated as shown in (2.100)-(2.101).

Since the transmission line is symmetric and perfectly transposed using the nine-section method, it is possible to use the $\mathbf{T}_{\mathbf{6}\text{-phases}}$, presented in (2.66), to obtain a decoupled modal matrix based on the symmetric components of the transmission line. From the six resulting decoupled components obtained from the transformation (2.65), only three components are present: the zero sequence (p_0), the zero sequence coupling ($p_0^{\text{I-II}}$), and the positive sequence (p_1) components. This occurs due to the positive and negative sequence components for the both circuits are identical due to the particularity of the line being symmetric and having the same constructive aspects.

The attenuation constant and phase velocity for the zero sequence (p_0), the zero sequence coupling ($p_0^{\text{I-II}}$), and the positive sequence (p_1) are presented in Figures 4.1, 4.2, and 4.3, respectively. It is observed that the most affected by the change in soil properties modes are

the zero sequence and zero sequence coupling components. These symmetrical components are directly influenced by the soil resistivity and relative permittivity.

Figure 4.1. Zero sequence component propagation characteristics considering different soil properties: (a) phase velocity, and (b) attenuation constant. Solid lines represent the CP soil models and dashed lines represent the FD soil models.



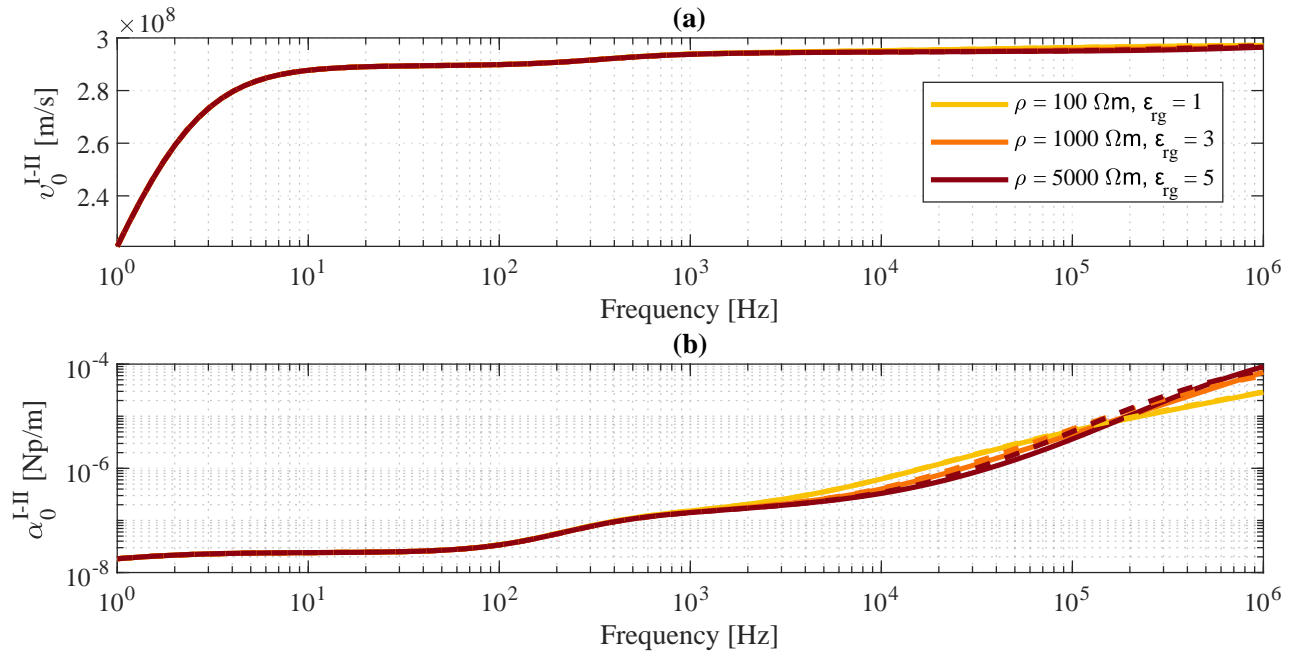
Source: Own authorship.

The zero sequence component is characterized by a higher attenuation and a slower phase velocity compared to the zero sequence coupling and positive sequence components. The path through the earth has an inductive impedance effect at low frequencies, which decreases with increasing frequency. At high frequencies, the soil primarily exhibits a capacitive effect, as explained in Section 2.8.4.

More conductive soils ($\rho = 100 \Omega\text{m}$) produce higher phase velocities and lower attenuations throughout the frequency spectrum. Additionally, it is observed that frequency-dependent soil models exhibit lower attenuations and higher phase velocities at high frequencies, attributed to the increased conductivity with frequency.

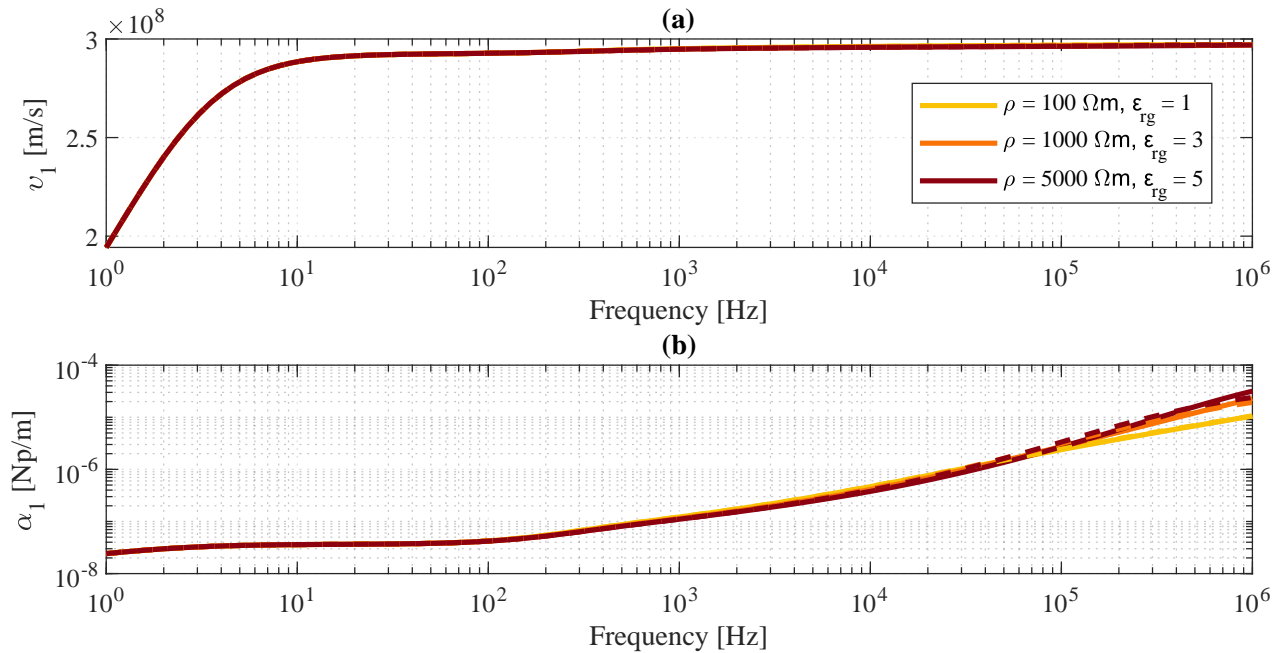
Both the positive and zero sequence coupling components exhibit almost constant attenuation across a broad range of frequencies, and their velocities converge to the speed of light in free space at high frequencies.

Figure 4.2. Zero sequence coupling component propagation characteristics considering different soil properties: (a) phase velocity, and (b) attenuation constant. Solid lines represent the CP soil models and dashed lines represent the FD soil models.



Source: Own authorship.

Figure 4.3. Positive sequence component propagation characteristics considering different soil properties: (a) phase velocity, and (b) attenuation constant. Solid lines represent the CP soil models and dashed lines represent the FD soil models.



Source: Own authorship.

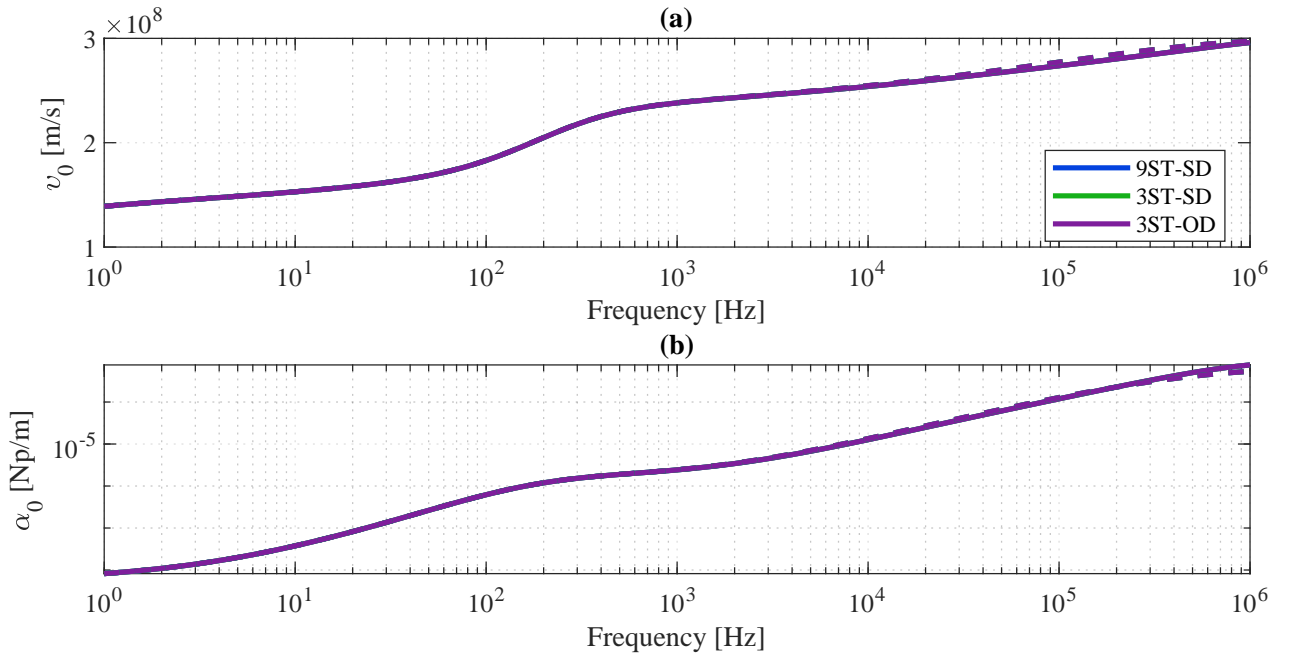
Although the two aerial modes are less affected by soil properties, it is noticeable that at high frequencies, the attenuation increases with higher values of soil resistivity.

4.2 TRANSPOSITION SCHEME INFLUENCES ON SYMMETRICAL COMPONENTS

The types of transposition schemes are also investigated to analyze their effects on symmetrical components across the frequency spectrum. The soil considered in all scenarios has a resistivity of $1000 \Omega\text{m}$ and a relative permittivity of 3. As in the previous case, the transformation matrix $\mathbf{T}_{6\text{-phases}}$ based on the symmetrical components of the double-circuit transmission line is used.

The the zero sequence (p_0), the zero sequence coupling ($p_0^{\text{I-II}}$), and the positive sequence (p_1) components for the nine-section transposition (9ST-SD), three-section transposition rotating phases in the same direction (3ST-SD), and rotating phases in the opposite direction (3ST-OD) are presented in Figures 4.4, 4.5, and 4.6, respectively.

Figure 4.4. Zero sequence component propagation characteristics considering different transposition schemes: (a) phase velocity, and (b) attenuation constant. Solid lines represent the CP soil models and dashed lines represent the FD soil models, both with $\rho = 1000 \Omega\text{m}$ and $\varepsilon_{rg} = 3$.

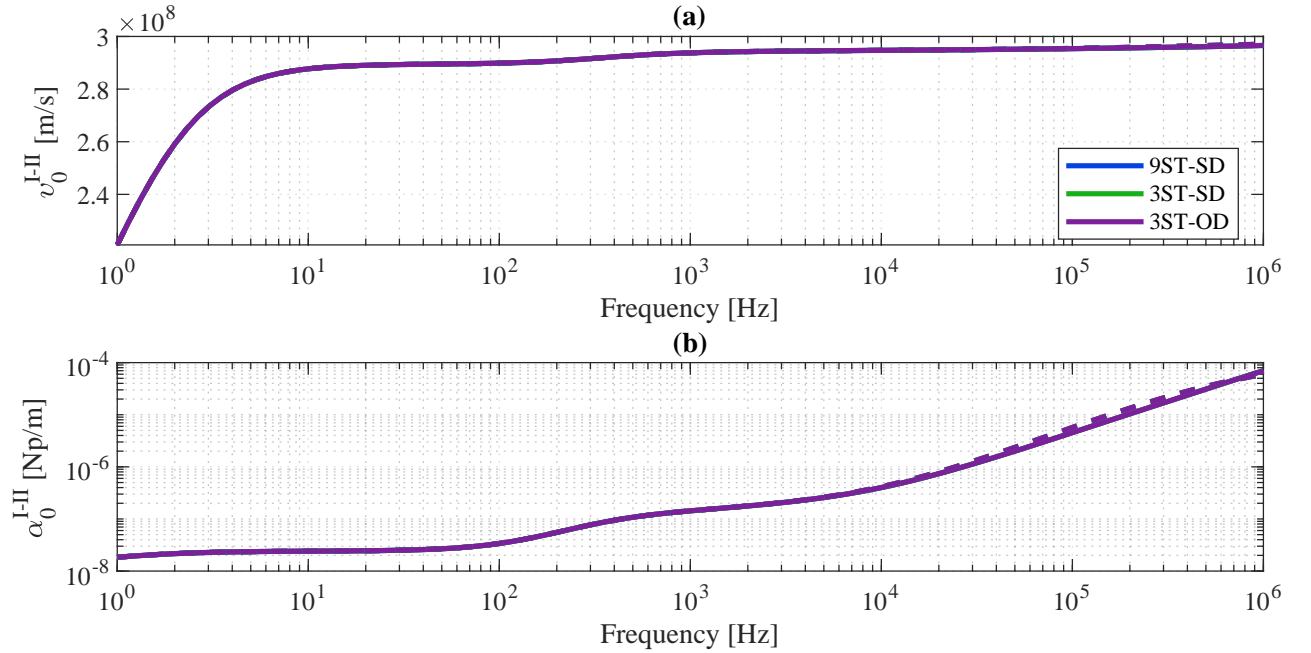


Source: Own authorship.

The symmetrical components propagation parameters are found to be the same regardless

of the transposition scheme adopted in the transmission line. The attenuation and velocity curves are perfectly overlapped for the 9ST-SD, 3ST-SD, and 3ST-OD transpositions.

Figure 4.5. Zero sequence coupling component propagation characteristics considering different transposition schemes: (a) phase velocity, and (b) attenuation constant. Solid lines represent the CP soil models and dashed lines represent the FD soil models, both with $\rho = 1000 \text{ } \Omega\text{m}$ and $\varepsilon_{rg} = 3$.

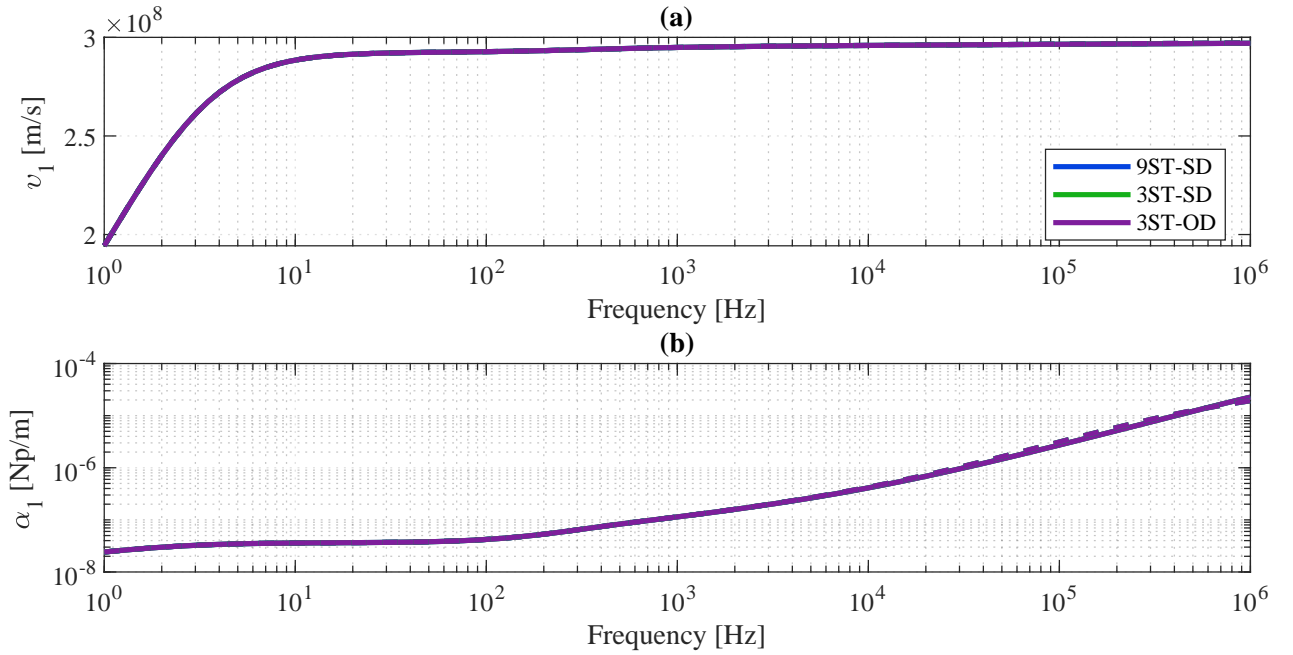


Source: Own authorship.

Since in the transformation from the phase domain to the sequence domain, the impedance and admittance values of zero, negative, and positive sequence components of both decoupled circuits are equal regardless of the adopted transposition scheme. The difference in the sequence matrix between the 9ST-SD scheme and the others is introduced by the positive and negative sequence inter-circuit coupling terms.

Although the decoupled sequence parameters of the circuits are the same, it is expected that some differences in the modal propagation parameters, especially for the zero sequence coupling component, would arise when the line is transposed by the 3ST-SD and 3ST-OD schemes due to the inclusion of the positive and negative sequence inter-circuit coupling. The inclusion of these components represents a higher inductive coupling between the two circuits. Then, it can be inferred that the use of symmetrical components does not accurately represent the physical phenomena existing between the circuits.

Figure 4.6. Positive sequence component propagation characteristics considering different transposition schemes: (a) phase velocity, and (b) attenuation constant. Solid lines represent the CP soil models and dashed lines represent the FD soil models, both with $\rho = 1000 \Omega\text{m}$ and $\varepsilon_{rg} = 3$.



Source: Own authorship.

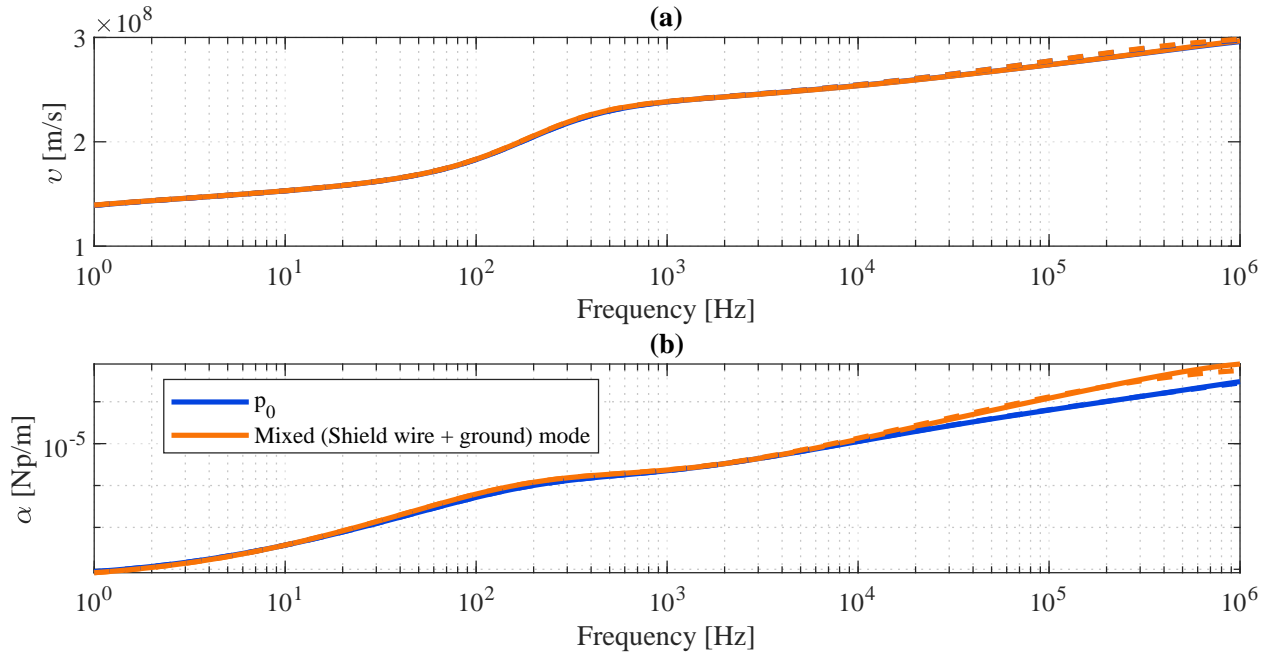
4.3 SYMMETRICAL COMPONENTS VERSUS MODAL PARAMETERS

4.3.1 Equivalent Kron-reduced System

In this topic, the symmetrical components are compared with the modal parameters derived from the eigenvalues and eigenvectors of the system, as presented in (2.88). Firstly, the Kron-reduced system is analyzed, to determine if the propagation characteristics of the system based on symmetrical components is compatible with the frequency-variant modal system. The same system used considered the 9ST transposition and soil resistivity of $\rho = 1000 \Omega\text{m}$ and relative permittivity of 3.

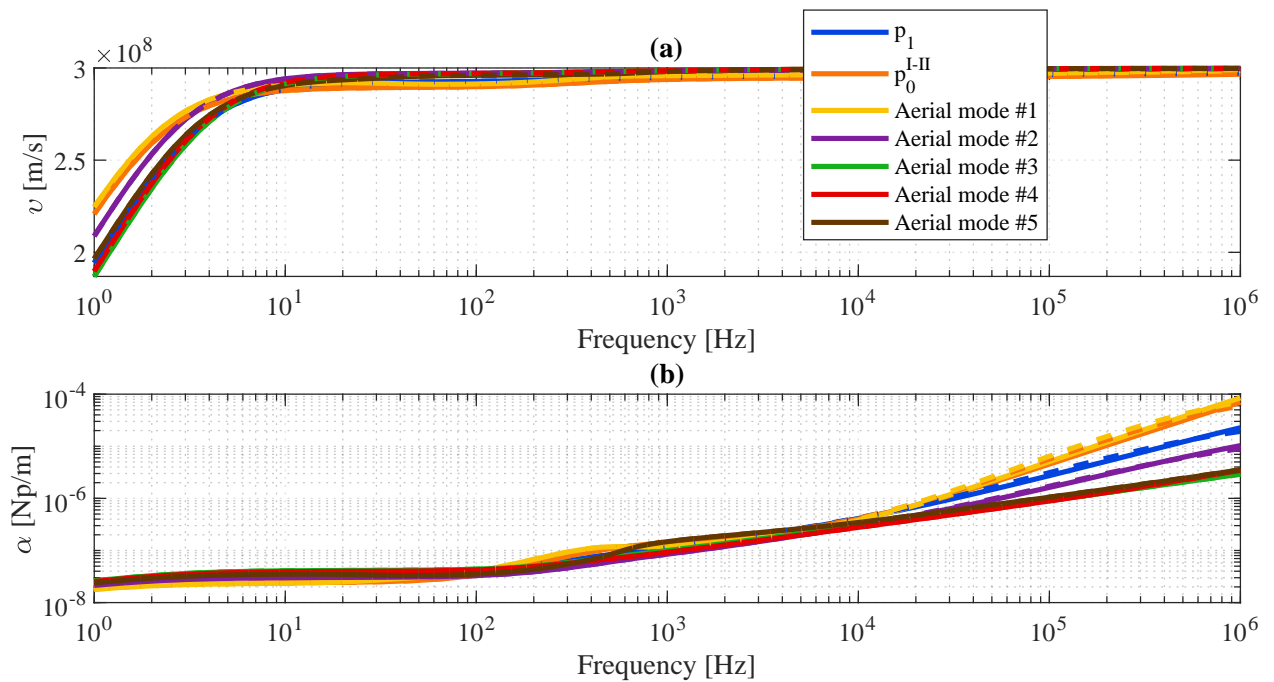
The propagation parameters of the ground-related modes are shown in Figure 4.7. The propagation parameters of the aerial modes are presented in Figure 4.8. Observing the ground-related propagation modes, it is noticeable that the zero sequence component has the same phase velocity as the ground mode from the modal domain.

Figure 4.7. Ground modes propagation characteristics considering symmetrical components and modal parameters with Kron reduction: (a) phase velocity, and (b) attenuation constant. Solid lines represent the CP soil models and dashed lines represent the FD soil models, both with $\rho = 1000 \Omega\text{m}$ and $\varepsilon_{rg} = 3$.



Source: Own authorship.

Figure 4.8. Aerial modes propagation characteristics considering symmetrical components and modal parameters with Kron reduction: (a) phase velocity, and (b) attenuation constant. Solid lines represent the CP soil models and dashed lines represent the FD soil models, both with $\rho = 1000 \Omega\text{m}$ and $\varepsilon_{rg} = 3$.



Source: Own authorship.

However, it should be noted that the modal domain ground mode is not a pure ground mode, as the shield wires are incorporated into the system through Kron reduction. Therefore, the ground mode is biased by the propagation parameters of the shield wires, resulting in a mixed mode.

Despite the similar phase velocity between the mixed mode and the zero sequence component, there is a difference in attenuation between these two modes at high frequencies.

Regarding the aerial modes, both in the symmetrical components and the modal-domain, they are more similar throughout the frequency spectrum. However, a difference in attenuation is also observed at high frequencies.

To highlight the differences between each approach, normalized propagation parameters (p_{norm}), are provided as the ratio concerning symmetrical-domain results

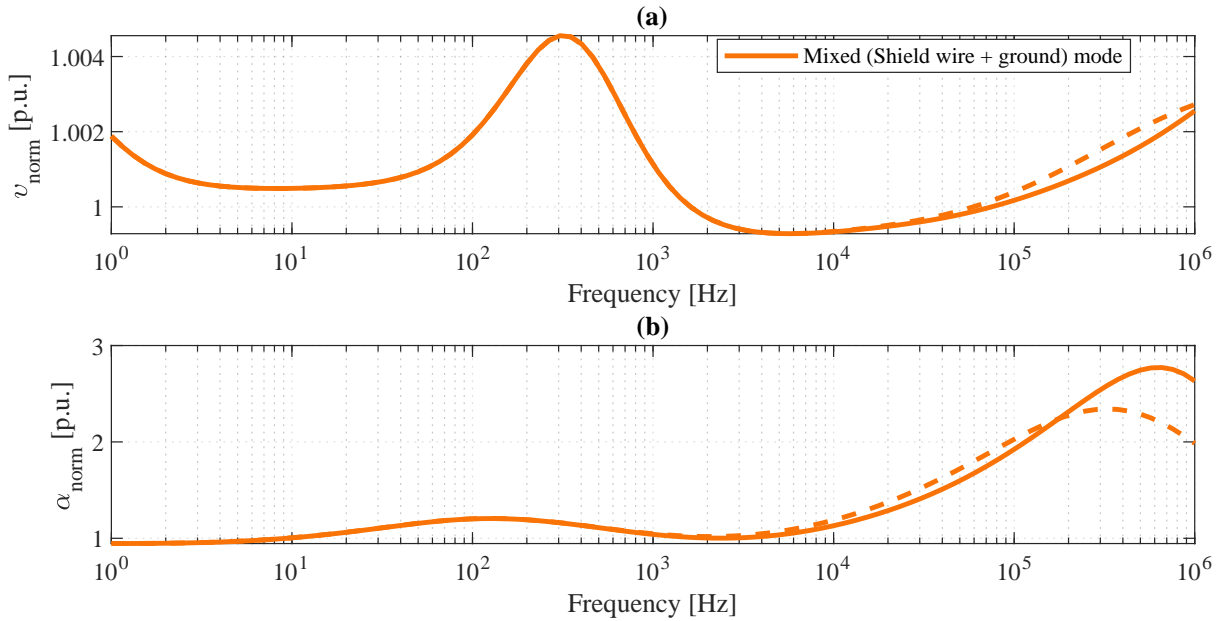
$$p_{norm} = \frac{\text{Propagation characteristics}_{modal-parameters}}{\text{Propagation characteristics}_{symmetrical-components}}. \quad (4.1)$$

The normalized ground mode attenuation constant and phase velocity are presented in Figure 4.9 as a function of frequency. The corresponding normalized propagation parameters for the aerial modes are summarized in Figure 4.10 and 4.11 for the zero sequence coupling and positive sequence components, respectively, as reference.

Upon observing the normalized graphs, it is noticed that the symmetrical components accurately represent the system at low frequencies. However, for high frequencies, there is a significant discrepancy, particularly in terms of attenuation, which tends to be 2 p.u. in zero sequence, 0 p.u. in zero sequence coupling, and 4 p.u. in positive sequence from 10 kHz onwards.

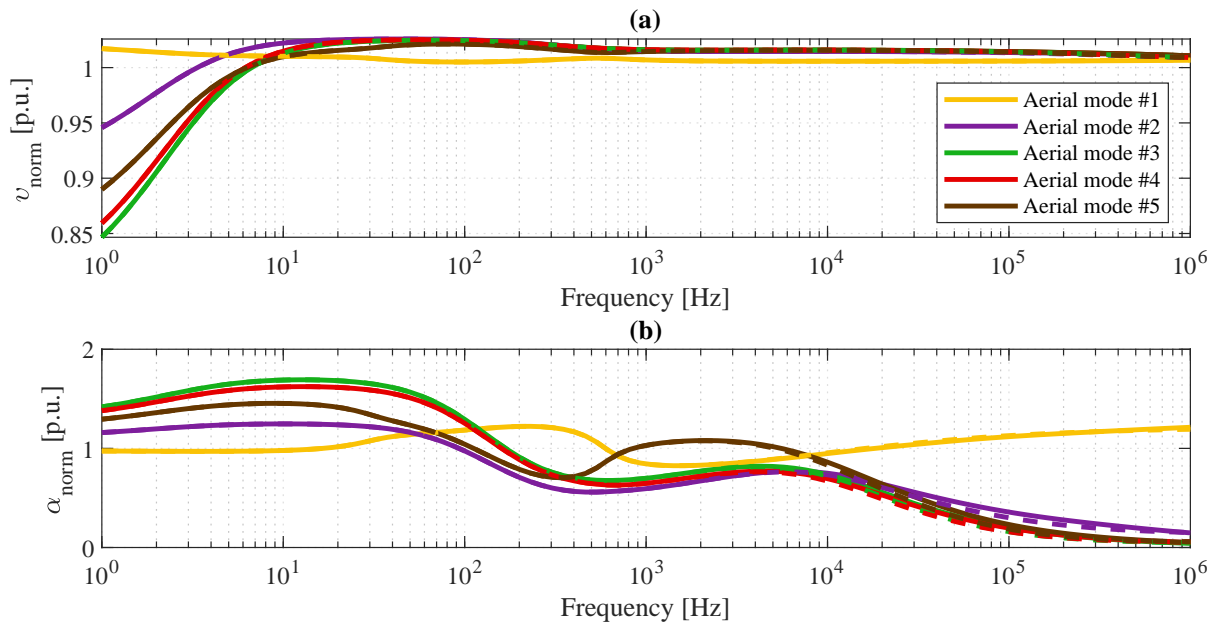
Regarding frequency-dependent soil properties, it is observed that only the phase velocity of ground-related modes is affected, starting from frequencies of 100 kHz. However, for all propagation modes, the attenuation constants are affected by the use of frequency-dependent soils at high frequencies (starting from 10 kHz). This spotlight the importance of employing such a model for high-frequency electromagnetic transient studies.

Figure 4.9. Ground mode normalized by zero sequence component (p_0) for: (a) phase velocity and (b) attenuation constant. Solid lines represent the CP soil models and dashed lines represent the FD soil models, both with $\rho = 1000 \text{ } \Omega\text{m}$ and $\varepsilon_{rg} = 3$.



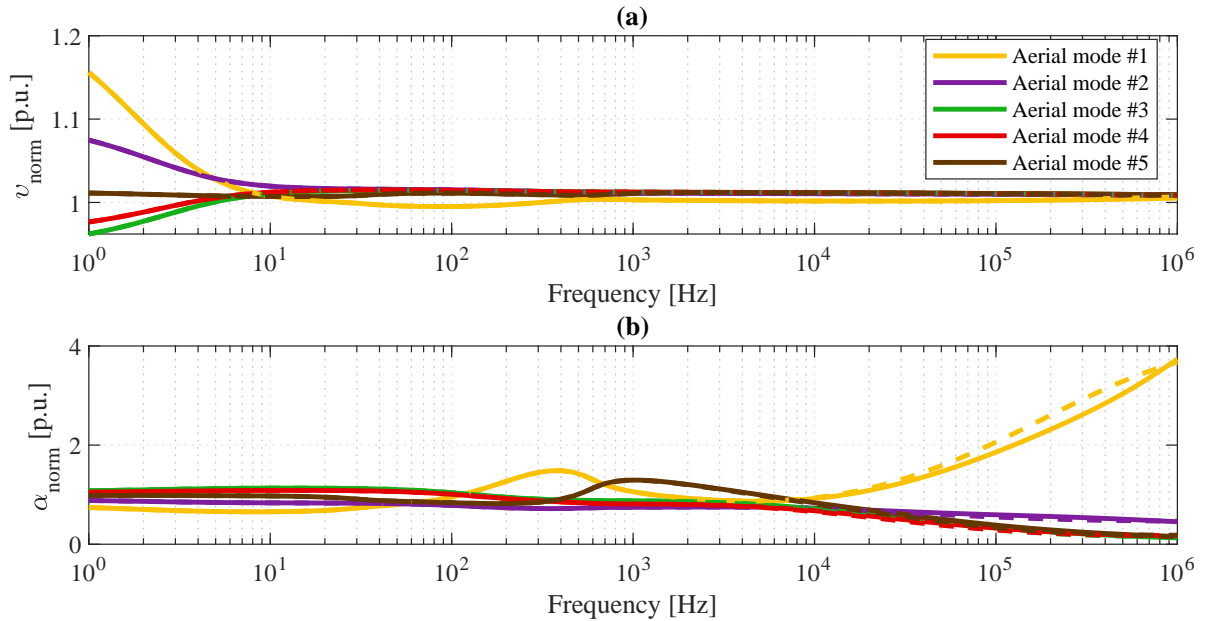
Source: Own authorship.

Figure 4.10. Aerial modes normalized by zero sequence coupling component (p_0^{I-II}) for: (a) phase velocity and (b) attenuation constant. Solid lines represent the CP soil models and dashed lines represent the FD soil models, both with $\rho = 1000 \text{ } \Omega\text{m}$ and $\varepsilon_{rg} = 3$.



Source: Own authorship.

Figure 4.11. Aerial modes normalized by positive sequence component (p_1) for: (a) phase velocity and (b) attenuation constant, comparing symmetrical domain and modal domain modes. Solid lines represent the CP soil models and dashed lines represent the FD soil models, both with $\rho = 1000 \Omega\text{m}$ and $\varepsilon_{rg} = 3$.



Source: Own authorship.

4.3.2 Complete System (Shield Wires Modeled Explicitly)

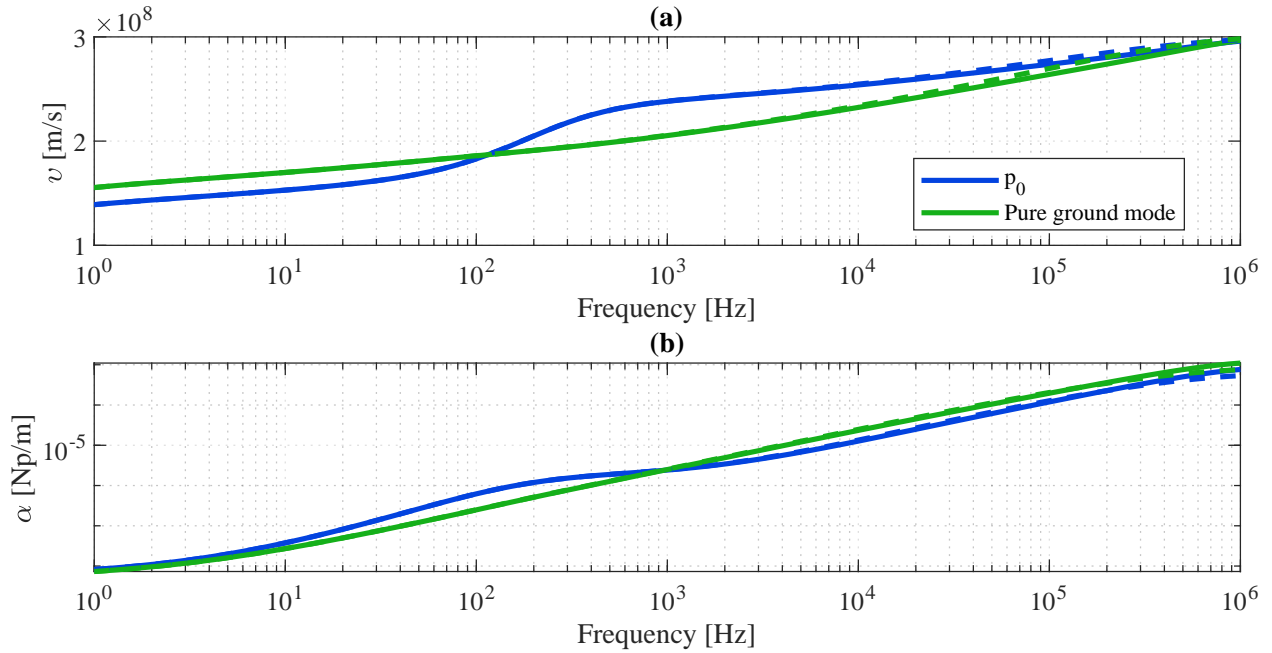
In the previous section, it is described that the symmetrical components: the zero sequence (p_0), the zero sequence coupling ($p_0^{\text{I-II}}$), and the positive sequence (p_1) accurately represent the modal propagation phenomena at low frequencies for a simplified system using Kron reduction. However, in a realistic system, there will be current induction in the shield wires caused by the currents flowing in the phase conductors. Therefore, despite the shield wires being grounded at each tower, an induced current will flow through these conductors, which renders the simplification by Kron reduction. However, using simplified Kron-reduced equivalent systems can lead to loss of relevant information in electromagnetic transient studies.

In the following section, a comparison is studied between the symmetrical components and the modal parameters considering an "explicit" mode for the shield wires. In other words, the shield wires are treated as a separate phase independent of the other phase conductors.

The purpose of this study is to highlight the discrepancies that arise from using the simplified

system assumption of no current flowing through the shield wires. The systems are assumed to be transposed using the 9ST method, and the soils considered have a resistivity of $1000 \Omega\text{m}$ and a relative permittivity of 3.

Figure 4.12. Ground modes propagation characteristics considering symmetrical components and modal parameter in a complete system (with "explicit" shield wires): (a) phase velocity, and (b) attenuation constant. Solid lines represent the CP soil models and dashed lines represent the FD soil models, both with $\rho = 1000 \Omega\text{m}$ and $\varepsilon_{rg} = 3$.



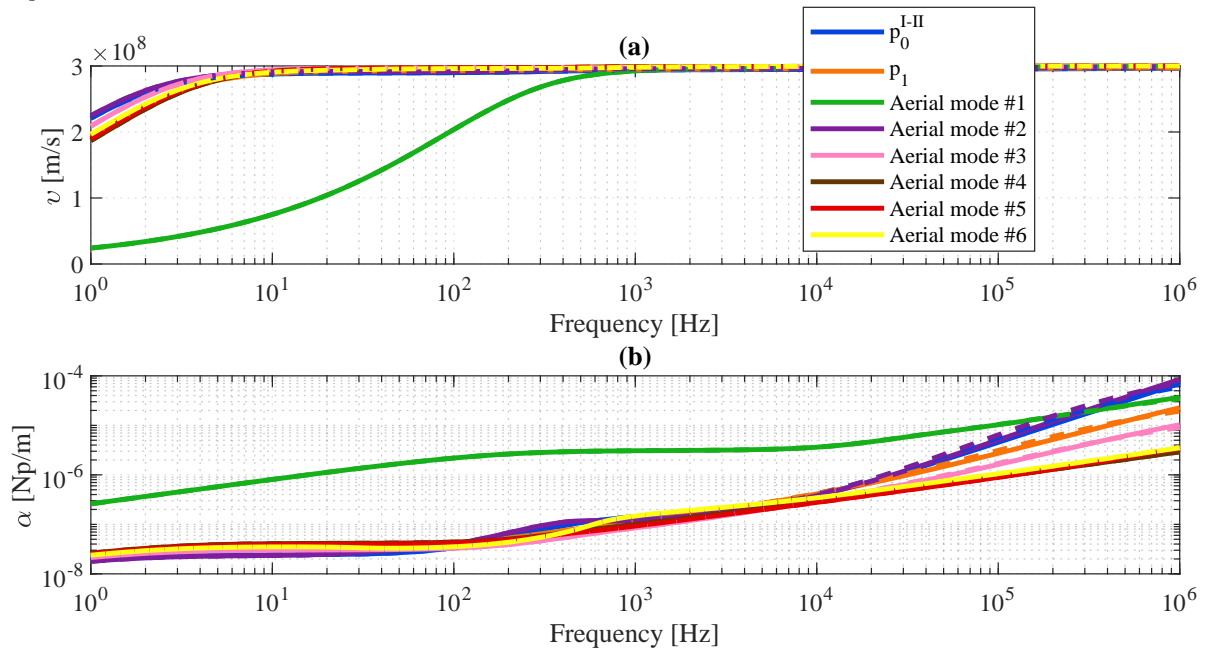
Source: Own authorship.

The propagation parameters of ground-related mode are presented in Figure 4.12. It is observed that the zero sequence components exhibits traces of propagation characteristics of overhead conductors when compared to the pure ground mode. This effect is caused by the inclusion of the shield wire characteristics during the Kron reduction process.

The propagation parameters of aerial modes are presented in Figure 4.12. It is noticed that the aerial mode #1 corresponds to the mode associated with the shield wires. Despite having similar attenuation and phase velocity characteristics as the other aerial modes, it exhibits higher attenuation throughout the frequency spectrum. Additionally, the aerial mode #1 phase velocity is significantly slower compared to the other modes due to the lower conductivity of the shield wires compared to the phase conductors.

To highlight the differences between the symmetric components approach and the modal-

Figure 4.13. Aerial modes propagation characteristics considering symmetrical components and modal parameters in a complete system (with "explicit" shield wires): (a) phase velocity, and (b) attenuation constant. Solid lines represent the CP soil models and dashed lines represent the FD soil models, both with $\rho = 1000 \Omega\text{m}$ and $\varepsilon_{rg} = 3$.



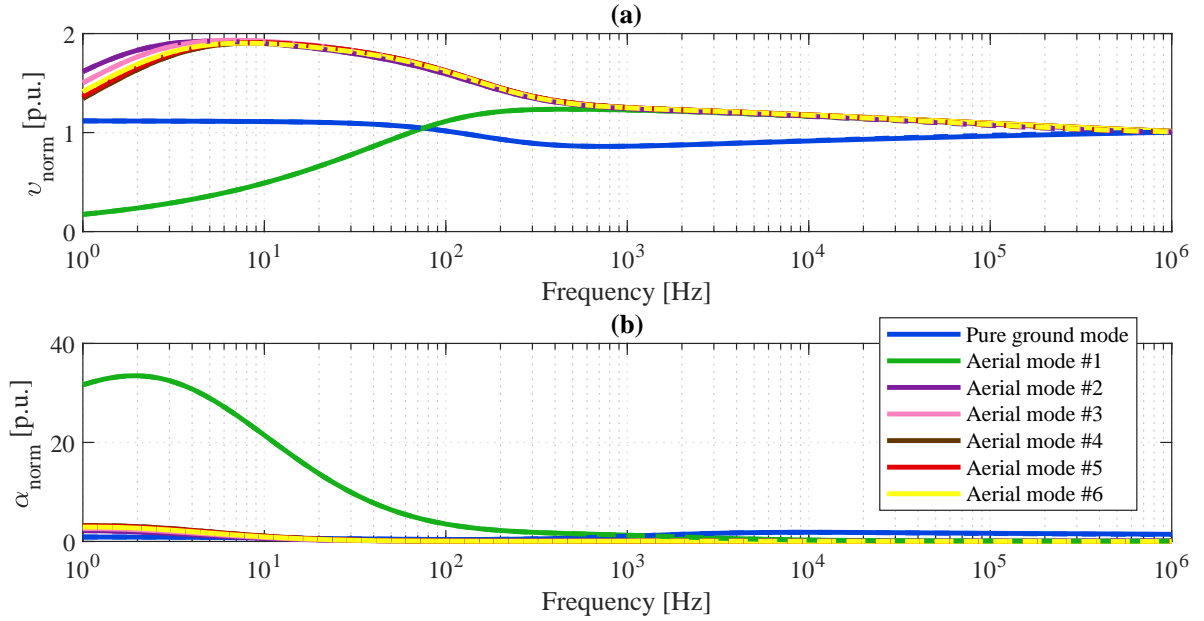
Source: Own authorship.

domain, normalized propagation parameters (p_{norm}), are provided as (4.1). The normalized modes by the zero sequence, zero sequence coupling, and the positive sequence are presented in Figures 4.14, 4.15 and 4.16, respectively.

From the normalized propagation parameters, it is verified that the propagation modes associated with the shield wires (Aerial mode #1) exhibit distinct characteristics compared to the three modes generated by the symmetric components (zero, zero coupling, and positive sequences). Although at high frequencies, Aerial mode #1 can be well represented by the zero sequence coupling and positive sequence, especially from 1 kHz onwards, the attenuation constant is significantly higher at low frequencies (approximately 62 and 55 p.u. for the inter-line and line modes, respectively). At high frequencies, the zero sequence coupling has twice the attenuation of the shield wire mode, while the symmetric line mode has half the attenuation.

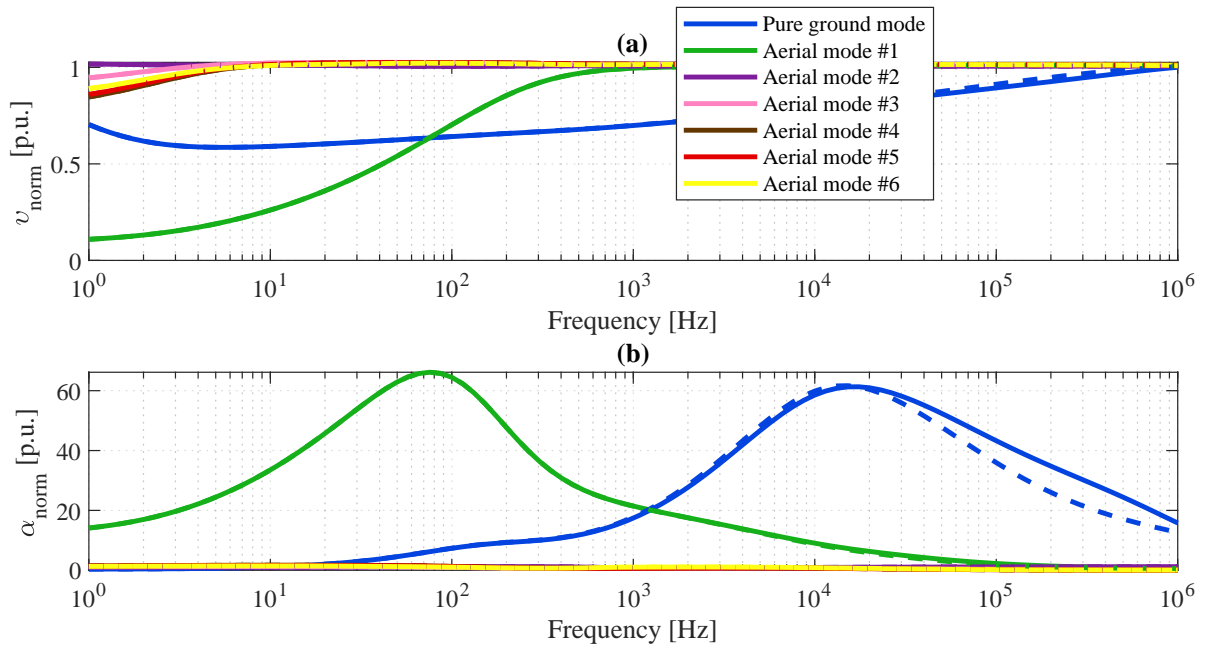
Therefore, it becomes evident that the wave propagation in the explicit shield wires is distinct, and the studies of all electrical phenomena throughout the frequency range are compromised when disregarding the current in the shield wires and, consequently, employing the Kron reduction.

Figure 4.14. Modal parameters propagation characteristics normalized by zero sequence component (p_0) considering a complete system (with "explicit" shield wires): (a) phase velocity and (b) attenuation constant, comparing symmetrical domain and modal domain modes. Solid lines represent the CP soil models and dashed lines represent the FD soil models, both with $\rho = 1000 \Omega\text{m}$ and $\varepsilon_{rg} = 3$.



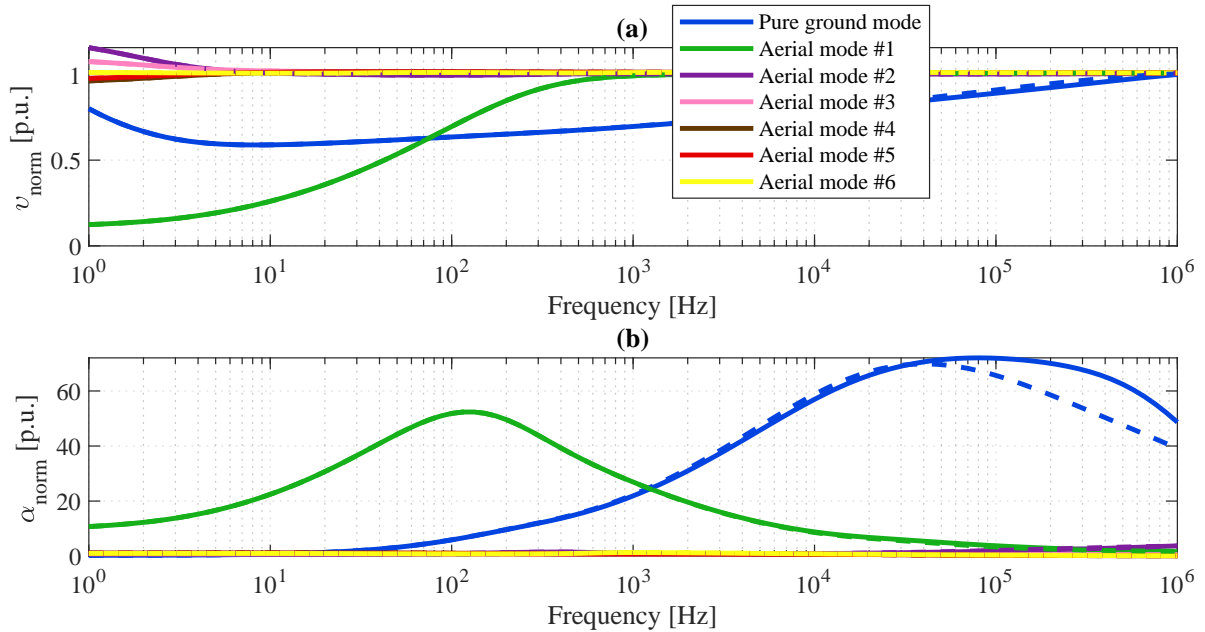
Source: Own authorship.

Figure 4.15. Modal parameters propagation characteristics normalized by zero sequence coupling component (p_0^{I-II}) considering a complete system (with "explicit" shield wires): (a) phase velocity and (b) attenuation constant, comparing symmetrical domain and modal domain modes. Solid lines represent the CP soil models and dashed lines represent the FD soil models, both with $\rho = 1000 \Omega\text{m}$ and $\varepsilon_{rg} = 3$.



Source: Own authorship.

Figure 4.16. Modal parameters propagation characteristics normalized by positive sequence component (p_1) considering a complete system (with "explicit" shield wires): (a) phase velocity and (b) attenuation constant, comparing symmetrical domain and modal domain modes. Solid lines represent the CP soil models and dashed lines represent the FD soil models, both with $\rho = 1000 \Omega\text{m}$ and $\varepsilon_{rg} = 3$.



Source: Own authorship.

4.4 CHAPTER SUMMARY

This chapter focuses on analyzing the propagation parameters in a double-circuit transmission line. Three main parameters are investigated: variations in soil properties (resistivity and relative permittivity), suitable transposition methods for double-circuit lines, and a comparison of modal parameters between a system using Kron reduction and a system considering the use of "explicit" shield wires.

In the analysis of soil influences on modal parameters, three types of soil properties are considered: low resistivity and relative permittivity, medium resistivity and relative permittivity, and high resistivity and relative permittivity. Both constant-frequency (CP) and frequency-dependent (FD) soil models are examined. The zero sequence and zero sequence coupling components are found to be the most affected by changes in soil properties, while the positive sequence is less affected. The most conductive soil exhibits higher phase velocities and lower attenuations, and the FD soil models show lower attenuations and higher phase velocities at

high frequencies.

The influence of transposition schemes on modal parameters is also investigated. Three transposition methods are compared: the nine-section transposition (9ST-SD), three-section transposition with phase rotation in the same direction (3ST-SD), and three-section transposition with phase rotation in the opposite direction (3ST-OD). It is observed that the propagation parameters remain the same regardless of the transposition scheme adopted, indicating that the symmetric components do not accurately represent the physical phenomena in the transmission line.

Furthermore, a comparison is performed between the symmetric components and the modal-domain, both using Kron reduction. The results show that the zero sequence component has the same phase velocity as the ground mode from the modal-domain, but there are differences in attenuation at high frequencies. The aerial modes exhibit similarities between the two domains, but there are also discrepancies in attenuation at high frequencies. Normalized propagation parameters demonstrate that the symmetric components accurately represent the system simplified with Kron reduction at low frequencies, but significant discrepancies arise at high frequencies.

Lastly, the inclusion of shield wires in the system is considered. In a realistic system, shield wires induce currents caused by the phase conductors. The analysis highlights the importance of considering the shield wire due to the singular propagation parameters, mainly the attenuation constant, that cannot be represented with symmetric components or modal-domain using Kron simplification.

Based on the results of the theoretical studies conducted in this chapter, it is evident that both the propagation parameters for the symmetric components and the modal parameters exhibit behaviors that vary with soil properties and the modeling of shield wires. Considering that soil properties vary along the right-of-way, the most realistic model to represent the transmission line is discriminate the geometric and physical parameters from span to span, which is the model used in this work to implement the transmission system. Furthermore, the most realistic model should explicitly consider the modeling of shield wires, as neglecting these elements can result in the loss of crucial information in electromagnetic transient studies. Regarding transposition, according to the findings of this chapter, it appears that it does not have any

influence on electromagnetic transient studies.

In the next chapter, a comprehensive study on short circuits in the 500 kV Silves-Oriximiná transmission line will be presented, focusing on the soil, transposition scheme, and influence of shield wires. The analysis includes various scenarios to evaluate their impact on short-circuit levels, fault currents, and contributions from substations.

TRANSIENT FAULT STUDY

5.1 GENERAL STUDY DESCRIPTION

In this chapter, various scenarios of short circuits occurring in the 500 kV Silves-Oriximiná transmission line are performed. The analysis focuses on three major aspects: 1) soil properties, 2) the transposition scheme, and 3) the influence of shield wires.

Each parameter is evaluated through different scenarios to assess their impact on short-circuit levels in the transmission line. This includes analyzing fault currents in the faulted branch and the contribution of substations to a faulted circuit of the transmission line.

To conduct the analysis, faults are applied at regular intervals of approximately 3.3 km (1% of the total transmission line length) for each scenario, which results in a total of 100 faults per scenario. Overall, 1500 short-circuit cases are analyzed in a wide range of scenarios along the transmission line.

Phase-to-ground faults are applied along circuit 1 of the transmission line. Circuit 2 remains under nominal conditions. A fault resistance (R_f) of 0.001 Ω is used to represent bolted short-circuit conditions, which evaluate the worst-case scenario for short-circuits in the transmission line.

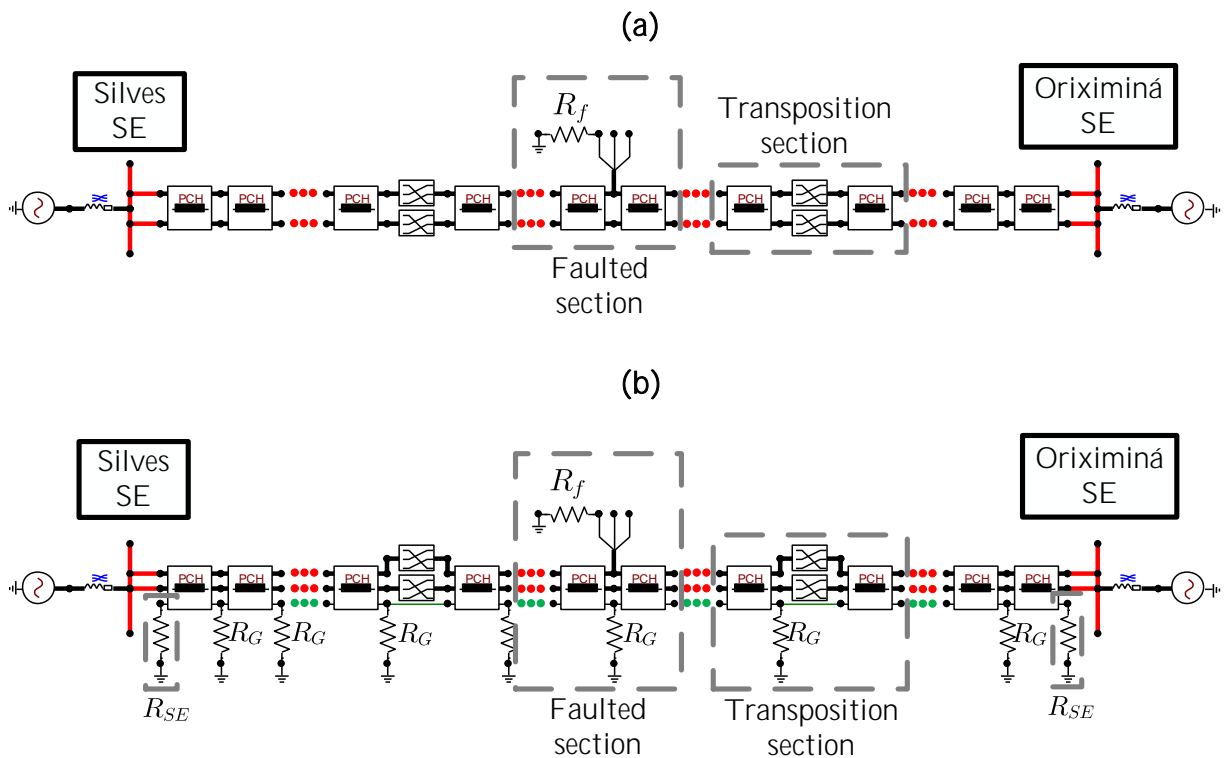
Single-phase faults are the most common type of fault in a transmission system, accounting for approximately 70 to 80% of all fault cases (NITHYAVELAM; HENRY, 2018). Furthermore, if all parameters under analysis are directly or indirectly associated with the earth, then faults involving the ground tend to be more affected by variations in these parameters. Therefore, only phase-to-ground faults are considered in this work without the loss of generality of the results.

5.2 EMTP/ATP CIRCUIT MODEL FOR THE TRANSIENT STUDY

For each span of the transmission line, the cell shown in Figure 3.8 is employed. The transmission line is formed by cascading the 596 spans along with their respective parameters. A simplified representation in ATPDraw is presented for didactic purposes; however, constructing a complex and lengthy system demands considerable time. Therefore, a computational routine was developed to generate all the punch files and assemble the main ATP cards.

Figure 5.1-(a) and 5.1-(b) present the simplified circuits used for phase-to-ground fault simulations using Kron simplification and with the shield wires (CPR) explicit, respectively.

Figure 5.1. EMTP/ATP simplified model representation for single-phase faults for (a) simplified model using Kron reduction, and (b) model with explicit shield wires. $R_G = 15 \Omega$ is the tower grounding resistance, $R_f = 0.001 \Omega$ is the fault resistance and $R_{SE} = 1 \Omega$ is the substation grounding resistance.



Source: Own authorship.

5.3 INFLUENCE OF SOIL PROPERTIES ON FAULT STUDY

To assess the influence of soil modeling and its parameters, five scenarios are considered based on real resistivity measurements obtained along the right-of-way:

1. minimum resistivity ($\rho = 40 \text{ } \Omega\text{m}$, $\varepsilon_{rg} = 1$);
2. common value considered in TL projects ($\rho = 1000 \text{ } \Omega\text{m}$, $\varepsilon_{rg} = 3$);
3. average resistivity ($\rho = 4324 \text{ } \Omega\text{m}$, $\varepsilon_{rg} = 3$);
4. maximum resistivity ($\rho = 13832 \text{ } \Omega\text{m}$, $\varepsilon_{rg} = 5$);
5. longitudinal heterogeneous resistivity along the transmission line extension.

The minimum, average, and maximum resistivities are derived from the deep-layer values of the multilayered models calculated from the field measurements of the transmission line (see Table 3.2).

The resistivity of 1000 ohms is included as a commonly used and regard as a conservative value for soil resistivity in transmission line modeling, particularly in transmission line constructive projects.

Finally, the heterogeneous resistivity model represents the most realistic case. In this model, the resistivity varies for each span of the transmission line according to the field values presented in Figure 3.7. Additionally, the electric permittivity values of the soil follow the pattern presented in Table 3.3, also varying for each span depending on the respective soil resistivity.

For the five soil models presented, two scenarios are considered: constant parameters (CP) and frequency-dependent parameters (FD).

In the CP scenarios, the soil properties remain constant across the entire frequency range of interest. This assumes that the resistivity and permittivity of the soil do not vary with frequency.

In the FD parameter scenario, the soil properties vary with frequency. This acknowledges that the resistivity and permittivity of the soil exhibit frequency-dependent behavior. This

scenario allows a more accurate representation of the soil's electrical characteristics at different frequencies.

Considering CP and FD soil in all scenarios, the study aims to assess the impact of frequency dependence in the soil properties on the behavior of the transmission line and its response to short-circuit events.

All soil models employ the same transmission line modeling to solely investigate the influence of soil properties on short circuits. Thus, in all models, the transmission line is modeled using a nine-section transposition scheme with the circuits rotated in the same direction (9ST-SD), as depicted in Figure 2.5, and Kron reduction is utilized. This transposition scheme is chosen as the standard due to its minimal coupling between the two circuits of the transmission line.

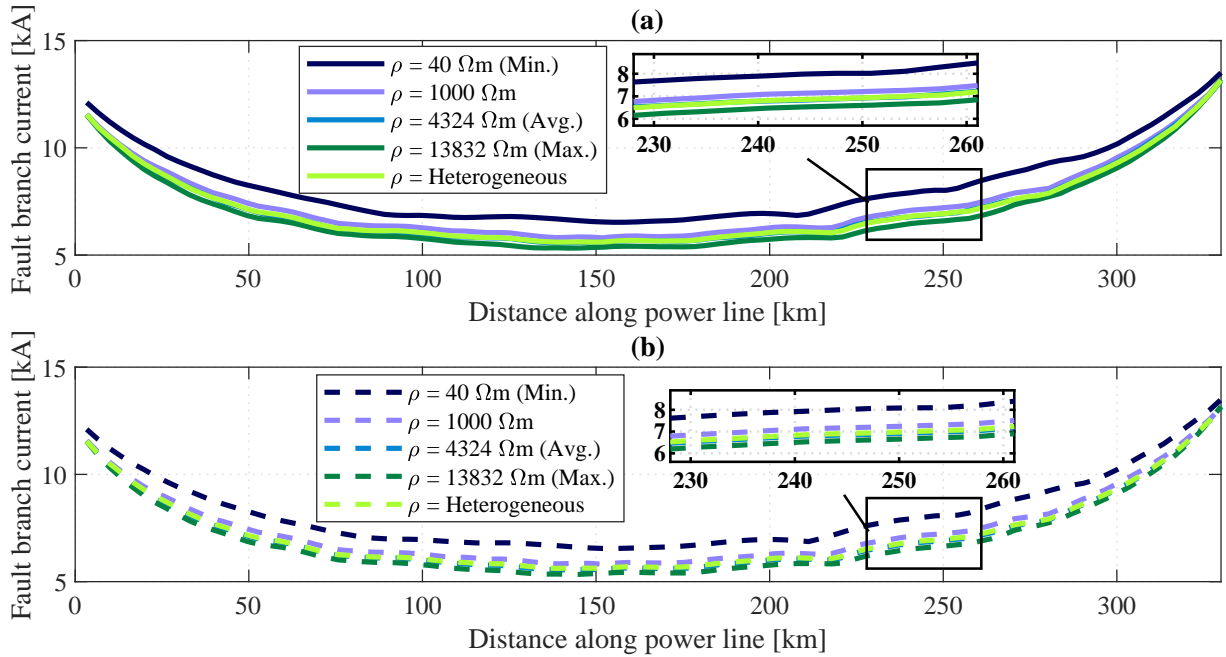
According to the theoretical studies on propagation parameters in Section 4.1, it is expected that soil resistivity significantly impact electromagnetic transients involving the ground, such as single-phase faults. Since the phase velocity and attenuation constant of the ground mode (or zero sequence) are affected by changes in soil resistivity (see Figures 4.1, 4.2, and 4.3). As for the variation of soil properties with frequency, there is only a discrepancy at high frequencies. Therefore, in the fault studies presented below, it is expected that the variant and constant-frequency soil parameters will have similar values, as the electromagnetic transients applied to the transmission line are not of high frequency.

5.3.1 Fault Branch Currents

Figure 5.2 presents the maximum fault branch current values for single-phase faults applied at each 1% of the transmission line for all the soil models considered. Figure 5.2-(a) shows the fault current values for the constant parameter soil models, while Figure 5.2-(b) presents the fault current values for the frequency-dependent parameter soil models.

Figure 5.2 shows that there is a small variation (less than 10%) between the frequency-dependent and frequency-invariant soil models. This is due to the fact that short circuits are not high-frequency electromagnetic transients. In the frequency ranges of short circuits, then, only a small difference in the modal parameters of the transmission line is observed between these models (see Figure 4.1). Although the difference between the frequency-dependent and

Figure 5.2. Maximum fault branch current under single-phase fault conditions along the transmission line, considering: (a) constant parameters (CP) soil models, and (b) frequency-dependent (FD) soil models.



Source: Own authorship.

frequency-invariant soil models seems to be insignificant, the absolute value of the branch fault currents is high and the 10% discrepancy between the models represents approximately 1.2 kA, which is a considerable difference in current. Moreover, if high-frequency EMTs are analyzed, such as atmospheric discharges, the difference between the models will be more significant.

It is evident that in all soil models, the fault current increases as the fault approaches the substations, due to the contribution of current from the sources at the terminals.

Regarding the variation in soil resistivity models, it is observed that considering the minimum and maximum values of resistivity measured, the system will be over-dimensioned and under-dimensioned, respectively. To quantitatively assess the discrepancy between the models, the normalized current between the scenarios is provided as follows:

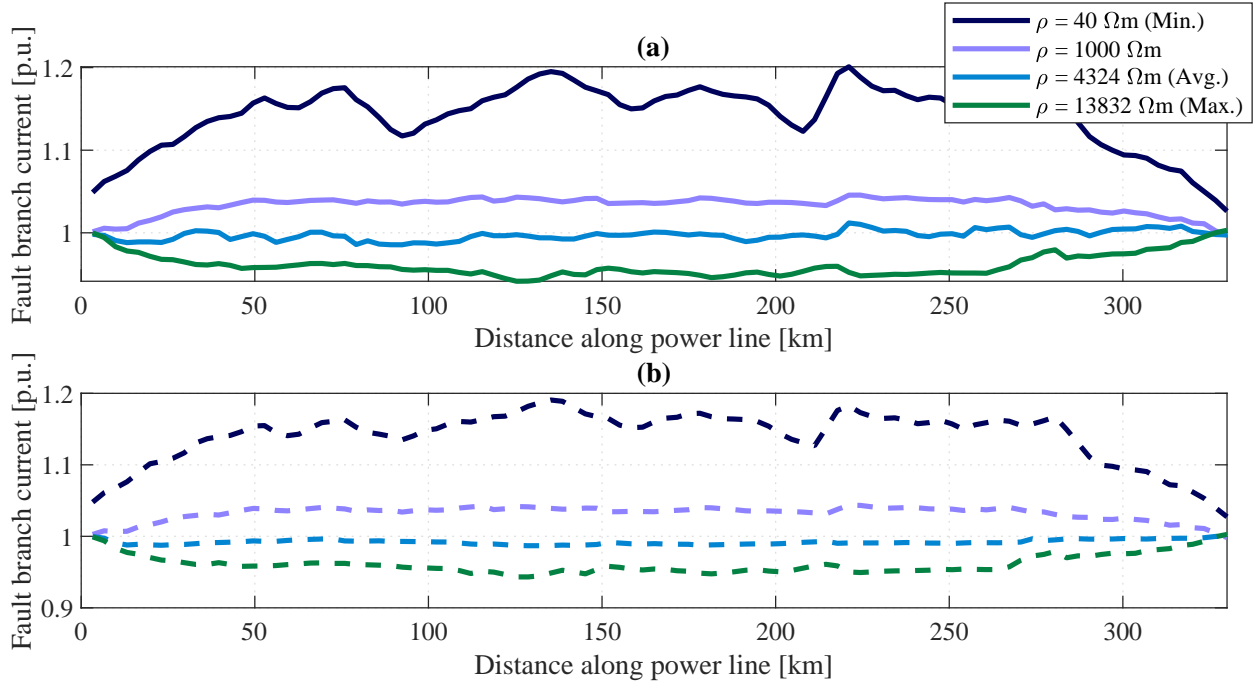
$$I_{norm} = \frac{\text{Current values of the models}}{\text{Current values of a reference model}} \quad (5.1)$$

In this case, the heterogeneous soil is considered as a reference.

Figure 5.3 presents the fault branch current difference for all models considering (a) CP soil

models, and (b) FD soil models. Table 5.4 summarizes the average of the normalized current for the fault branch currents in the different soil models.

Figure 5.3. Normalized fault branch current under single-phase fault conditions along the transmission line, considering: (a) constant parameters (CP) soil models, and (b) frequency-dependent (FD) soil models.



Source: Own authorship.

It is verified that with the minimum soil properties, the fault branch current is overestimated by an average of 1.14 p.u. (1 kA) compared to the heterogeneous model. This is due to the fact that the soil, in this case, is more conductive, and in the event of a fault involving the earth, more current flows through the fault branch into the earth.

In the case of the soil with the maximum resistivity observed in the field measurements, the opposite phenomenon occurs. Considering the maximum soil properties, the average fault current is underestimated by 4% (≈ 260 A), according to Table 5.1.

Considering the parameters as $\rho = 1000 \Omega\text{m}$ and $\varepsilon_{rg} = 3$, the fault branch current corresponds, on average, to 1.033 p.u. of the fault current in the heterogeneous case, for both FD and CP soil models.

Finally, considering the average value of the deep-layer resistivity provides the best approximation for modeling with only a single constant soil resistivity value considered throughout the transmission line. With these parameters, a discrepancy of 37.3 A and 55.08 A is observed

Table 5.1. Outline of average discrepancy on fault branch current between the soil models in relation to heterogeneous soil model.

Soil models	Average of I_{norm}		Average of I_{norm}	
	CP	FD	CP	FD
$\rho = 40 \Omega\text{m}$ (Min.)	978.41 A	962.83 A	1.143 p.u.	1.141 p.u.
$\rho = 1000 \Omega\text{m}$	222.48 A	261.95 A	1.033 p.u.	1.032 p.u.
$\rho = 4324 \Omega\text{m}$ (Avg.)	37.3 A	55.08 A	0.997 p.u.	0.992 p.u.
$\rho = 13832 \Omega\text{m}$ (Max.)	261.95	259.96 A	0.961 p.u.	0.961 p.u.

Source: Own authorship.

for FD and CP models, respectively. This discrepancy represents less than a 1% difference based on the more realistic model, which is consistent with studies found in the literature (MARTINS-BRITTO *et al.*, 2020).

5.3.2 Substation Contribution Currents

The maximum absolute values of the faulted phase currents (Phase A of Circuit 1) measured on the Silves and Oriximiná substations, considering constant soil properties, are shown in Figure 5.4. The same currents, considering FD soils, are presented in Figure 5.5.

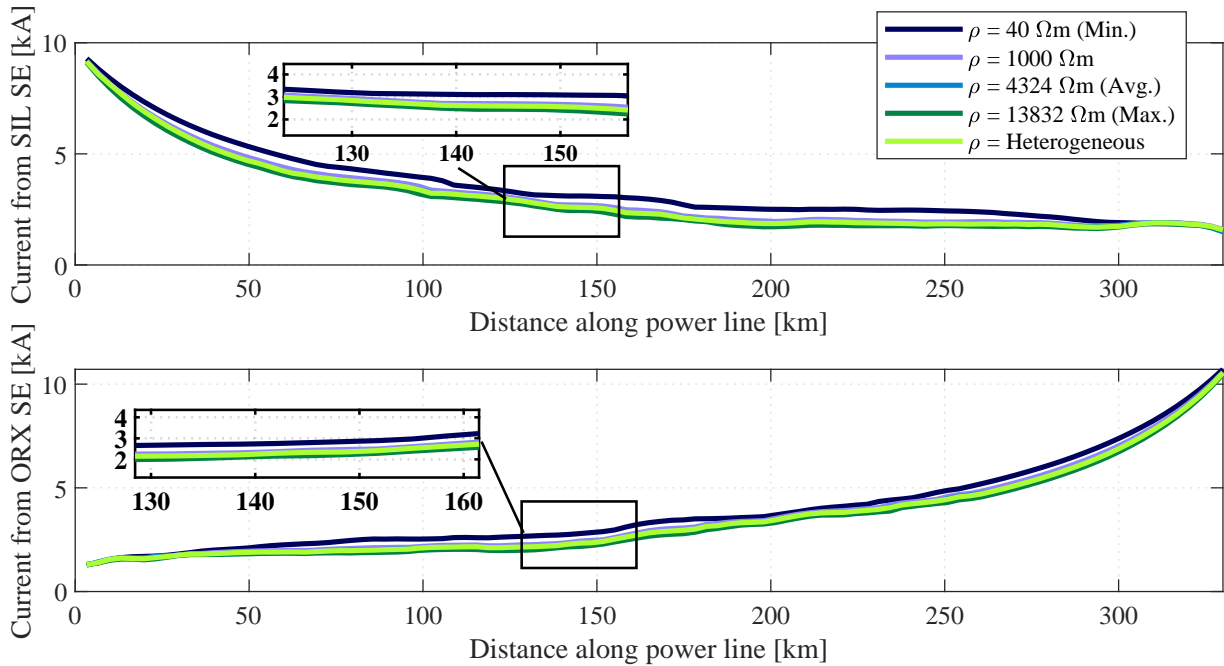
Similar to the fault branch currents, soil models with FD soil properties do not significantly influence the results of the substation contribution currents compared to constant soil models (observe the zoom box in Figure 5.4 and 5.5), due to the low-frequency range of the analyzed transients (between 1 and 200 kHz).

It is noted from the measured currents at the Silves and Oriximiná substations that the influence of the impedance as seen from the terminals can be observed. As the fault location is moved away from the terminal, the equivalent impedance seen from the terminal increases, which decreases the contribution current from the terminal.

The normalized values of the contribution currents from both substations are shown in (5.1).

Similarly to previous analyses, the system with heterogeneous soil along the transmission line is considered the most realistic and serves as the reference. The differences in contribution currents for the faulted circuit and the healthy circuit, considering frequency-dependent soils, are presented in Figure 5.6. As the frequency-dependent models exhibit insignificant discrepan-

Figure 5.4. Maximum value of contribution currents from Silves and Oriximiná substations measured on the faulted circuit under phase-to-ground fault conditions along the transmission line. Soils are considered invariant-frequency (CP) models.



Source: Own authorship.

cies compared to the frequency-independent models, the other graph will be omitted for the sake of brevity. Tables 5.2 and 5.3 summarize the average of the discrepancy of the CD and FD soil models respectively.

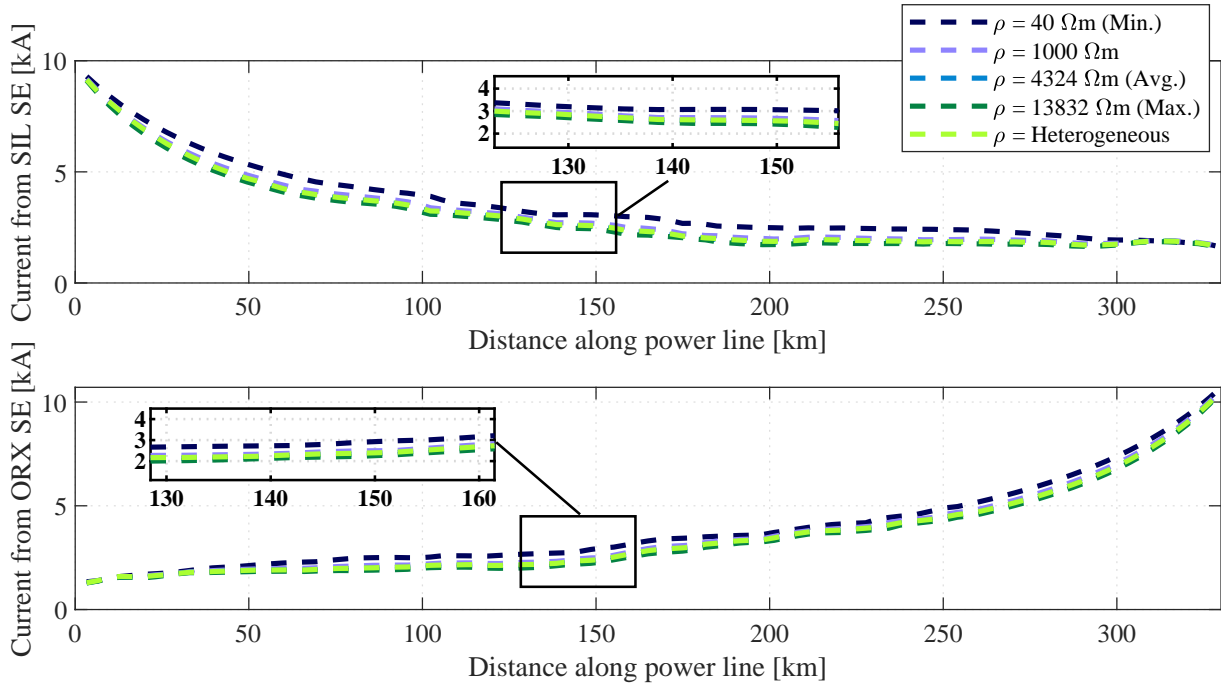
Table 5.2. Outline of average discrepancy on substations contribution currents for the different CP soil models.

Soil models	Avg. of I_{norm}		Avg. of I_{norm}	
	Silves SE		Oriximiná SE	
$\rho = 40 \Omega m$ (Min.)	1.18 p.u.	466.96 A	1.12 p.u.	365.20 A
$\rho = 1000 \Omega m$	1.03 p.u.	95.06 A	1.03 p.u.	86.28 A
$\rho = 4324 \Omega m$ (Avg.)	0.99 p.u.	26.61 A	0.99 p.u.	20.73 A
$\rho = 13832 \Omega m$ (Max.)	0.95 p.u.	126.03 A	0.96 p.u.	111.93 A

Source: Own authorship.

It is observed that the contribution currents are sensitive to changes in soil properties. For the minimum resistivity, it is noticed that in the regions where the soil resistivity increased in the right-of-way highest discrepancies are encountered, reaching up to 1.3 p.u. at the Silves substation and 1.25 p.u. at the Oriximiná substation.

Figure 5.5. Maximum value of contribution currents from Silves and Oriximiná substations measured on the faulted circuit under phase-to-ground fault conditions along the transmission line. Soils are considered frequency-dependent (FD) models.



Source: Own authorship.

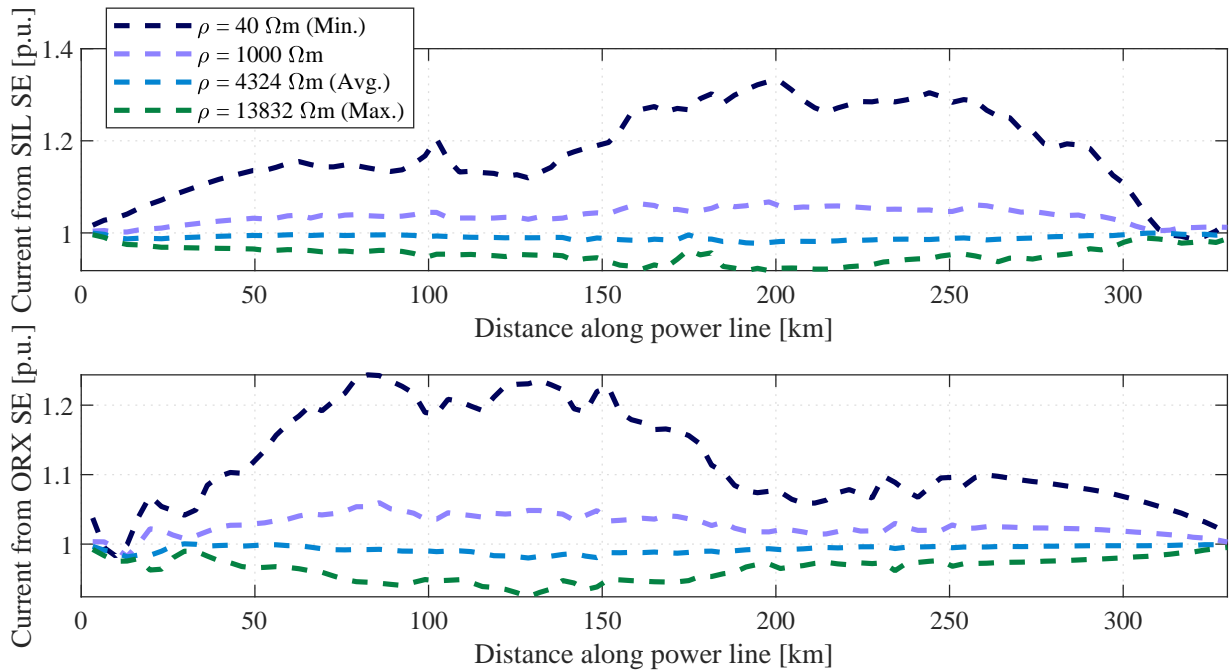
The contribution currents from the substations are overestimated using low resistivity values and underestimated using high resistivity values. For $\rho = 40 \Omega\text{m}$, the Silves substation is overestimated by an average of 466.96 A and 455.37 A, considering CP and FD soils, respectively. In the Oriximiná substation, on average, for CP and FD soils, the system experiences current rises of 365.20 A and 356.09 A, respectively.

With the maximum resistivity value, the contribution currents are underestimated by 126.06 A and 111.93 A for the Silves and Oriximiná substations, respectively, for frequency-invariant soils. For FD soils, the contribution currents from the substations are 127.15 A and 107.69 A.

Considering a resistivity of 1000 ohms, a discrepancy of less than 3% is obtained for the heterogeneous model, which represents a conservative model with an approximate difference of 90 A for both substations, considering FD and CP soils.

Once again, the model considering the average of deep-layer resistivity is the one that best fits the heterogeneous case using constant parameters along the entire transmission line. The discrepancy between this model and the most realistic is only 1% (25 A). It is reasonable to

Figure 5.6. Normalized contribution currents from Silves and Oriximiná substations measured on circuit 1 phase A (faulted circuit) in phase-to-ground fault conditions along the transmission line. The model with longitudinal heterogeneous soil is considered as reference and have frequency-dependent (FD) properties.



Source: Own authorship.

consider that these models yield equivalent results.

An interesting point to observe is that the Oriximiná substation is the main contributor to current injection into the transmission line. As this is the strongest source at the terminal ends of the transmission line, it is verified that this substation is less susceptible to variations in soil models. On the other hand, the Silves substation as a "weaker" source, exhibits larger discrepancies observed for different resistivity and permittivity values of the soil.

Table 5.3. Outline of average discrepancy on substations contribution currents for the different FD soil models.

Soil models	Avg. of I_{norm}	
	Silves SE	Oriximiná SE
$\rho = 40 \Omega\text{m}$ (Min.)	1.18 p.u. 455.37 A	1.12 p.u. 356.09 A
$\rho = 1000 \Omega\text{m}$	1.03 p.u. 97.16 A	1.03 p.u. 84.04 A
$\rho = 4324 \Omega\text{m}$ (Avg.)	0.99 p.u. 28.29 A	0.99 p.u. 20.26 A
$\rho = 13832 \Omega\text{m}$ (Max.)	0.95 p.u. 127.15 A	0.96 p.u. 107.69 A

Source: Own authorship.

5.4 INFLUENCE OF CONDUCTOR TRANSPOSITION ON FAULT STUDY

To analyze the influence of transposition schemes on short-circuit currents in double-circuit transmission lines, five transposition scenarios are considered:

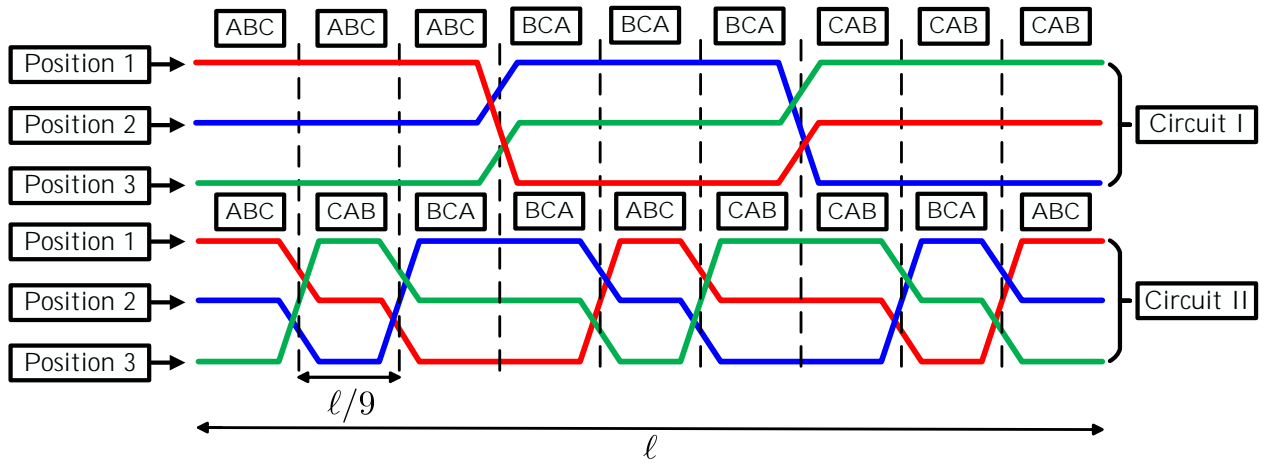
1. three-section transposition scheme with the barrels rotated in the same direction (3ST-SD), as presented in Figure 2.7;
2. three-section transposition with the barrels rotated in opposite direction (3ST-OD), as shown in Figure 2.6;
3. nine-section transposition scheme with the barrels rotated in the same direction (9ST-SD), presented in Figure 2.5;
4. proposed a new transposition scheme with 9 sections, rotating the phases of the circuits in opposite directions (9ST-OD);
5. real transposition of the transmission line, shown in Figure 3.5.

Due to the constructional aspects of the phase conductors in the transmission line tower, for a triangular phase arrangement, transposition types that involve phase rotation in opposite directions can be more advantageous for the system. This is because in these transposition types, phase conductors with the same magnitude and angle in both circuits never come close to each other, reducing the resulting electromagnetic field of the system. Furthermore, it is known that the nine-section transposition is the type of transposition that results in minimal coupling between the circuits of the transmission line. Therefore, a new transposition model is proposed, considering nine sections but rotating the circuits in opposite directions, as presented in 5.7.

In all these transposition scenarios, the transmission line is modeled considering the Kron simplification. Therefore, all the analyzed fault scenarios are constructed as shown in Figure 5.1-(a).

In this section, the transposition schemes are evaluated considering frequency-dependent soil properties only, as the previous section showed no significant differences in short-circuit currents

Figure 5.7. Proposed nine-section transposition scheme for double-circuit transmission line, with the barrels rotated in opposite direction.



Source: Own authorship.

between models considering frequency-dependent and frequency-invariant soil properties. This choice is made because FD parameters represent better electrical earth phenomena.

The theoretical studies presented in Section 4.2 have shown that there is no change in propagation parameters for the types of transposition considered. Therefore, it is expected that there will be no change in the electromagnetic transients when only the conductor transposition is varied.

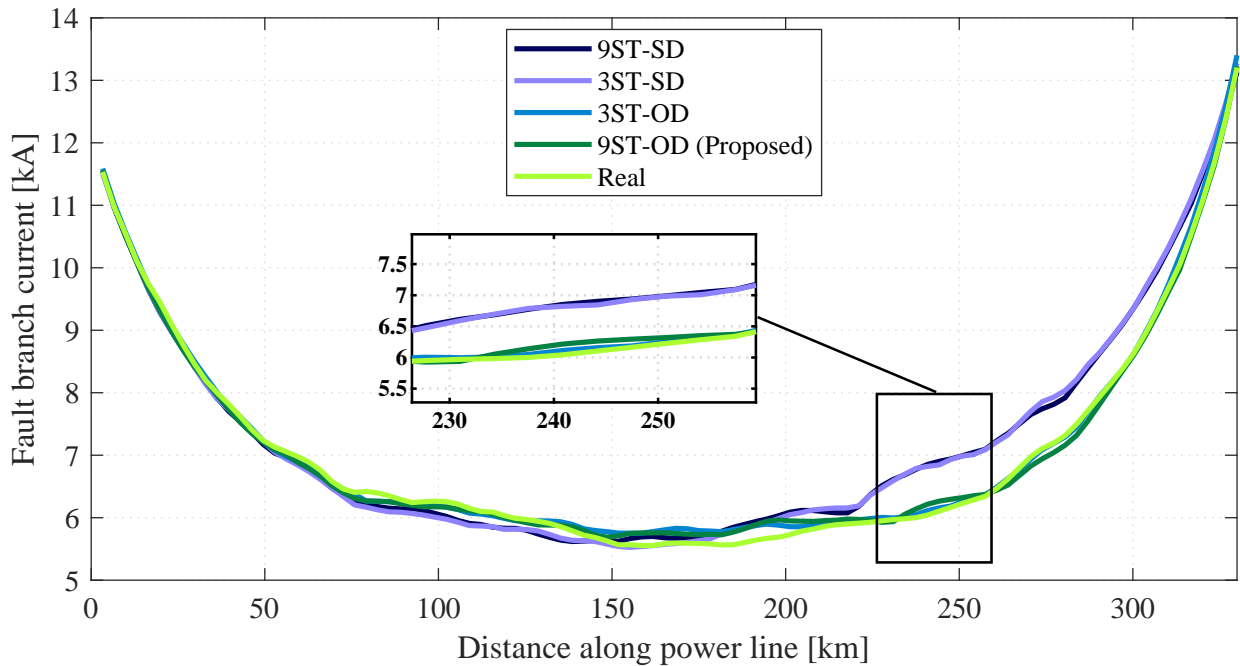
5.4.1 Faulted Branch Currents

The maximum absolute values of the fault branch currents for each transposition scenario for the faults applied along the transmission line are presented in Figure 5.8.

It is observed that for this transmission line, the transposition schemes that rotate the circuits in opposite directions have better performance in terms of fault currents, especially in the latter portion of the transmission line (from 200 km onwards).

It is noted that the circuits rotated in the same direction present always two equal phases in the transmission line that are closer, resulting in a stronger resultant electromagnetic field and higher fault current. The observation of this phenomenon primarily occurs in the last third of the transmission line because the fault phase (phase A of the circuit) becomes closer to phase

Figure 5.8. Maximum absolute value of fault branch current under a single-phase fault (Ag) condition, considering all types of transposition schemes. Soils are considered frequency-dependent (FD) models and longitudinal heterogeneous along the right-of-way, as presented in Figure 3.7.



Source: Own authorship.

A of circuit 2 (which has the same angle) in that region.

The real transposition of the transmission line rotates the phases of the circuits in the opposite direction, which results in lower current values in the fault branch in the last third of the transmission line as well.

Using the equation in (5.1), but taking the real line transposition as a reference, the normalized fault branch currents under single-phase fault conditions are presented in Figure 5.9.

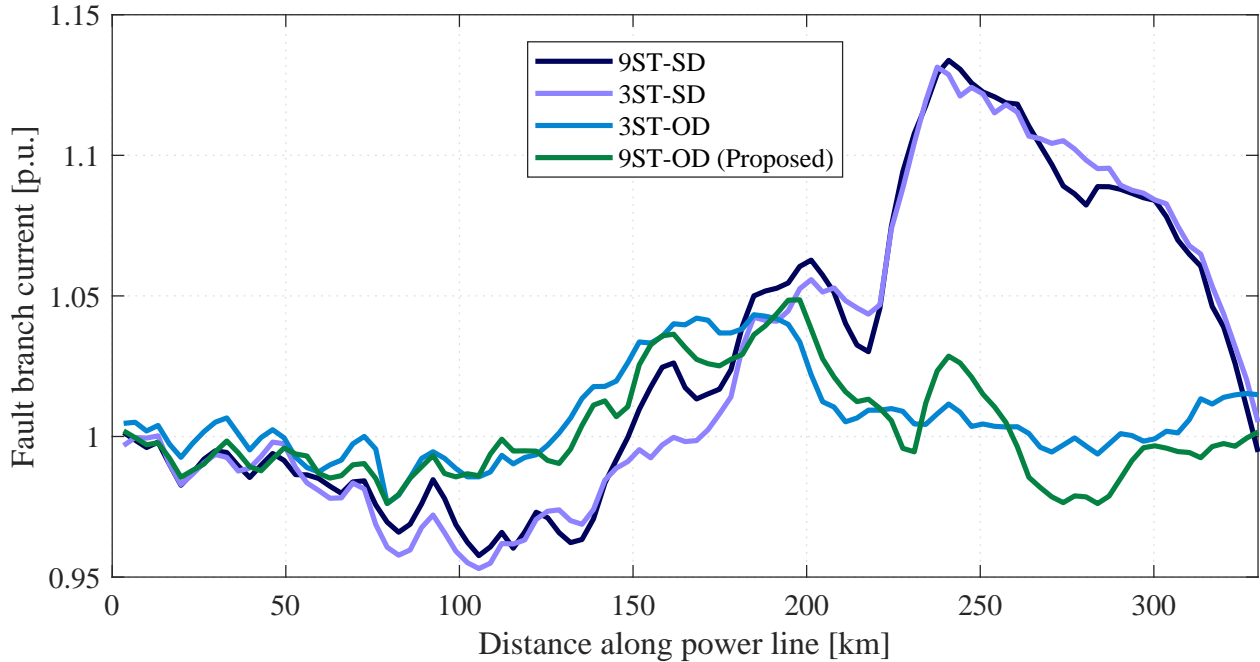
Table 5.4. Outline of average discrepancy on fault branch current between the transposition schemes in relation to the real transposition scheme.

Transposition schemes	Average of I_{norm}	Average of I_{norm}
9ST-SD	193.08 A	1.03 p.u.
3ST-SD	186.60 A	1.03 p.u.
3ST-OD	43.01 A	1.01 p.u.
9ST-OD (Proposed)	4.86 A	1.00 p.u.

Source: Own authorship.

Table 5.4 presents the average discrepancies between the types of transposition and the real

Figure 5.9. Normalized fault branch current under a single-phase fault (Ag) condition, considering all types of transposition scheme. The real transposition of the 500 kV double-circuit Silves-Oriximiná transmission line is used as a reference (see Figure 3.5). Soils are considered frequency-dependent (FD) models and longitudinal heterogeneous along the right-of-way, as presented in Figure 3.7.



Source: Own authorship.

line transposition, in amperes and per unit. Based on the data presented in Table 5.4, it is confirmed that, on average, the transpositions that rotate the circuits in the same direction, due to the constructive aspects of the phases in the tower geometry, have a higher resultant magnetic field and therefore exhibit a discrepancy of 3% compared to the real transposition, which represents approximately 190 A.

Another important point is that the 9ST-OD and 3ST-OD transposition schemes have smoother variations in the currents in the branch due to a better balance of phases between the two circuits along the right-of-way.

Furthermore, it is verified that the proposed model (9ST-OD) is the closest to the real transposition, with the lowest values of fault current, having a discrepancy of less than 4 A between the models. The discrepancy between these two models is so small that it is negligible, and they can be considered equal in fault branch results.

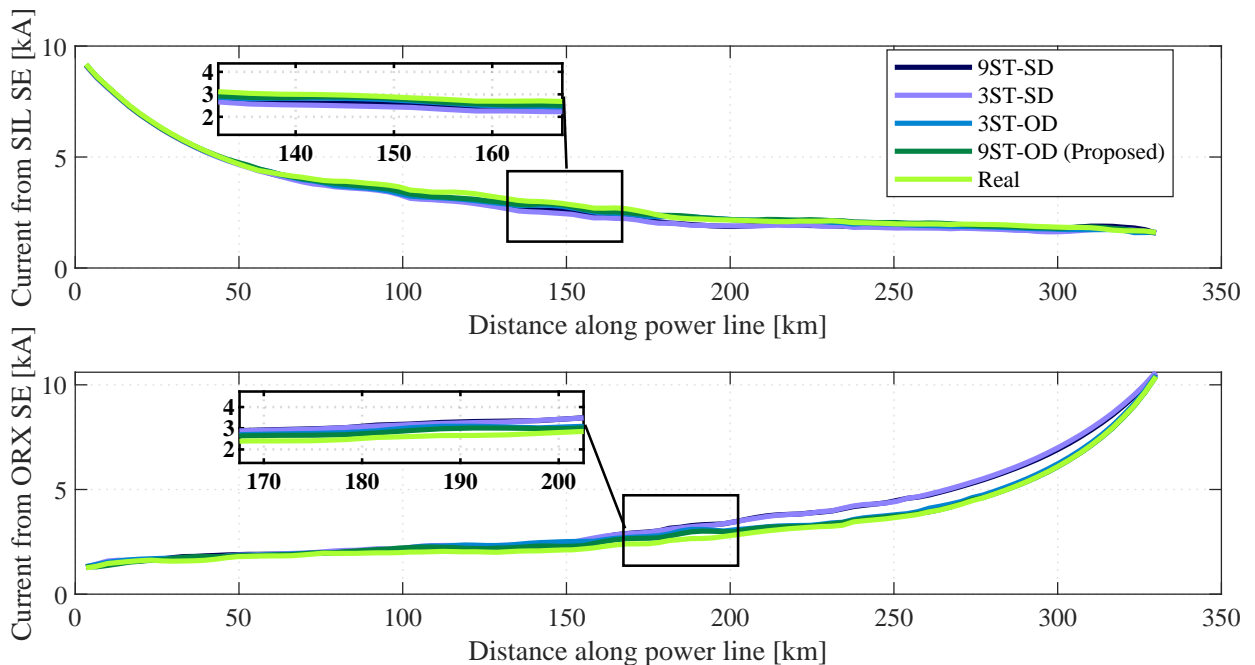
Finally, the 3ST-OD transposition scheme achieved the best three-section transposition result compared to the real model, demonstrating an average discrepancy of 1% (43.01 A) and

a maximum discrepancy of approximately 200 A.

5.4.2 Substations Contribution Currents

The maximum contribution currents of phase A in the faulted circuit (circuit 1) for the Silves and Oriximiná substations are shown in Figure 5.10.

Figure 5.10. Maximum value of contribution currents from Silves and Oriximiná substations measured on circuit 1 phase A (faulted circuit) under phase-to-ground fault conditions along the transmission line for each transposition scenario. Soils are considered frequency-dependent (FD) models and longitudinal heterogeneous along the right-of-way, as presented in Figure 3.7.



Source: Own authorship.

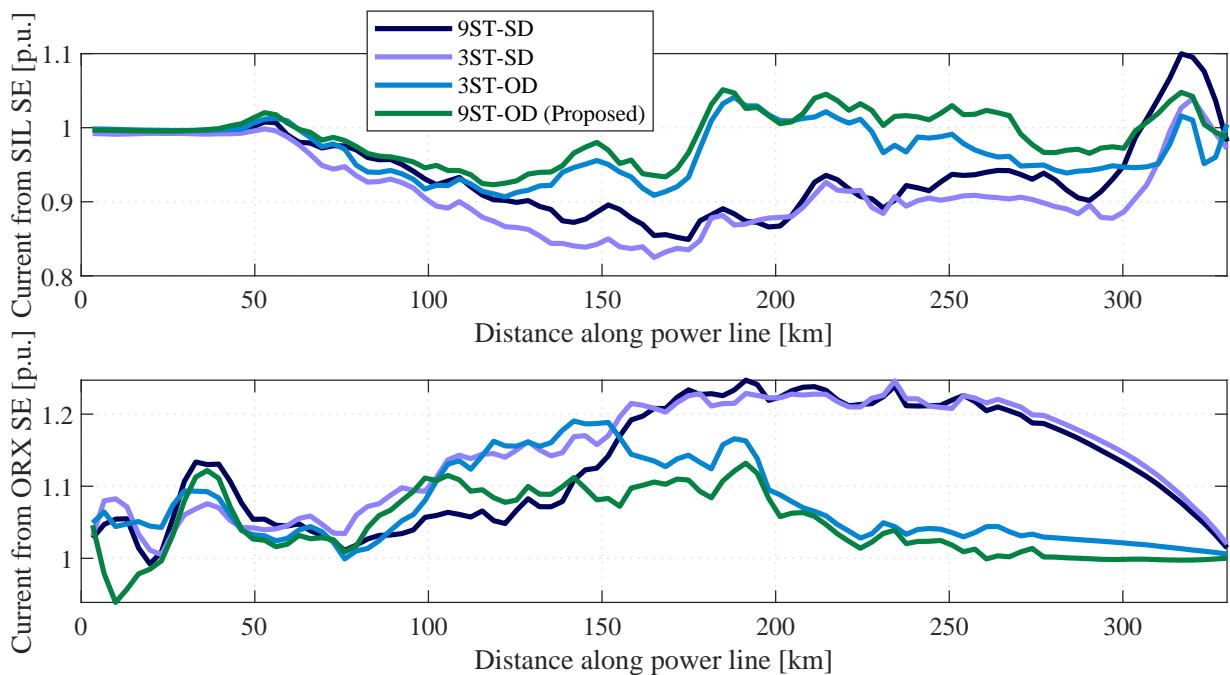
It is observed that for the faulted circuit, the contribution currents are similar among the various transposition schemes analyzed. The contribution currents are inversely proportional to the impedances seen at the terminals, and since the soil properties are the same, the zero-sequence impedances for all transpositions are equal. Therefore, although the discrepancy is small, its existence is solely due to the difference in the transposition schemes.

As in the previous case, transposition schemes that rotate the barrels in the same direction presented a rise in contribution currents on the last third of the transmission line, due to the geometric constructive aspects of the phases on the tower, which causes the faulted phase (phase

A of circuit 1) and the corresponding phase in the healthy circuit (phase A of circuit 2) to be closer on this transmission line extension. Consequently, during a fault, phase A of the healthy circuit receives a greater coupling from the faulted phase, which in turn has a higher resultant magnetic field during the fault occurrence.

The normalized contribution currents are calculated using equation (5.1) and presented in Figure 5.11 with the real transposition as reference. Table 5.5 summarizes the average discrepancies found for the faulted circuit. The reference used is the transposition scheme since it yielded the best results in terms of contribution currents.

Figure 5.11. Normalized contribution currents from Silves and Oriximiná substations measured on circuit 1 phase A (faulted circuit) under phase-to-ground fault conditions along the transmission line. The real transposition of the 500 kV double-circuit Silves-Oriximiná transmission line is used as a reference (see Figure 3.5). Soils are considered frequency-dependent (FD) models and longitudinal heterogeneous along the right-of-way, as presented in Figure 3.7.



Source: Own authorship.

From Figure 5.11, it is verified that in the last section of the transmission line, where the faulted phase is close to its analog phase in the second circuit, there is a 20% increase in contribution currents at the Oriximiná substation to compensate the 10% of contribution current decrease at the Silves substation. This effect is only observed in transpositions with analog phases from both circuits closer (9ST-SD and 3ST-SD).

Table 5.5 confirms that, on average, there is a decrease in contribution from the Silves subs-

Table 5.5. Outline of average discrepancy on substations contribution currents between the transposition schemes concerning the real transposition scheme for the faulted circuit.

Transp. schemes	Avg. of I_{norm}	
	Silves SE	Oriximiná SE
9ST-SD	0.94 p.u. 160.66 A	1.13 p.u. 419.23 A
3ST-SD	0.92 p.u. 223.63 A	1.14 p.u. 458.81 A
3ST-OD	0.96 p.u. 89.15 A	1.07 p.u. 179.56 A
9ST-OD (Proposed)	0.99 p.u. 41.05 A	1.05 p.u. 105.74 A

Source: Own authorship.

tation, which is compensated by a double contribution increase from the Oriximiná substation, regardless of the type of transposition used.

It is confirmed that, on average, the transposition schemes that adopt the same rotation direction of the circuits are less favorable and result in higher short-circuit contribution currents along most of the transmission line.

Finally, it is evident that the proposed transposition scheme, 9ST-OD, is the closest to reality and is a viable alternative to the real case, with the advantage of presenting less inductive coupling between the circuits on the same tower. However, this scheme requires twice the number of towers and is more expensive.

On the other hand, the 3ST-OD scheme achieves satisfactory results compared to the scheme used in practice, using fewer towers than the actual case and, therefore, more economically viable. The disadvantage of this scheme is the presence of negative and positive sequence coupling between both circuits.

5.5 INFLUENCE OF SHIELD WIRES MODELING ON FAULT STUDY

5.5.1 Fault Branch Currents

To analyze the influence of shield wires modeling on short-circuit level, two models are compared: (a) a simplified model considering the Kron reduction, and (b) a complete model with the shield wires explicitly modeled. Both models take into account heterogeneous soils along the transmission line with frequency-dependent parameters. The 9ST-SD transposition

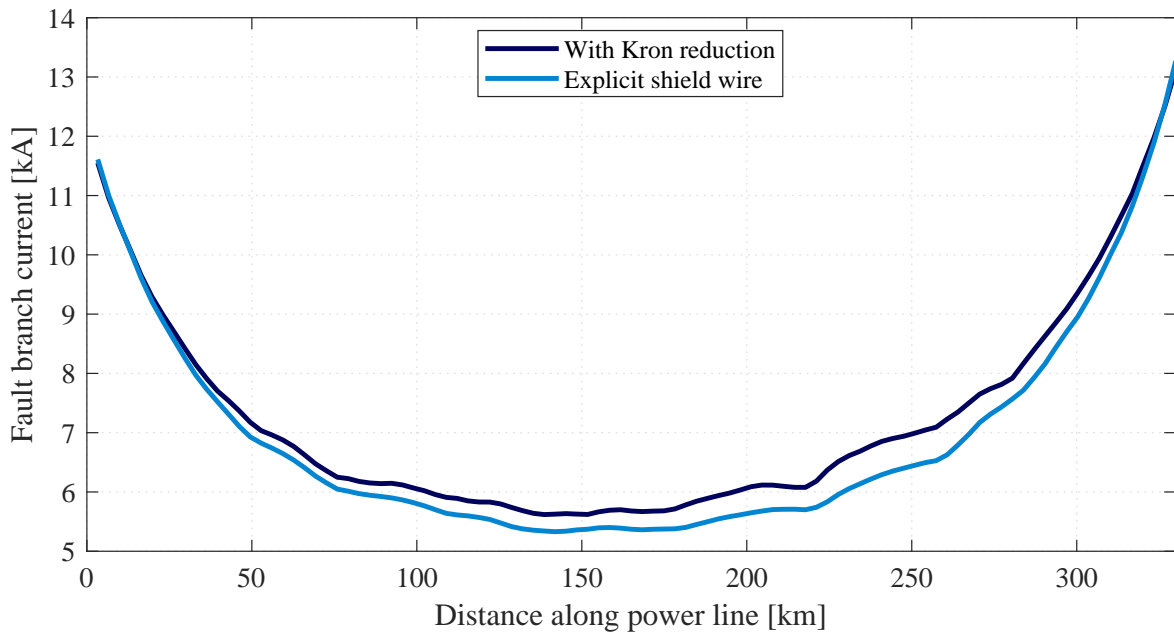
scheme is employed in both models.

Figure 5.12 presents the maximum fault currents in the fault branch for each scenario, with single-phase faults being applied along the transmission line.

It is observed that the shield wires explicitly result in lower fault currents, especially in central regions of the transmission line, where the contribution currents from the substations have less influence on the short-circuit levels. This is because, considering the Kron reduction, the currents that should be flowing from the fault point towards the substations through the shield wires are being flowed through the transmission line phases, causing a proportional rise on the fault branch current.

The maximum current in the shield wires is measured at each terminal substation of the transmission line under single-phase fault conditions, and it is presented in Figure 5.13.

Figure 5.12. Maximum absolute value of fault branch current under a single-phase fault condition, considering the simplified system with Kron reduction and the complete system with explicit shield wires.

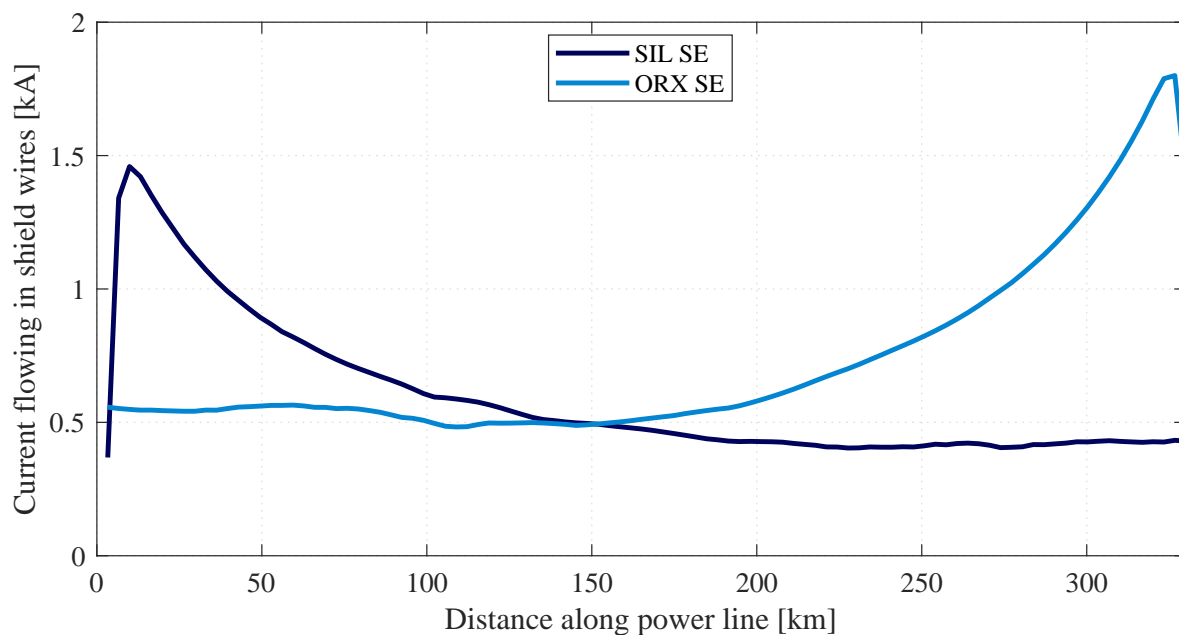


Source: Own authorship.

Figure 5.13 shows that higher currents are observed in the shield wires when faults occur near the substations. This is due to the fact that faults occurring at the terminals of the line have higher levels of short-circuit, both in contribution and in the fault branch. The consequence of this larger portion of current being flowed in the transmission line in these cases

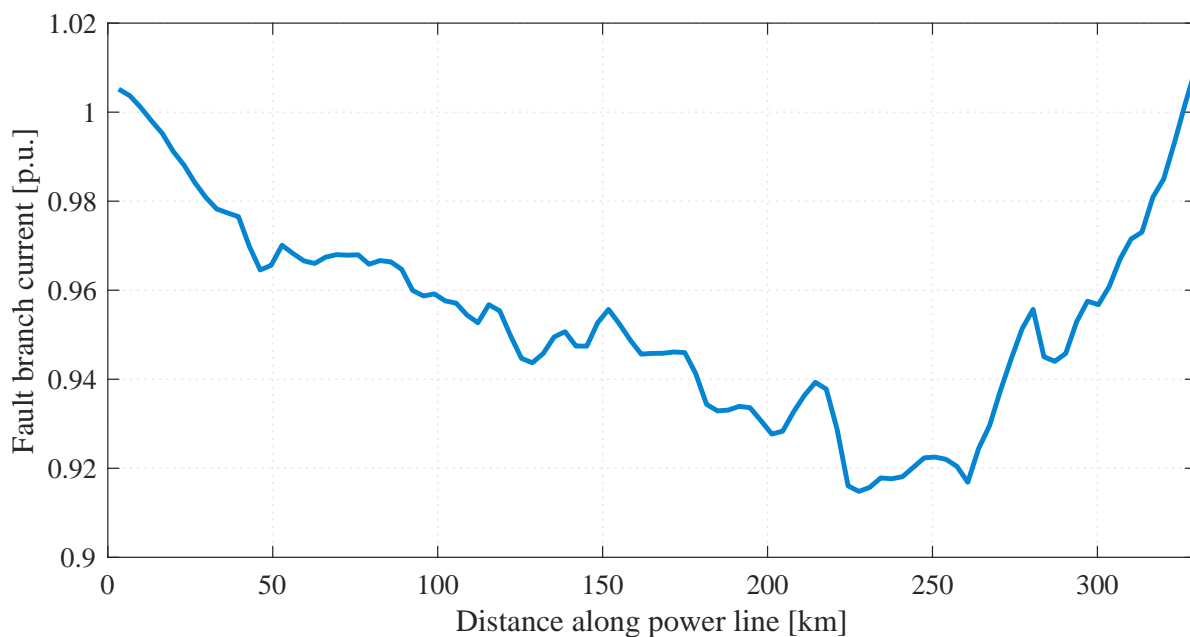
is also observed in shield wires.

Figure 5.13. Maximum shield wire currents under single-phase fault conditions at both terminals substation.



Source: Own authorship.

Figure 5.14. Normalized fault branch current under a single-phase fault (Ag) condition, considering the complete system with explicit shield wires.



Source: Own authorship.

However, even in short-circuit that low current flows in the shield wires, a significant portion

of the current is still observed (approximately 500 A).

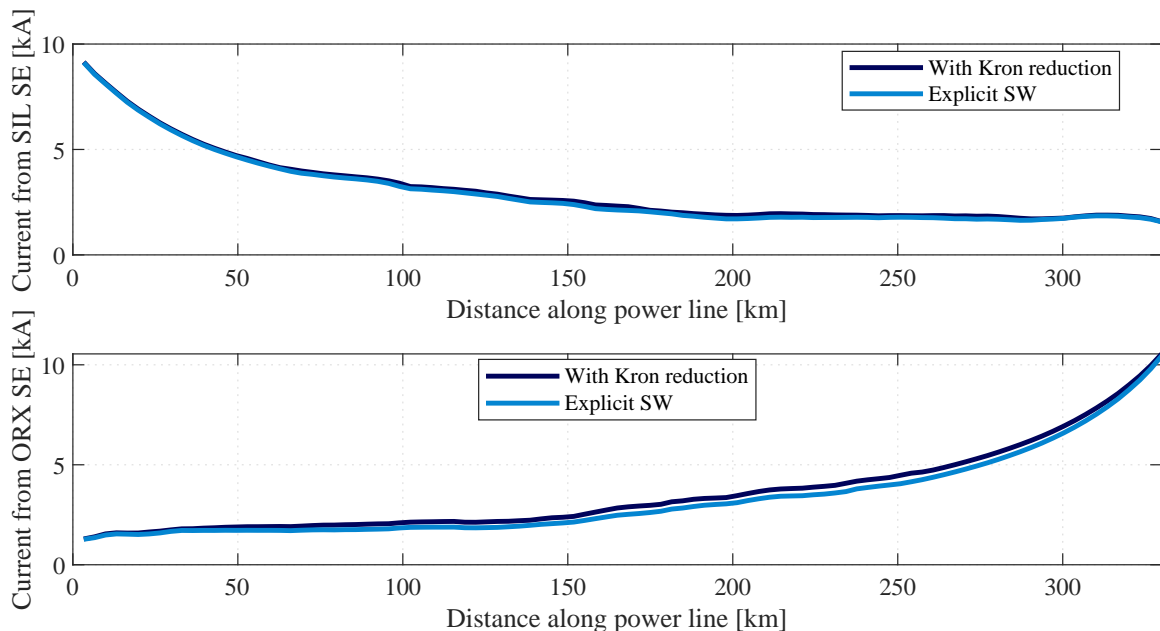
To highlight the discrepancies, the normalized fault branch current is provided using (5.1). The circuit simplified by Kron reduction is used as a ratio reference. Figure 5.14 summarizes the normalized fault branch current.

It is observed that modeling the shield wires correctly decreases the fault branch current by up to 0.91 A (approximately 700 A). On average, using Kron reduction results in a 5% increase in the fault branch current, which corresponds to approximately 307 A.

5.5.2 Substations contribution currents

The maximum values of short-circuit contribution currents along the transmission line in the faulted circuit are presented in Figure 5.15.

Figure 5.15. Maximum value of contribution currents from Silves and Oriximiná substations measured on the faulted circuit under phase-to-ground fault conditions along the transmission line for the model considering Kron reduction and for the model considering explicit shield wires. Soils are considered frequency-dependent (FD) models and longitudinal heterogeneous along the right-of-way, as presented in Figure 3.7.

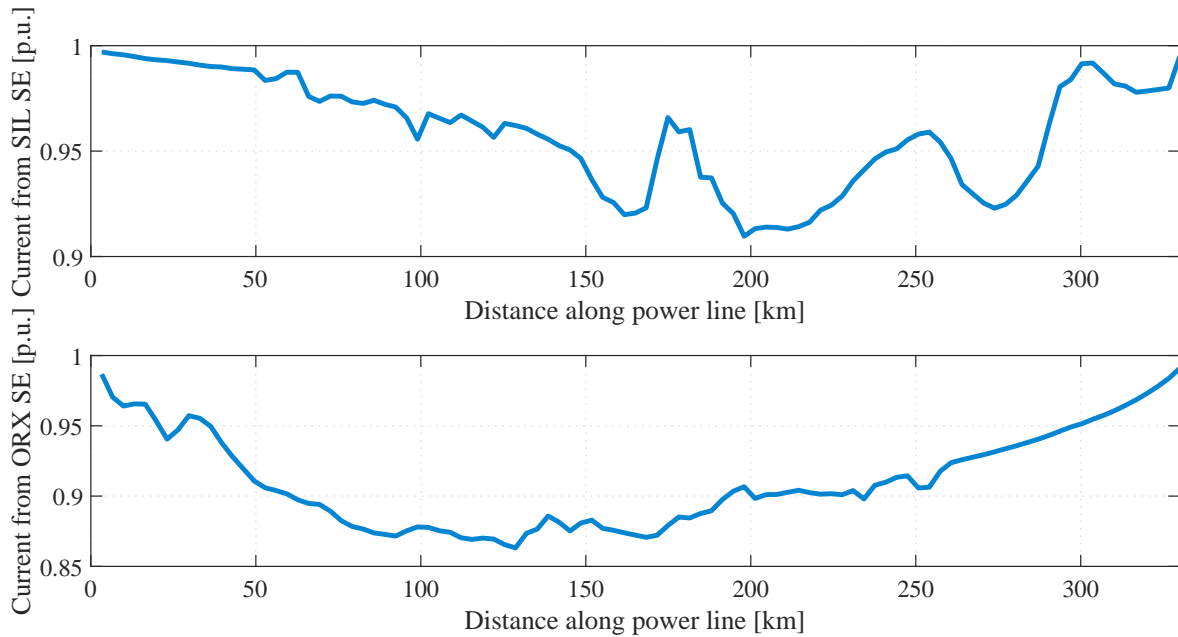


Source: Own authorship.

As for the fault branch currents, a discrepancy in the contribution currents between the two models for short circuits near the terminal substations of the transmission line is verified.

However, it is observed that considering the Kron simplification rises the contribution current at the Silves substation up to 0.1 p.u. and at the Oriximiná substation up to 0.14 p.u. On average, the Kron-reduced model produces 9.9% (276.75 A) higher currents for the Oriximiná substation and an increase of 9.9% (276.75 A) for the Silves substation currents.

Figure 5.16. Normalized contribution currents from Silves and Oriximiná substations measured on the faulted circuit under phase-to-ground fault conditions along the transmission line for the model considering explicit shield wires. Soils are considered frequency-dependent (FD) models and longitudinal heterogeneous along the right-of-way, as presented in Figure 3.7.



Source: Own authorship.

5.6 CHAPTER SUMMARY

This chapter provides an overview of the study conducted on short circuits in the 500 kV SIL-ORX transmission line. The analysis focuses on three key aspects: the soil, the transposition scheme, and the influence of shield wires. Various scenarios are evaluated to assess their impact on short-circuit levels, including fault currents and contributions from substations.

This section describes the circuit model used for the transient study, employing a cell representation for each span of the transmission line. Two simplified circuit models are presented, one using Kron reduction and the other with explicit shield wires. The ATPDraw software is utilized for the representation, and a computational routine is developed to generate the

necessary files and ATP cards.

The study assesses the influence of soil modeling and its parameters on the behavior of a transmission line. Five scenarios are considered based on real resistivity measurements, including minimum, common, average, maximum resistivities, and heterogeneous resistivity. The impact of frequency dependence on soil properties is evaluated using a constant parameter (CP) and frequency-dependent (FD) scenarios. Fault branch currents and substation contribution currents are analyzed for different soil models. Results show a small variation between frequency-dependent and frequency-invariant soil models, with the heterogeneous soil model serving as the reference. The discrepancies in fault branch currents and contribution currents are quantified, highlighting the importance of accurate soil modeling in transmission line analysis.

The impact of conductor transposition on fault studies in double-circuit transmission lines is also evaluated. Five transposition scenarios are considered, including various three-section and nine-section schemes, as well as the real transposition. The analysis focuses on faulted branch currents and substation contribution currents. It is observed that transposition schemes rotating the circuits in opposite directions exhibit better performance in fault currents, particularly in the latter portion of the transmission line. The discrepancy in fault branch currents is quantified, highlighting the higher resultant magnetic field and fault current in transpositions with circuits rotated in the same direction. The 3ST-OD scheme also achieves satisfactory results with fewer towers and economic viability.

The proposed transposition scheme, known as 9ST-OD, closely mimics the real-world scenario and offers a viable alternative with the advantage of minimizing inductive coupling between circuits on the same tower.

Finally, the influence of shield wires modeling on fault study is analyzed by comparing two models: a simplified model with Kron reduction and a complete model with explicit shield wires. The inclusion of shield wires in the complete model results in lower short-circuit currents, especially in central regions of the transmission line. The maximum currents in the shield wires occur near substations and even in cases of low current flow, a significant portion is observed. Correctly modeling shield wires decreases fault branch current by up to 0.91 A, while the Kron reduction model leads to a 5% increase on average. Contribution currents also show

discrepancies between the models, the Kron reduction model produces higher contribution currents at both substations compared to the model with explicit shield wires

CONCLUSIONS AND FUTURE WORKS

Transmission lines, as essential components of the system, impact the energy supply of regions and require reliability and robustness. However, they often face challenges such as limited space availability and interferences, which can lead to faults and power interruptions. To address these issues, double-circuit transmission lines have become more prevalent, allowing the transmission of double the power within the same space. Nevertheless, these lines present difficulties due to electromagnetic coupling between the circuits. Balancing the need for space utilization and minimizing electromagnetic interference is essential for ensuring a resilient and efficient transmission network.

Modal parameters of the transmission line were analyzed based on a 500 kV double-circuit transmission line connecting the Silves and Oriximiná substations, located in northern Brazil. The analysis focused on three main aspects: soil properties, transposition schemes, and the inclusion of shield wires.

For soil modeling, variations in resistivity and relative permittivity were considered, along with constant-frequency and frequency-dependent soil models based on real resistivity field measurements. The analysis revealed that changes in soil properties primarily affect the ground mode and inter-line mode, while the line mode is less influenced. The most conductive soil exhibited higher phase velocities and lower attenuations, and frequency-dependent soil models showed lower attenuations and higher phase velocities at high frequencies.

Three transposition schemes were evaluated, including nine-section, three-section with phase rotation in the same direction, and three-section with phase rotation in the opposite direction. It was found that the modal propagation parameters remained the same regardless of the transposition scheme, indicating that the symmetric components do not accurately represent the physical phenomena in the transmission line.

A novel transposition scheme was proposed using nine section with the barrels rotated in

opposite direction. The proposed transposition scheme, 9ST-OD, closely resembles the real case and provides a feasible alternative with the added benefit of reduced inductive coupling between the circuits on the same tower. However, this scheme necessitates twice the number of towers and incurs higher costs.

A final comparison was also made between symmetric-domain components derived from Kron reduction and modal-domain components. Results show that while similarities were observed in some modes, discrepancies in attenuation at high frequencies were noted. The symmetric-domain components accurately represented the system simplified with Kron reduction at low frequencies but exhibited significant discrepancies at high frequencies.

Lastly, the analysis emphasized the inclusion of explicitly shield wires in the system. It was highlighted that shield wires have singular propagation characteristics, particularly the attenuation constant, which cannot be accurately represented with symmetric-domain or modal-domain using Kron simplification.

Theoretical studies on the propagation parameters considering variations in soil properties, conductor transposition, and shield wires have subdivided and justified the use of the complex transmission line model, which the power line is modeled span by span, allowing for the variation of its physical, geometric and constructive parameters at each tower. This approach represents transmission lines in a realistic manner.

In addition to the studies on propagation parameters, over 1500 single-phase faults were analyzed on the transmission line connecting Silves to Oriximiná, aiming to evaluate the impacts of soil properties, transposition schemes, and shield wire modeling on electromagnetic transient studies. In all scenarios, fault branch currents and contribution currents from terminal substations were analyzed.

The short-circuit levels for soil properties showed that the variation between frequency-dependent and frequency-invariant soil models was minimal, with the heterogeneous soil model serving as the reference. Accurate soil modeling can be achieved using only one and constant soil properties based on the average of the bottom layer resistivity.

Furthermore, the evaluation of conductor transposition schemes in double-circuit transmission lines revealed important insights. Transposition schemes that rotated the circuits in oppo-

site directions demonstrated improved performance in fault currents, particularly in the latter portion of the transmission line. The analysis quantified the discrepancies in fault branch currents, highlighting the higher resultant magnetic field and fault current in transpositions with circuits rotated in the same direction. The proposed 9ST-OD transposition closely matched the real transposition, while the 3ST-OD scheme achieved satisfactory results with fewer towers and economic viability.

Finally, the influence of shield wires on fault studies was also investigated by comparing two models: a simplified model employing Kron reduction and a complete model with explicit shield wires. The inclusion of shield wires in the complete model resulted in lower short-circuit currents, particularly in central regions of the transmission line. The maximum level of currents in the shield wires was observed near substations, but even further substations currents flowing through shield wires were observed. Properly modeling shield wires decreased fault branch current by up to 0.91 A, whereas the Kron reduction model led to an average 5% increase. Discrepancies were also observed in contribution currents between the two models, with the Kron reduction model producing higher contribution currents at both substations compared to the model with explicit shield wires.

Overall, this study highlights the importance of accurate modeling and analysis techniques in understanding the behavior of transmission lines during fault conditions. The findings contribute to the improvement of the transmission line design, protection systems, and the overall reliability of power systems.

Future research can build upon these findings to further enhance the understanding and performance of double-circuit transmission lines. Some of these studies can be addressed by the author soon:

- Include to the computational routine that creates the punch (.pch) files, that represent the standard Line/Cable Constants, by a true multilayered version allowing for the simulation of high-frequency phenomena up to 2 MHz;
- Extended modal parameters and shield wires influences on direct current (DC) transmission lines;
- Inclusion of underground transmission line models, considering the calculation of impe-

dance and admittance for a multilayered soil;

- Additional application studies related to high-frequency electromagnetic transients such as atmospheric discharges;
- Additional studies related to faults that involve the shield wires in comparison with the commonly used Kron reduction simplification;
- Implementation of traveling-wave fault location methods based on modal propagation parameters instead of symmetrical components, aiming to improve the accuracy of the models mainly in high-frequency events.

BIBLIOGRAPHY

- ABB, H.; EVOLTZ. *Modelagem ATP Tronco 500 kV Tucuruí – Manaus – Macapá*. [S.l.], 2021. Cited 4 times in pages 49, 50, 52, and 54.
- ABNT. *NBR 7117 - Medição da Resistividade e Determinação da Estratificação do Solo*. 2012. 1–72 p. Cited in page 35.
- ALAMO, J. del. A Comparison Among Eight Different Techniques to Achieve an Optimum Estimation of Electrical Grounding Parameters in Two-Layered Earth. *IEEE Transactions on Power Delivery*, v. 8, n. 4, p. 1890–1899, 1993. Cited in page 36.
- ALIPIO, R.; VISACRO, S. Frequency dependence of soil parameters: Effect on the lightning response of grounding electrodes. *IEEE Transactions on Electromagnetic Compatibility*, v. 55, n. 1, p. 132–139, 2013. Cited 2 times in pages 3 and 4.
- ALÍPIO, R.; VISACRO, S. A new model for the frequency dependence of soil parameters. *2014 International Conference on Lightning Protection (ICLP)*, p. 1432–1436, 2014. Cited 3 times in pages 2, 3, and 37.
- AMETANI, A.; YONEDA, T.; BABA, Y.; NAGAOKA, N. An Investigation of Earth-Return Impedance Between Overhead and Underground Conductors and Its Approximation. *IEEE Transactions on Electromagnetic Compatibility*, v. 51, n. 3, p. 860–867, 2009. ISSN 0018-9375. Disponível em: <<http://ieeexplore.ieee.org/lpdocs/epic03/wrapper.htm?arnumber=4914803>>. Cited in page 12.
- CARSON, J. R. Wave Propagation in Overhead Wires with Ground Return. *Bell Syst. Tech. J.*, v. 5, p. 539–554, 1926. Cited 2 times in pages 2 and 10.
- CAVKA, D.; MORA, N.; RACHIDI, F. A comparison of frequency-dependent soil models: Application to the analysis of grounding systems. *IEEE Transactions on Electromagnetic Compatibility*, v. 56, n. 1, p. 177–187, 2014. Cited in page 37.
- CHAVES, D. B.; CHAGAS, N. B. Características e comportamentos do efeito pelicular. *Anais do 8º Salão Internacional de Ensino, Pesquisa e Extensão da Universidade Federal do Pampa*, 2016. Cited in page 17.
- CHRYSOCHOS, A. I.; PAPADOPOULOS, T. A.; PAPAGIANNIS, G. K. Robust calculation of frequency-dependent transmission-line transformation matrices using the levenberg–marquardt method. *IEEE Transactions on Power Delivery*, v. 29, n. 4, p. 1621–1629, 2014. Cited in page 32.
- DAS, S.; SANTOSO, S.; GAIKWAD, A.; PATEL, M. Impedance-based Fault Location in Transmission Networks: Theory and Application. *IEEE Access*, v. 2, p. 537–557, 2014. ISSN 21693536. Cited in page 2.

- DAWALIBI, F.; BLATTNER, C. Earth Resistivity Measurement Interpretation Techniques. *IEEE Transactions on Power Apparatus and Systems*, PAS-103, n. 2, p. 374–382, 1984. ISSN 0018-9510. Cited 2 times in pages 36 and 45.
- Deri, A., Tevan, G. The Complex Ground Return Plane - A Simplified Model for Homogeneous and Multi-Layer Earth Return. n. August, p. 31–32, 1981. Cited 2 times in pages 3 and 12.
- DOMMEL, H.; BHATTACHARYA, S. *EMTP Theory Book*. Microtran Power System Analysis Corporation, 1992. Disponível em: <https://books.google.com.br/books?id=dy3_mgEACAAJ>. Cited 15 times in pages 3, 8, 9, 10, 15, 17, 19, 20, 21, 22, 23, 24, 25, 26, and 27.
- ELGUERA, A. V.; TAVARES, M. C. Influence of transmission line transposition in electromagnetic transients phenomena. In: *2006 IEEE/PES Transmission Distribution Conference and Exposition: Latin America*. [S.l.: s.n.], 2006. p. 1–6. Cited in page 3.
- FEDOROV, A.; PETROV, V.; NAUMOV, V. The rules for using modal transformation in traveling wave fault locator. In: *2022 International Ural Conference on Electrical Power Engineering (UralCon)*. [S.l.: s.n.], 2022. p. 54–58. Cited 4 times in pages 1, 2, 4, and 25.
- FERNANDES, A.; NEVES, W. Phase-domain transmission line models considering frequency-dependent transformation matrices. *IEEE Transactions on Power Delivery*, v. 19, n. 2, p. 708–714, 2004. Cited in page 32.
- FRANCIS, J. G. F. The QR Transformation A Unitary Analogue to the LR Transformation—Part 1. *The Computer Journal*, v. 4, n. 3, p. 265–271, 01 1961. ISSN 0010-4620. Disponível em: <<https://doi.org/10.1093/comjnl/4.3.265>>. Cited in page 32.
- FRANCIS, J. G. F. The QR Transformation—Part 2. *The Computer Journal*, v. 4, n. 4, p. 332–345, 01 1962. ISSN 0010-4620. Disponível em: <<https://doi.org/10.1093/comjnl/4.4.332>>. Cited in page 32.
- GIL, M.; ABDOOS, A. A.; SANAYE-PASAND, M. A precise analytical method for fault location in double-circuit transmission lines. *International Journal of Electrical Power Energy Systems*, v. 126, p. 106568, 2021. ISSN 0142-0615. Disponível em: <<https://www.sciencedirect.com/science/article/pii/S014206152032161X>>. Cited 3 times in pages 1, 2, and 4.
- HE, J.; ZENG, R.; ZHANG, B. *Methodology and Technology for Power System Grounding*. [S.l.: s.n.], 2012. 1–566 p. ISBN 9781118254950. Cited 2 times in pages 2 and 36.
- HOFMANN, L. Series expansions for line series impedances considering different specific resistances, magnetic permeabilities, and dielectric permittivities of conductors, air, and ground. *IEEE Transactions on Power Delivery*, v. 18, n. 2, p. 564–570, 2003. Cited in page 3.
- IEEE Std 80. *Guide for Safety In AC Substation Grounding*. 2000. 1–192 p. Cited 2 times in pages 34 and 35.
- KIKUCHI, H. Wave propagation along an infinite wire above ground at high frequencies. *Electrotech*, 1956. Cited in page 3.

- LEVENBERG, K. A method for the solution of certain non-linear problems in least squares. *Quarterly of Applied Mathematics*, Brown University, v. 2, n. 2, p. 164–168, 1944. ISSN 0033569X, 15524485. Disponível em: <<http://www.jstor.org/stable/43633451>>. Cited in page 32.
- LONGMIRE, C. L.; SMITH, K. A universal impedance for soils. In: . [S.l.: s.n.], 1975. Cited 2 times in pages 3 and 37.
- LOPES, F. V.; REIS, R. L. A.; SILVA, K. M.; MARTINS-BRITTO, A.; RIBEIRO, E. P. A.; MORAES, C. M.; RODRIGUES, M. A. M. Past, present, and future trends of traveling wave-based fault location solutions. In: *2021 Workshop on Communication Networks and Power Systems (WCNPS)*. [S.l.: s.n.], 2021. p. 1–6. Cited 3 times in pages 1, 2, and 4.
- LUCCA, G. Mutual Impedance between an Overhead and a Buried Line with Earth Return. In: *Proc. Int. Electr. Eng. 9th Int. Conf. EMC*. [S.l.: s.n.], 1994. p. 80–86. Cited in page 12.
- MARQUARDT, D. W. An algorithm for least-squares estimation of nonlinear parameters. *Journal of the Society for Industrial and Applied Mathematics*, Society for Industrial and Applied Mathematics, v. 11, n. 2, p. 431–441, 1963. ISSN 03684245. Disponível em: <<http://www.jstor.org/stable/2098941>>. Cited in page 32.
- MARTINS-BRITTO, A. G. *Modeling of the Electromagnetic Interferences between Power Lines and Underground Metallic Pipelines and Impact Analysis*. 121 p. Tese (Master's Thesis) — University of Brasília, 2017. Cited in page 36.
- MARTINS-BRITTO, A. G. *Realistic Modeling of Power Lines for Transient Electromagnetic Studies*. 187 p. Tese (Doutorado) — University of Brasília, 2020. Cited 2 times in pages 4 and 11.
- MARTINS-BRITTO, A. G.; LOPES, F. V.; RONDINEAU, S. R. M. J. Multi-layer Earth Structure Approximation by a Homogeneous Conductivity Soil for Ground Return Impedance Calculations. *IEEE Transactions on Power Delivery*, v. 8977, n. c, p. 1–1, 2019. ISSN 0885-8977. Cited 2 times in pages 45 and 46.
- MARTINS-BRITTO, A. G.; MORAES, C. M.; LOPES, F. V.; RONDINEAU, S. Low-frequency electromagnetic coupling between a traction line and an underground pipeline in a multilayered soil. In: *2020 Workshop on Communication Networks and Power Systems (WCNPS)*. [S.l.: s.n.], 2020. p. 1–6. Cited 4 times in pages 4, 45, 46, and 78.
- MARTINS-BRITTO, A. G.; PAPADOPOULOS, T. A.; DATSIOS, Z. G.; CHRYSOCHOS, A. I.; PAPAGIANNIS, G. K. Influence of lossy ground on high-frequency induced voltages on aboveground pipelines by nearby overhead transmission lines. *IEEE Transactions on Electromagnetic Compatibility*, v. 64, n. 6, p. 2273–2282, 2022. Cited in page 47.
- MONTEIRO, J. S. *Cálculo dos Parâmetros de Linhas de Transmissão para Estudos de Fluxo de Potência Considerando o Efeito de Outras Linhas Fisicamente Próximas*. 1-62 p., 7 2004. Cited 10 times in pages 1, 8, 9, 21, 22, 23, 24, 25, 27, and 29.
- NITHYAVELAM, M.; HENRY, J. Transmission lines fault detection using discrete wavelet transform and artificial neural network algorithm. *ARPN Journal of Engineering and Applied Sciences*, v. 13, n. 16, p. 4625–4632, 2018. ISSN 18196608. Cited in page 72.

NODA, T. A double logarithmic approximation of carson's ground-return impedance. In: *2006 IEEE Power Engineering Society General Meeting*. [S.l.: s.n.], 2006. p. 1 pp.–. Cited in page 3.

PAPADOPOULOS, T. A.; DATSIOS, Z. G.; CHRYSOCHOS, A. I.; MIKROPOULOS, P. N.; PAPAGIANNIS, G. K. Wave propagation characteristics and electromagnetic transient analysis of underground cable systems considering frequency-dependent soil properties. *IEEE Transactions on Electromagnetic Compatibility*, v. 63, n. 1, p. 259–267, 2021. Cited in page 33.

PAPADOPOULOS, T. A.; PAPAGIANNIS, G. K. Influence of earth permittivity on overhead transmission line earth-return impedances. In: *2007 IEEE Lausanne Power Tech*. [S.l.: s.n.], 2007. p. 790–795. Cited 3 times in pages 37, 38, and 39.

PAPADOPOULOS, T. A.; PAPAGIANNIS, G. K.; LABRIDIS, D. P. A generalized model for the calculation of the impedances and admittances of overhead power lines above stratified earth. *Electric Power Systems Research*, v. 80, n. 9, p. 1160–1170, 2010. ISSN 0378-7796. Disponível em: <<https://www.sciencedirect.com/science/article/pii/S0378779610000684>>. Cited 4 times in pages 2, 37, 38, and 39.

PAPAGIANNIS, G.; TRIANTAFYLLIDIS, D.; LABRIDIS, D. A one-step finite element formulation for the modeling of single and double-circuit transmission lines. *IEEE Transactions on Power Systems*, v. 15, n. 1, p. 33–38, 2000. Cited in page 3.

PAPAGIANNIS, G.; TSIAMITROS, D.; LABRIDIS, D.; DOKOPOULOS, P. A systematic approach to the evaluation of the influence of multilayered earth on overhead power transmission lines. *IEEE Transactions on Power Delivery*, v. 20, n. 4, p. 2594–2601, 2005. Cited in page 3.

PETTERSSON, P. Image representation of wave propagation on wires above, on and under ground. *IEEE Transactions on Power Delivery*, v. 9, n. 2, p. 1049–1055, 1994. Cited in page 3.

PORTELA, C. Measurement and modeling of soil electromagnetic behavior. In: *1999 IEEE International Symposium on Electromagnetic Compatibility. Symposium Record (Cat. No.99CH36261)*. [S.l.: s.n.], 1999. v. 2, p. 1004–1009 vol.2. Cited in page 3.

PORTELA, C.; TAVARES, M. C. Modelling simulation and optimization of transmission line. In: *IEEE Transmission and Distribution Latin America 2002*. [S.l.: s.n.], 2002. Cited in page 3.

RACHIDI, F.; NUCCI, C.; IANOZ, M. Transient analysis of multiconductor lines above a lossy ground. *IEEE Transactions on Power Delivery*, v. 14, n. 1, p. 294–302, 1999. Cited in page 3.

SAZALI, M. S.; WOOL, C.; ARSHAD, S.; WONG, T.; ABDUL-MALEK, Z.; NABIPOUR-AFROUZI, H. Study of soil resistivity using wenner four pin method: Case study. In: *2020 IEEE International Conference on Power and Energy (PECon)*. [S.l.: s.n.], 2020. p. 386–391. Cited in page 33.

SCOTT, J. H. Electrical and magnetic properties of rock and soil. *U.S. Geological Survey*, 1966. Cited in page 3.

SEMLYEN, A. Ground return parameters of transmission lines an asymptotic analysis for very high frequencies. *IEEE Transactions on Power Apparatus and Systems*, PAS-100, n. 3, p. 1031–1038, 1981. Cited 3 times in pages 37, 38, and 39.

SMITH-ROSE, R. L. The electrical properties of soil for alternating currents at radio frequencies. *Royal Society*, v. 140, n. 841, 1933. Cited in page 3.

TAKAHASHI, T.; KAWASE, T. Analysis of Apparent Resistivity in a Multi-Layer Earth Structure. *IEEE Transactions on Power Delivery*, v. 5, n. 2, p. 604–612, 1990. Cited in page 35.

THEODOULIDIS, T. On the Closed-Form Expression of Carson's Integral. *Periodica Polytechnica, Electrical Engineering*, v. 59, n. 1, p. 26–29, 2015. ISSN 15873781. Cited 2 times in pages 3 and 13.

TRIANAFYLLIDIS, D.; PAPAGIANNIS, G.; LABRIDIS, D. Calculation of overhead transmission line impedances a finite element approach. *IEEE Transactions on Power Delivery*, v. 14, n. 1, p. 287–293, 1999. Cited in page 3.

TSIAMITROS, D. A.; PAPAGIANNIS, G. K.; DOKOPOULOS, P. S.; ARRANGEMENT, A. O. L. Homogenous Earth Approximation of Two-Layer Earth Structures: An Equivalent Resistivity Approach. *IEEE Transactions on Power Delivery*, v. 22, n. 1, p. 658–666, 2007. Cited in page 35.

TSIAMITROS, D. A.; PAPAGIANNIS, G. K.; DOKOPOULOS, P. S.; EQUATIONS, A. E. F. Earth return impedances of conductor arrangements in multilayer soils - part i : Theoretical model. *IEEE Transactions on Power Delivery*, v. 23, p. 2392–2400, 2008. Cited in page 11.

TSIAMITROS, D. A.; PAPAGIANNIS, G. K.; DOKOPOULOS, P. S.; POWER, A. O.; LINES, T. Earth return impedances of conductor arrangements in multilayer soils ? part ii : Numerical results. *IEEE Transactions on Power Delivery*, v. 23, p. 2401–2408, 2008. Cited in page 11.

VISACRO, S.; ALIPIO, R. Frequency dependence of soil parameters: Experimental results, predicting formula and influence on the lightning response of grounding electrodes. *IEEE Transactions on Power Delivery*, v. 27, n. 2, p. 927–935, 2012. Cited 2 times in pages 3 and 4.

VISACRO, S.; ALIPIO, R.; VALE, M. H. M.; PEREIRA, C. The response of grounding electrodes to lightning currents: The effect of frequency-dependent soil resistivity and permittivity. *IEEE Transactions on Electromagnetic Compatibility*, v. 53, n. 2, p. 401–406, 2011. Cited in page 3.

WEDEPOHL, L.; NGUYEN, H.; IRWIN, G. Frequency-dependent transformation matrices for untransposed transmission lines using newton-raphson method. *IEEE Transactions on Power Systems*, v. 11, n. 3, p. 1538–1546, 1996. Cited in page 31.

WEDEPOHL, L. M. Application of matrix methods to the solution of travelling-wave phenomena in polyphase systems. In: . [S.l.: s.n.], 1963. Cited in page 31.

WENNER, F. A method for measuring earth resistivity. *Journal of The Franklin Institute-engineering and Applied Mathematics*, v. 180, p. 373–375, 1915. Cited in page 33.

- WG-36.02, C. *Publication n. 95 - Guide on the Influence of High Voltage AC Power Systems on Metallic Pipelines*. Paris: CIGRÉ, 1995. 1–135 p. Disponível em: <<http://www.e-cigre.org/Order/select.asp?ID=96>>. Cited 3 times in pages 12, 16, and 33.
- WG-C4.33. *Technical publication n°. 781 - Impact of soilparameter frequency dependence on the response of grounding electrodes and on the lightning performance of electrical systems*. [S.l.]: CIGRÉ, 2019. 1–135 p. Cited 3 times in pages 3, 37, and 38.
- WHEELER, H. A. Formulas for the skin effect. *Proceedings of the Institute of Radio Engineers*, v. 30, 1942. Cited in page 17.
- WHELAN J.M; HANRATTY, B. M. E. Earth Resistivity in Ireland. In: *CDEGS Users' Group*. Montreal: [s.n.], 2010. p. 155–164. Cited 3 times in pages 2, 12, and 35.
- WISE, W. Propagation of high-frequency currents in ground return circuits. *Proceedings of the Institute of Radio Engineers*, v. 22, n. 4, p. 522–527, 1934. Cited 3 times in pages 3, 13, and 16.
- WISE, W. H. Effect of ground permeability on ground return circuits. *The Bell System Technical Journal*, v. 10, n. 3, p. 472–484, 1931. Cited 3 times in pages 3, 13, and 16.
- WISE, W. H. Potential coefficients for ground return circuits. *The Bell System Technical Journal*, v. 27, n. 2, p. 365–371, 1948. Cited 3 times in pages 3, 13, and 16.
- XUE, H.; AMETANI, A.; MAHSEREDJIAN, J.; KOCAR, I. Generalized formulation of earth-return impedance/admittance and surge analysis on underground cables. *IEEE Transactions on Power Delivery*, v. 33, n. 6, p. 2654–2663, 2018. Cited in page 33.
- YU JUNJUN WU, D. D. Z. Fault location of t-type line with double-circuit line on the same tower with asymmetrical parameters. In: *16th Annual Conference of China Electrotechnical Society*. [S.l.: s.n.], 2022. p. 1–6. Cited 2 times in pages 1 and 2.
- ZHANG, B.; CUI, X.; LI, L.; HE, J. Parameter Estimation of Horizontal Multilayer Earth by Complex Image Method. *IEEE Transactions on Power Delivery*, v. 20, n. 2 II, p. 1394–1401, 2005. ISSN 08858977. Cited 2 times in pages 34 and 35.

APPENDIX A

SOIL RESISTIVITY MEASUREMENTS

During the construction of the 500 kV double-circuit transmission line between the Silves and Oriximiná substations, field measurements of soil resistivity were carried out along the right-of-way from October 2010 to March 2011. The collected data, summarizing the resistivity values, is presented in Table A.1. The apparent resistivities were measured using the Wenner method, as explained in Section 2.8.1, with the probe inserted 20 cm ($c = 20$ cm) into the soil.

Table A.1: Real data from apparent soil resistivity measurements along the path of the 500 kV Silves-Oriximiná transmission line.

Measurement point	Distance along the power line [m]	Apparent resistivity [Ωm]				
		a = 1m	a = 2m	a = 4m	a = 8m	a = 16m
1	0	1153.593	2429.708	3872.955	5629.734	5695.079
2	558.5427	777.8583	1756.779	2470.548	3857.876	5197.451
3	1117.0854	224.6239	334.2655	730.1061	1080.708	1869.876
4	1675.6281	1090.761	1809.557	2121.203	1095.788	4187.115
5	2234.1708	700.261	979.5486	1245.327	1015.363	864.5663
6	2792.7135	1051.491	1611.637	1925.168	2400.177	3015.929
7	3351.2562	853.2566	1463.982	997.7698	776.6017	472.4955
8	3909.7989	2170.841	2688.575	2141.31	1847.256	2483.115
9	5026.8843	964.1548	1643.681	1881.186	1688.92	291.5398
10	7261.0551	123.1504	172.1593	183.469	196.0354	231.2212
11	8936.6832	1144.168	1704	1964.124	1397.38	1120.92
12	9495.2259	321.0708	559.2035	722.5663	774.0884	583.0796
13	10053.7686	1007.823	1783.796	2150.106	1945.274	1251.611
14	10612.3113	1121.549	1844.115	2401.433	2935.504	1955.327
15	11170.854	10.99557	2138.796	2757.062	2196.602	1754.265
16	11729.3967	551.161	2096.699	3273.54	4807.893	5287.929
17	12287.9394	1169.615	1436.336	1878.672	2774.655	3216.991
18	12846.4821	2.199115	906.6636	3625.398	5338.194	6675.256
19	13405.0248	2.230531	1122.868	3049.858	4307.752	4649.557
20	13963.5675	1092.332	1572.053	3459.522	5835.823	5865.982
21	14522.1102	1066.257	1652.478	2534.637	3277.309	7067.327
22	15080.6529	811.7875	1438.849	2153.876	2985.77	3136.566
23	15639.1956	1526.814	2510.761	3739.752	1852.283	1593.416
24	18431.9091	2500.708	2909.115	3279.823	2505.734	2478.088
25	19548.9945	2148.849	1979.203	1835.947	3010.902	1492.885

Table A.1: Real data from apparent soil resistivity measurements along the path of the 500 kV Silves-Oriximiná transmission line.

Measurement point	Distance along the power line [m]	Apparent resistivity [Ωm]				
		a = 1m	a = 2m	a = 4m	a = 8m	a = 16m
26	20666.0799	1633.628	1847.256	1470.265	2086.018	3337.628
27	24017.3361	3226.416	4687.256	5893.628	11043.33	10887.5
28	24575.8788	2170.841	2060.256	2141.31	1847.256	2483.115
29	25134.4215	1884.956	2165.186	2065.911	2304.672	3639.221
30	25692.9642	827.8097	1270.46	1874.902	2312.212	2895.292
31	26251.5069	904.7787	1416.23	2003.079	3124	4172.035
32	26810.0496	947.8185	1215.168	1701.487	2973.203	4388.177
33	28485.6777	1859.823	2497.566	3120.23	4048.885	4910.938
34	29044.2204	2148.849	3707.079	4975.026	5230.123	7755.964
35	29602.7631	1533.097	3267.256	4371.84	6642.584	7504.637
36	30719.8485	3898.716	6151.238	7062.3	6343.504	8032.424
37	32395.4766	2409.602	3876.725	6232.92	6182.654	6951.716
38	35746.7328	2557.256	3637.964	4452.265	4727.469	6016.778
39	36305.2755	2425.31	3788.761	4398.23	5074.3	7615.221
40	36863.8182	3132.168	4134.336	5123.309	4682.23	8318.937
41	37422.3609	2774.026	4347.964	6094.69	7177.911	7348.814
42	37980.9036	2861.991	4611.858	5629.734	7213.097	6428.955
43	38539.4463	2343.628	3593.982	4096.637	5338.194	5152.212
44	39097.989	2293.363	3059.911	3430.619	3289.876	4016.212
45	39656.5317	2818.009	3468.318	3996.106	5139.646	6077.097
46	40215.0744	3210.708	4379.38	4146.902	6056.991	6539.539
47	40773.6171	3034.779	4932.3	6584.778	7534.796	8620.53
48	41332.1598	3653.672	4812.92	5189.911	7333.734	38050.97
49	67025.124	1052.434	1514.248	2329.805	3490.938	5378.407
50	67583.6667	816.8141	1204.487	1774.372	2834.973	4156.955
51	68700.7521	1291.195	1665.044	2523.327	3976	4835.539
52	69259.2948	1398.009	1979.203	2646.478	4074.017	5871.008
53	70934.9229	1322.611	1589.646	2789.734	4478.654	4006.159
54	71493.4656	901.6371	1205.115	1883.699	2978.23	4961.203
55	72052.0083	703.7168	1146.681	1979.203	3724.672	5237.663
56	72610.551	1124.69	1463.982	2473.062	3779.964	4528.92
57	73169.0937	435.4247	795.4513	1614.779	2468.035	4322.831
58	73727.6364	2070.31	3022.212	4599.292	6232.92	5720.212
59	76520.3499	1872.389	3970.973	5617.168	8318.937	7615.221
60	77078.8926	4184.601	4718.672	5730.265	9198.583	10525.59
61	77637.4353	1991.77	3003.363	3254.69	2646.478	1824.637
62	78195.978	2403.318	3719.646	5943.893	6207.787	3659.327
63	79871.6061	813.6725	1489.115	2270.743	3872.955	4860.672
64	80430.1488	747.6991	1163.646	9614.53	2533.38	4976.283
65	80988.6915	1017.876	1495.398	1857.31	2525.84	1533.097
66	81547.2342	5840.221	5233.893	3304.955	3146.619	7951.999
67	82105.7769	2224.248	3286.106	4636.991	6056.991	9409.698
68	82664.3196	2657.787	4366.814	5252.743	6961.769	7660.46
69	83222.8623	2035.752	3304.955	5277.876	7288.495	11289.63

Table A.1: Real data from apparent soil resistivity measurements along the path of the 500 kV Silves-Oriximiná transmission line.

Measurement point	Distance along the power line [m]	Apparent resistivity [Ωm]				
		a = 1m	a = 2m	a = 4m	a = 8m	a = 16m
70	83781.405	3273.54	4310.265	5931.327	6559.645	10857.34
71	84339.9477	1507.964	1891.239	2651.504	3257.203	4448.495
72	84898.4904	1187.522	1270.46	1463.982	1683.894	2855.079
73	85457.0331	1985.487	3015.929	3493.451	4415.823	2880.212
74	86015.5758	1511.106	2664.071	3769.911	23102.02	5529.203
75	86574.1185	1457.699	1539.38	2231.787	2865.133	2457.982
76	87132.6612	1517.389	2890.265	3707.079	5114.513	2523.327
77	87691.2039	2217.964	1866.106	662.2477	293.8017	1682.888
78	88249.7466	882.7875	1420	1369.734	857.0265	462.4424
79	88808.2893	2717.478	3248.407	3619.115	3171.752	2171.469
80	89366.832	1856.681	2582.389	2338.602	1998.053	913.8265
81	89925.3747	882.7875	1420	1369.734	857.0265	462.4424
82	93276.6309	2585.531	1573.31	1639.911	1726.619	1769.345
83	93835.1736	961.3274	1608.495	1505.451	1520.531	1144.042
84	94393.7163	1108.982	1677.61	2039.522	1256.637	687.6318
85	94952.259	1225.221	1463.982	1678.867	1701.487	1296.849
86	95510.8017	1828.407	1458.956	1372.248	741.4159	748.9557
87	96069.3444	1030.442	1221.451	1123.434	756.4955	392.0708
88	96627.8871	923.6282	1087.619	1436.336	1133.487	638.3716
89	97186.4298	1027.301	1690.177	1760.549	2023.186	1930.195
90	97744.9725	1778.141	2224.248	1945.274	1786.938	2965.663
91	98303.5152	429.1416	520.2477	1166.159	2063.398	4584.212
92	99420.6006	3769.911	4586.725	4724.955	5830.796	6041.911
93	99979.1433	1168.672	1394.867	1810.814	2028.212	2035.752
94	100537.686	1190.664	1066.257	1476.549	1457.699	1633.628
95	101096.2287	3763.628	4222.301	5240.177	4174.548	1352.141
96	101654.7714	3776.194	4272.566	5303.008	4833.026	4885.805
97	103330.3995	2042.035	3078.761	3832.743	4219.787	4126.796
98	103888.9422	3163.584	4021.239	4649.557	4828	3347.681
99	105564.5703	1448.274	1677.61	2009.363	1201.848	2427.823
100	106123.113	2089.159	2412.743	3053.628	3976	3528.637
101	106681.6557	2431.593	2796.017	2789.734	1985.487	1042.506
102	107240.1984	2802.301	2569.823	3292.389	3865.416	1548.177
103	107798.7411	1105.841	1204.487	1663.787	2535.894	2890.265
104	116176.8816	1495.398	1470.265	1234.018	1512.991	2151.363
105	116735.4243	2525.84	1828.407	1657.504	1540.637	3453.239
106	118969.5951	425.6858	520.8761	792.938	809.2743	1196.318
107	122320.8513	1140.398	1542.522	1761.805	1281.77	1110.867
108	122879.394	1291.195	1683.894	1485.345	1422.513	1558.23
109	123437.9367	1485.973	1484.088	1926.425	3131.54	2689.203
110	123996.4794	1068.142	1326.38	1398.637	1952.814	2151.363
111	124555.0221	2500.708	1490.372	1433.823	1254.124	1580.347
112	125113.5648	438.5663	446.1062	913.5751	990.23	1216.425
113	125672.1075	860.7964	685.4955	571.7699	486.5699	633.3451

Table A.1: Real data from apparent soil resistivity measurements along the path of the 500 kV Silves-Oriximiná transmission line.

Measurement point	Distance along the power line [m]	Apparent resistivity [Ωm]				
		a = 1m	a = 2m	a = 4m	a = 8m	a = 16m
114	126230.6502	1297.478	1539.38	1382.301	2138.796	2603.752
115	126789.1929	3282.964	3355.221	3141.593	3257.203	5086.867
116	264749.2398	67.8584	146.3982	331.7522	713.7699	1794.478
117	265866.3252	56.54867	100.531	199.8053	497.6283	1176.212
118	268659.0387	70.68583	132.5752	618.2654	643.3982	2679.15
119	273685.923	211.115	379.5044	1216.425	2364.991	3367.787
120	274244.4657	60.63274	267.6637	378.2478	912.3185	2684.177
121	298261.8018	318.8717	630.2035	1226.478	2322.265	2020.672
122	299378.8872	155.5088	365.6814	554.1769	2101.097	1970.407
123	299937.4299	392.3849	753.3539	1440.106	2274.513	2050.832
124	300495.9726	237.5044	402.7522	716.2831	1198.832	1945.274
125	301054.5153	245.0442	471.2389	913.5751	1683.894	1814.584
126	302171.6007	139.4867	263.8938	480.0354	1120.92	2121.203
127	302730.1434	126.9203	352.4867	668.5309	1382.301	1729.133
128	303847.2288	414.3761	720.053	1386.071	2571.079	2407.717
129	304405.7715	218.0265	409.0354	796.7079	1759.292	2583.646
130	305522.8569	651.2522	1159.248	2135.026	4254.973	3583.929
131	307198.485	115.9248	213.6283	394.584	937.4512	1965.38
132	307757.0277	143.2566	197.292	569.2566	1369.734	2116.177
133	308315.5704	285.8849	447.3628	1022.903	2209.168	3588.955
134	308874.1131	638.3716	1243.442	2234.301	4252.46	3955.893
135	309991.1985	313.8451	567.3716	1017.876	1719.08	1955.327
136	310549.7412	188.4956	366.3097	698.6902	1223.964	1764.318
137	311108.2839	173.4159	333.6371	634.6017	1261.664	1603.469
138	311666.8266	296.5663	552.9203	933.6813	2080.991	2176.495
139	312225.3693	378.2478	708.115	1298.106	2080.991	2256.92
140	312783.912	192.8938	351.2301	694.9203	1228.991	1719.08
141	313342.4547	173.1018	311.0177	521.5044	967.6105	1603.469
142	323396.2233	351.2301	557.3185	1132.23	2199.115	4624.424
143	323954.766	334.5796	615.1238	1318.212	2646.478	3473.345
144	325071.8514	324.2124	552.292	1144.796	2035.752	5192.424
145	328423.1076	314.1593	596.2743	1186.265	2184.035	4001.132
146	329540.193	249.1283	490.7168	1063.115	2146.336	3850.336
147	330098.7357	752.0973	1352.141	2713.079	4760.141	4121.77
148	330657.2784	954.4158	1732.274	3621.628	6489.274	6444.035
149	331215.8211	240.9602	409.0354	848.23	1920.141	3493.451
150	331774.3638	162.4203	309.1327	574.2831	1073.168	1829.664

Table A.2: Average and deep layer resistivity obtained from the apparent resistivity data presented in Table A.1.

Measurement point	Distance along the power line [m]	Average of apparent resistivity [Ωm]	Deep layer soil resistivity [Ωm]
1	0	3756.21384	7441.179
2	558.5427	2812.102416	6963.94
3	1117.0854	847.9158572	4038.85
4	1675.6281	2060.884781	1206.014
5	2234.1708	961.0131927	785.6314
6	2792.7135	2000.880361	2955.416
7	3351.2562	912.8211614	250.5166
8	3909.7989	2266.219277	2136.221
9	5026.8843	1293.89635	40.0033
10	7261.0551	181.2070643	217.2759
11	8936.6832	1466.11846	1394.434
12	9495.2259	592.0017196	646.3186
13	10053.7686	1627.721986	902.924
14	10612.3113	2051.585667	2390.938
15	11170.854	1771.544097	2108.126
16	11729.3967	3203.44433	10578.14
17	12287.9394	2095.253804	3812.444
18	12846.4821	3309.542197	8945.182
19	13405.0248	2626.45314	8189.762
20	13963.5675	3565.142175	9106.031
21	14522.1102	3119.601505	10065.24
22	15080.6529	2105.369733	3681.652
23	15639.1956	2244.605119	1282.775
24	18431.9091	2734.693573	2286.546
25	19548.9945	2093.557344	1735.01
26	20666.0799	2074.959116	3571.629
27	24017.3361	7147.625942	13437
28	24575.8788	2140.55557	2093.029
29	25134.4215	2411.989176	6035.792
30	25692.9642	1836.135242	3087.858
31	26251.5069	2324.024581	5209.865
32	26810.0496	2245.170606	7832.576
33	28485.6777	3287.488216	4910.017
34	29044.2204	4763.408445	7208.678
35	29602.7631	4663.88279	9151.045
36	30719.8485	6297.636633	7541.805
37	32395.4766	5130.723458	7490.211
38	35746.7328	4278.346539	5677.011
39	36305.2755	4660.364206	6700.584
40	36863.8182	5078.196029	6188.06
41	37422.3609	5548.680945	8000.435
42	37980.9036	5349.126979	7152.205
43	38539.4463	4104.930625	5441.994
44	39097.989	3217.996187	3831.75

Table A.2: Average and deep layer resistivity obtained from the apparent resistivity data presented in Table A.1.

Measurement point	Distance along the power line [m]	Average of apparent resistivity [Ωm]	Deep layer soil resistivity [Ωm]
45	39656.5317	4299.835033	6521.033
46	40215.0744	4866.704012	7320.372
47	40773.6171	6141.436647	8965.404
48	41332.1598	11808.24148	8986.499
49	67025.124	2753.166138	7165.88
50	67583.6667	2157.520171	5931.345
51	68700.7521	2858.220996	6305.971
52	69259.2948	3193.743092	7494.429
53	70934.9229	2837.360821	5075.781
54	71493.4656	2385.976789	8989.851
55	72052.0083	2558.387393	8777.815
56	72610.551	2674.123667	5979.782
57	73169.0937	1927.304261	9245.384
58	73727.6364	4328.989013	6612.622
59	76520.3499	5478.937588	9524.091
60	77078.8926	6871.542779	13584.24
61	77637.4353	2544.187395	1619.469
62	78195.978	4386.794318	4160.195
63	79871.6061	2661.431632	6595.709
64	80430.1488	3807.107641	5792.909
65	80988.6915	1685.904282	1878.964
66	81547.2342	5095.53762	3937.832
67	82105.7769	5122.806645	10592.7
68	82664.3196	5379.914587	7979.122
69	83222.8623	5839.341097	13832.39
70	83781.405	6186.424253	11315.74
71	84339.9477	2751.281182	4870.948
72	84898.4904	1692.187467	4617.935
73	85457.0331	3158.180263	3502.28
74	86015.5758	7315.261326	6830.764
75	86574.1185	2110.396281	2781.7
76	87132.6612	3150.514777	79.41141
77	87691.2039	1344.601656	298.1177
78	88249.7466	998.3981453	471.4401
79	88808.2893	2985.643994	2629.996
80	89366.832	1937.910278	271.2149
81	89925.3747	998.3981453	471.4401
82	93276.6309	1858.943205	1682.066
83	93835.1736	1347.969443	1082.595
84	94393.7163	1354.076699	235.3324
85	94952.259	1473.281291	1403.305
86	95510.8017	1229.996356	673.0791
87	96069.3444	904.7786842	270.2601
88	96627.8871	1043.888407	405.6345

Table A.2: Average and deep layer resistivity obtained from the apparent resistivity data presented in Table A.1.

Measurement point	Distance along the power line [m]	Average of apparent resistivity [Ωm]	Deep layer soil resistivity [Ωm]
89	97186.4298	1686.281273	2058.831
90	97744.9725	2140.052916	2116.15
91	98303.5152	1752.63171	2121.316
92	99420.6006	4990.859753	5910.025
93	99979.1433	1687.663574	2126.482
94	100537.686	1364.959176	1667.436
95	101096.2287	3750.558974	295.4454
96	101654.7714	4614.119962	5059.443
97	103330.3995	3460.024485	4435.464
98	103888.9422	4002.01205	3873.717
99	105564.5703	1752.983568	1543.386
100	106123.113	3012.033373	3852.078
101	106681.6557	2209.067423	459.0045
102	107240.1984	2815.621	577.4472
103	107798.7411	1880.054708	2925.795
104	116176.8816	1572.806946	1547.282
105	116735.4243	2201.125477	2023.254
106	118969.5951	749.0185205	1160.199
107	122320.8513	1367.47245	1325.327
108	122879.394	1488.235272	1531.4
109	123437.9367	2143.445836	3220.699
110	123996.4794	1579.467123	2209.539
111	124555.0221	1651.87455	1364.502
112	125113.5648	800.980463	1450.127
113	125672.1075	647.5953432	533.7422
114	126230.6502	1792.341441	3755.242
115	126789.1929	3624.769604	3741.763
116	264749.2398	610.8512756	3472.2065
117	265866.3252	406.1450983	3404.817375
118	268659.0387	828.8149739	3337.42825
119	273685.923	1507.964474	3303.733688
120	274244.4657	860.6078915	3270.039125
121	298261.8018	1303.698119	3202.65
122	299378.8872	1029.374249	8667.175
123	299937.4299	1382.237936	2904.937
124	300495.9726	900.1291271	3394.609
125	301054.5153	1025.66717	3130.356
126	302171.6007	825.1078945	3388.0565
127	302730.1434	851.8742639	6391.23
128	303847.2288	1499.859165	3645.757
129	304405.7715	1153.341495	3459.65225
130	305522.8569	2356.885641	5316.652
131	307198.485	725.3937437	3273.5475
132	307757.0277	879.1432882	3087.44275

Table A.2: Average and deep layer resistivity obtained from the apparent resistivity data presented in Table A.1.

Measurement point	Distance along the power line [m]	Average of apparent resistivity [Ωm]	Deep layer soil resistivity [Ωm]
133	308315.5704	1510.854739	2994.390375
134	308874.1131	2464.893596	6060.43
135	309991.1985	1114.699905	2901.338
136	310549.7412	848.3556802	3716.54
137	311108.2839	801.3574541	3482.635
138	311666.8266	1208.130871	3811.548
139	312225.3693	1344.475992	3270.089
140	312783.912	837.4229377	3586.03
141	313342.4547	715.3406472	3326.086
142	323396.2233	1772.863566	3949.3095
143	323954.766	1677.547645	9601.005
144	325071.8514	1849.895418	4105.115375
145	328423.1076	1656.373311	4183.018313
146	329540.193	1559.926416	4260.92125
147	330098.7357	2739.845785	6097.223
148	330657.2784	3848.325337	4338.824188
149	331215.8211	1382.363599	4416.727125
150	331774.3638	789.7335613	4572.533